

Optimization of the Clustering and Tracking Algorithms of the Silicon Microstrip Detectors for the COMPASS Experiment

Diploma Thesis

by

Michael Leeb

November 2011

Physik Department E18
Technische Universität München

Abstract

The COMPASS experiment at CERN uses silicon microstrip detectors for beam definition and during hadron program also for the reconstruction of the primary interaction point. In the year 2009 these detectors were operated continuously at cryogenic temperatures of 200 K for the first time. The objective of this thesis is the optimization of the data reconstruction algorithms used for the silicon microstrip detectors. The clustering algorithm is extended to increase the capability of resolving several particles in close proximity with respect to each other. Furthermore improvements on the simulation of the detector response are presented. In addition, the requirements on the detector alignment in order to make full use of the detector capability are studied. Based on a precise alignment, results on the performance during cryogenic operation are given and compared to the non-cryogenic detector characteristics.

Contents

1	Introduction	1
2	COMPASS	3
2.1	Experimental Site	3
2.2	Physics Programs	4
2.2.1	Hadron Program	4
2.2.2	Muon Program	7
2.3	The COMPASS Spectrometer	7
2.3.1	Spectrometer Regions	7
2.3.2	Detector Types	8
2.3.3	Targets	12
2.4	Analysis Chain	12
2.4.1	CORAL - Event Reconstruction Software	12
2.4.2	PHAST Analysis Software	16
2.4.3	COMGEANT	16
2.4.4	ROOT	17
3	The Silicon Microstrip Detectors for COMPASS	19
3.1	Requirements on the COMPASS Silicon Microstrip Detectors	19
3.2	Basic Working Principle	20
3.2.1	Energy Loss	20
3.2.2	Semiconductor Detectors	21
3.3	Wafers and Detector Modules	23
3.3.1	Wafer Design	23
3.3.2	The Detector Module	24
3.4	Cryogenic Operation	26
3.4.1	The Silicon Stations	27
3.4.2	Cooling Circuit	29
3.5	Readout Chain	30
3.6	Data Reconstruction	32
3.6.1	Time Reconstruction	32
3.6.2	Cluster Finding	35

4	Alignment for the Primakoff Run 2009	39
4.1	The Alignment Procedure	39
4.1.1	Coordinate Systems and Formalism	39
4.1.2	The Principle	40
4.2	Requirements for the Primakoff Run	41
4.3	Troubleshooting	41
4.3.1	Silicon Detectors	42
4.3.2	The Micromegas Pitch	44
4.3.3	Run-by-Run Alignment	47
4.4	Results	47
4.5	Conclusion and Outlook	50
5	Performance of the Silicon Microstrip Detector for COMPASS	55
5.1	Signal Amplitude	55
5.2	Spatial Resolution	56
5.2.1	Method	56
5.2.2	Fitfunction for Single-strip Clusters	58
5.2.3	Results	58
5.3	Time Resolution	60
5.4	Efficiency	63
5.5	Comparison with Non-Cryogenic Results	64
5.6	Summary	67
6	Improvement of the Clustering Algorithm	69
6.1	Analysis of the Current Situation	69
6.2	Misidentified Double-strip Clusters	69
6.2.1	Approach	69
6.2.2	Performance	71
6.3	Amplitude Correlation	72
6.3.1	Technical Aspect	74
6.3.2	Performance	79
6.4	Results	80
6.5	Outlook: Particle Identification with COMPASS Silicon Detectors	82
6.6	Conclusions and Outlook	84
7	Simulation of the Detector Response	87
7.1	General Principle	87
7.2	Signal Amplitude	88
7.3	Cluster Size	88
7.4	Charge Sharing	90
7.4.1	No Intermediate Strips	90
7.4.2	Intermediate Strips	93
7.5	Conclusion and Outlook	96

8 Conclusion and Outlook	97
A Performance Plots and Histograms	99
B Plots for Alignment Studies	121
B.1 Micromegas Pitch	121
B.2 Used Productions	123
B.3 Silicon Residuals	124
Bibliography	137

List of Figures

2.1	Overview of CERN's accelerator complex. COMPASS is located in the North Area, from [20].	5
2.2	The Primakoff effect, from [61].	6
2.3	Top view of the COMPASS spectrometer in its 2009 hadron configuration, from [56].	9
3.1	Most probable energy loss in silicon scaled to the mean energy loss of a MIP, $388 \text{ eV}/\mu\text{m}$, from [27].	22
3.2	Normalized energy loss distribution for a $100 \text{ GeV}/c$ pion and a $300 \mu\text{m}$ silicon layer calculated according to [44] for $\xi=5.0 \text{ keV}$ and $\Delta_p=84 \text{ keV}$	22
3.3	Cross section through a silicon wafer of the SINTEF design, modified from [24].	24
3.4	Silicon detector module, from [24].	25
3.5	Charge collection efficiency for silicon detectors irradiated with various doses, from [15].	26
3.6	Upstream cryostat assembly, from [12].	28
3.7	Open conical cryostat with mounted detector module.	29
3.8	Simplified schematics of the cooling system of the COMPASS silicon detectors, from [3].	30
3.9	Overview of the silicon readout chain, from [12].	31
3.10	Time dependence of r_1 and r_0 obtained in the latency scan for the 2010 beam time.	34
3.11	Charge distribution for a sensor with intermediate strips (a) and without intermediate strips (b).	37
3.12	Residual distribution versus charge sharing factor η for a plane without (a) and with (b) intermediate strips. For the data shown the η -dependent position corrections were deactivated.	37
4.1	χ^2 distribution of tracks reconstructed with SI04 and SI05 only.	45
4.2	Residual versus track position measured in WRS for the four projections of MM01. The average residual as a function of the track position was fitted with a straight line.	46
4.3	Distribution of vertices along the z axis for run 81819. Fig. 4.3(a) shows the initial situation. The data shown in Fig. 4.3(b) include the alignment improvements as well as bridging over the target.	51

List of Figures

4.4	The scattering angle versus the vertex position along the z axis is shown. For the old T38 production the broad background band dominates the picture and several tracking artifacts can be seen. These vanish in the new production and a clear correlation between scattering angle and vertex resolution is present.	52
4.5	Determined shifts of all silicon U-planes for the complete Primakoff period compared to the temperature trend inside the experimental hall. The zero point for the calculation of the time values is set to the first run of the Primakoff period.	53
4.6	Vertex resolution of the Ni target along the z axis versus the scattering angle for one outgoing particle. The horizontal lines mark the acceptance region of the involved detectors between target and SM1, their ordinate is sorted according to the appearance of the detectors as in the direction of the beam. Shown are the two silicon stations inside the conical cryostat SI04 and SI05, the pixel and strip part of the first PixelGEM detector GP01P and GP01XY, as well as the three Micromegas stations MM01, MM02 and MM03.	53
5.1	Signal amplitude of clusters assigned to tracks for SI02V. The fit shown is a convolution of a Gaussian and a Landau distribution [39].	57
5.2	Residual of SI04X for single-strip clusters. Fitted with Eq. 5.2 plus a Gaussian background (yellow). The standard deviation is calculated to be $6.4 \mu\text{m}$	59
5.3	Residual distribution for SI01Y in muon beam.	60
5.4	Timing distribution of SI01X fitted with a Gaussian. The obtained σ is 1.32 ns. The time resolution stated is the RMS of the distribution shown in the histogram, with clusters outside this range being discarded. Unfolding the track time error of 0.375 ps, the intrinsic time resolution of 1.34 ns is calculated. Since the track time is dominated by the contribution of the two SciFi planes, the bias can be neglected. The right side shows the identical distribution but in logarithmic scale.	61
5.5	Two dimensional efficiency plot for a plane from the beam telescope (a) and downstream of the target (b).	65
5.6	Expected tracks in SI03X (a) and SI04U (b). The ring shaped structures are supposed to result from the beam trigger and the target discs. The low statistics in some regions is also visible in the efficiency map shown in Fig. 5.5.	66
6.1	Residual distribution for SI02V restricted to clusters of three strips. The main contribution of the double peak structure is from noise. Overlapping tracks and δ -electrons account for roughly 30%. The RMS of the shown distribution is $16 \mu\text{m}$, while the peaks at about $\pm 10 \mu\text{m}$ have a Gaussian σ of roughly $7 \mu\text{m}$	70

6.2	Residual distribution for SI05V restricted to single-strip clusters, illustrating a too strict cut on Eq. 3.16 in the Cinderella clustering, namely $Y_{\text{cutoff}}=3.5$. Clearly the sharp drops at $\pm\text{pitch}/2 \approx 27 \mu\text{m}$ can be seen, which result from actual two-strip clusters that were split into two one-strip clusters.	71
6.3	Comparison between old and new clustering as described in Section 6.2 using exactly the same data. Only clusters that showed the described structure are shown for the old clustering and the distribution for the new clustering is restricted to modified clusters. The plane presented here as an example is SI03U. The corresponding plots for the other silicon detectors together with a list of the used data are given in App. A. . . .	73
6.4	Amplitude correlation of SI02U and SI02V exemplarily. The Gaussian σ of the amplitude difference is 8 ADC channels.	73
6.5	Cluster amplitudes a_{large} of clusters composed of three or more strips on SI05V, matched with the cluster amplitudes of two single- or double-strip clusters a_{sum} on SI05U. The lines indicate the domain around the diagonal where the amplitude matching is defined successful.	76
6.6	The left side shows the difference between a_{large} and a_{sum} . The right side is the cluster amplitude distribution of a_{large} for $a_{\text{sum}} < 40$ ADC channels, i.e. the one dimensional projection of the part of Fig. 6.5 that lies below the horizontal line. The most probable value is roughly at 75 ADC channels.	76
6.7	Basic kinematics behind δ -clusters. Two new clusters are created from on the one hand the first two and on the other the last two strips. The angle with respect to the particle trajectory, under which the δ -electron is emitted, is denoted with α	79
6.8	Residual distribution of the complete mate clustering introduced in Section 6.3, separated into the different contributions for SI02U.	81
6.9	Π as defined in Eq. 6.4 over the particle momentum. The black line marks the band at $\Pi=7.5$, which corresponds to an average amplitude in the silicons of twice the most probable one. This band is supposed to stem from conversion electrons.	83
7.1	Probability for a double-strip cluster in bins of x_{dist}	89
7.2	Exemplary one-dimensional distribution of Fig. 7.3(a) for a plane without intermediate strips.	91
7.3	Charge sharing distribution versus the distance of the particle trajectory from the next strip, derived from real data (a) and obtained from simulation (b) for a plane without intermediate strips. The solid line is the function given Eq. 7.6 with the parameters presented in Eq. 7.7, while for the dashed line a was changed from 0.49 to 0.45.	92
7.4	Comparison between the simulated charge sharing and the corresponding distribution extracted from real data for a plane without intermediate strips.	93

List of Figures

7.5	Exemplary one-dimensional distribution of Fig. 7.6(a) for a detector with intermediate strips. While (a) is reasonably described by the Gaussian fit, (b) shows an asymmetry towards $\eta=0.5$	94
7.6	Charge sharing distribution versus the distance of the particle trajectory from the next strip, derived from real data (a) and obtained from simulation (b) for a plane with intermediate strips. The function is of the form given in Eq. 7.8 with the parameters presented in Eq. 7.9	95
7.7	Comparison between the simulated charge sharing and the corresponding distribution extracted from real data for a plane with intermediate strips.	96
A.1	Performance plots for SI01U.	100
A.2	Performance plots for SI01V.	101
A.3	Performance plots for SI01X.	102
A.4	Performance plots for SI01Y.	103
A.5	Performance plots for SI02U.	104
A.6	Performance plots for SI02V.	105
A.7	Performance plots for SI02Y.	107
A.8	Performance plots for SI03U.	108
A.9	Performance plots for SI03V.	109
A.10	Performance plots for SI03X.	110
A.11	Performance plots for SI03Y.	111
A.12	Performance plots for SI04U.	112
A.13	Performance plots for SI04V.	113
A.14	Performance plots for SI04X.	114
A.15	Performance plots for SI04Y.	115
A.16	Performance plots for SI05U.	116
A.17	Performance plots for SI05V.	117
A.18	Performance plots for SI05X.	118
A.19	Performance plots for SI05Y.	119
B.1	Residual versus track position measured in WRS for the four planes of MM02.	122
B.2	Residual versus track position measured in WRS for the four planes of MM03.	122
B.3	Residuals for X-like detectors placed in the beam telescope, run 81971.	125
B.4	Residuals for X-like detectors downstream of the target, run 81971.	126
B.5	Residuals for Y-like detectors placed in the beam telescope, run 81971.	127
B.6	Residuals for Y-like detectors downstream of the target, run 81971.	128
B.7	Residuals for X-like detectors placed in the beam telescope, run 82006.	129
B.8	Residuals for X-like detectors downstream of the target, run 82006.	130
B.9	Residuals for Y-like detectors placed in the beam telescope, run 82006.	131
B.10	Residuals for Y-like detectors downstream of the target, run 82006.	132
B.11	Residuals for X-like detectors placed in the beam telescope, run 82144.	133

List of Figures

B.12 Residuals for X-like detectors downstream of the target, run 82144. . . .	134
B.13 Residuals for Y-like detectors placed in the beam telescope, run 82144. .	135
B.14 Residuals for Y-like detectors downstream of the target, run 82144. . . .	136

List of Tables

4.1	Alignment summary for three runs from the Primakoff data taking period 2009. The maximal and minimal deviation for X-like and Y-like detectors is shown. The last column shows the maximal movement of planes between the considered runs. The used alignment file is based upon run 81686 which started at 05/11/09 6:35 p.m. All used start times are taken from [46].	43
4.2	Summary of the obtained slope for all MM planes.	46
5.1	Time resolution for all silicon planes. Clusters outside the range of ± 30 ns were discarded for the calculation of the RMS. Additionally the σ of a performed Gaussian fit is given. All readings are in ns.	62
5.2	Combined time resolution for all silicon sensors. Clusters outside the range of ± 30 ns were discarded.	63
5.3	Comparison of the average time resolution as obtained from a Gaussian fit in cryogenic and non-cryogenic operation. All values for non-cryogenic operation are taken from [24].	64
5.4	Comparison of the average spatial resolution and the fraction of double-strip clusters in cryogenic and non-cryogenic operation [24].	66
5.5	Performance overview of the COMPASS silicon detectors. All RMS values are given in μm . The column “Cls 3” shows the fraction of clusters that are composed of three or more strips.	67
6.1	Summary of the properties of the clustering improvement described in this section.	71
6.2	Improvement for three- and four-strip clusters due to the changed clustering algorithm described in Section 6.2. The last column gives the fraction of modified clusters with respect to the total number of clusters composed of three or four strips.	72
6.3	Naming convention of the different cluster types. The input size states the number of strips the input cluster is allowed to have in the particular category. In the last column the cluster size of possible outcomes is given.	75
6.4	Summary of the mate clustering. RMS values for the clustering described in Section 6.3 with appearance of different contributions according to Table 6.3. The RMS for the corresponding clusters as calculated with the Cinderella clustering is given for comparison. As SI02X was rendered inoperable, no amplitude matching for SI02Y could be performed.	80

List of Tables

A.1	Used runs for clustering and determination of the time resolution. Only the listed chunks were used.	99
A.2	Used runs for determination of the efficiency and the spatial resolution. In each case the complete run was used.	99
B.1	CORAL options for tracking with SI04 and SI05 only.	121
B.2	CORAL options for straight line tracking through all silicon stations. . .	124

Chapter 1

Introduction

The COMPASS experiment is a high luminosity fixed target experiment at the SPS at CERN with the aim to investigate the structure and dynamics of hadrons. The physics goals, the spectrometer components, as well as the used analysis tools are introduced in Chapter 2.

The silicon microstrip detectors play a crucial role in the COMPASS spectrometer offering a spatial resolution better than $10\ \mu\text{m}$ and a time resolution of a few ns. The detector design and the methods applied during data reconstruction are described in Chapter 3.

A precise spectrometer alignment is important for precision measurements, like the measurement of the pion polarizabilities via the Primakoff effect. In Chapter 4 studies on the 2009 spectrometer alignment exploiting the silicon detectors' high spatial resolution are presented and its impact on the data quality is evaluated.

The COMPASS silicon microstrip detectors are operated at 200 K since 2009 to increase their radiation hardness. Apart from that, a significant improvement of the detector performance is expected. In Chapter 5 the precise alignment described in Chapter 4 is used to analyze the detector performance, for the first time revealing the full capability during cryogenic operation. The results are compared to the performance during non-cryogenic operation of the detectors.

The clustering algorithm was analyzed and improvements were worked out and implemented in the reconstruction software. The amplitude correlation, which is a feature of the double-sided readout, is utilized in the reconstruction process to significantly improve the spatial resolution for specific cluster types. The developed algorithms are presented and their performance is studied in Chapter 6. In addition, the impact of the improvements on the tracking performance is evaluated.

A full simulation of the spectrometer plays an important role in all physics analysis conducted in COMPASS. Therefore the correct interactions of particles in the spectrometer have to be reproduced. The detector response of the silicon detectors to penetrating particles was analyzed on experimental data. The main features were modeled and integrated into the simulation software as presented in Chapter 7.

Chapter 2

COMPASS

The COMPASS (COmmon Muon and Proton Apparatus for Structure and Spectroscopy) experiment is a high statistics fixed target experiment located at CERN¹ operating a spectrometer with large acceptance and high angular resolution. These unique properties together with high luminosity hadron or polarised muon beams are used to investigate the structure and dynamics of hadrons. This chapter introduces the various physics questions which can be addressed with the COMPASS experiment, and in the second part presents the spectrometer layout and its different configurations. The analysis software used for physics analysis in COMPASS is addressed.

2.1 Experimental Site

CERN is an international organization currently operating the worlds largest particle accelerator LHC². Apart from acting as pre-accelerators for this accelerator the CERN accelerator complex shown in Fig. 2.1 also provides protons to several experimental areas. At the CERN site all the infrastructure needed to conduct a high-energy particle physics experiment is at hand [21]. Located in the French part of the CERN site COMPASS is provided with an high luminosity hadron or muon beam by the M2 beamline [31]. A primary beam of approximately $1.2 \cdot 10^{13}$ protons per spill cycle³ with an energy of 400 GeV is extracted from the SPS into the North Area and directed onto a Beryllium target resulting in a secondary beam primarily consisting of hadrons. The target thickness can be varied up to 500 mm to obtain various beam intensities. A sequence of bending magnets, collimators and absorbers is used to extract pions and kaons as secondary, or muons and electrons as tertiary decay products respectively. The beam mode can be switched remotely.

The *hadron beam* is available from 40 to 280 GeV/ c . The positive hadron beam mainly consists of protons whereas in the negative beam one predominantly finds pions and a small fraction of kaons and antiprotons. The intensity can be varied up to 10^8 particles per spill.

The *muon beam* originates from pions and kaons decaying into muons. For this purpose

¹European Organization for Nuclear Research

²Large Hadron Collider

³SPS accelerator cycle: Injection, acceleration and extraction. In total 45 s with roundabout 10 s of beam delivery to COMPASS.

a 600 m long decay line on the way from the primary target to the experimental hall is foreseen. Remaining hadrons are removed by hadron absorbers directly placed in the beam. A momentum range of 60 to 190 GeV/ c is available for both polarities. Because the pion decay is weak and the generated neutrino has negative helicity⁴, the muons are naturally polarized in the center of mass system. A specific polarization can be selected via the energy. The maximum flux is up to $2 \cdot 10^8$ muons per SPS cycle limited by radiation protection guidelines.

2.2 Physics Programs

2.2.1 Hadron Program

Primakoff

The electromagnetic polarizabilities of the pion and the kaon are predicted with a low uncertainty by *Chiral Perturbation Theory* (χ PT). From the experimental side these quantities can be tackled exploiting the *Primakoff Effect*. Ultra-relativistic charged pions scatter of quasi-real photons from a high Z -nuclei as shown in Fig. 2.2. This reaction takes place under very small momentum transfer making it experimentally challenging. The deviations of the measured cross section from the one of a point-like particle gives access to the electric and magnetic pion polarizability. After pilot runs in 2004 and 2009 the gathered experience is used for a high statistics measurement in 2012, which was already approved. Up to now the measurements by various experiments give no conclusive answer concerning the pion polarizabilities. COMPASS will also attempt a first measurement on kaons identified in the incoming beam by the CEDAR⁵ detectors. More details can be found in [50, 24].

Exotic Mesons

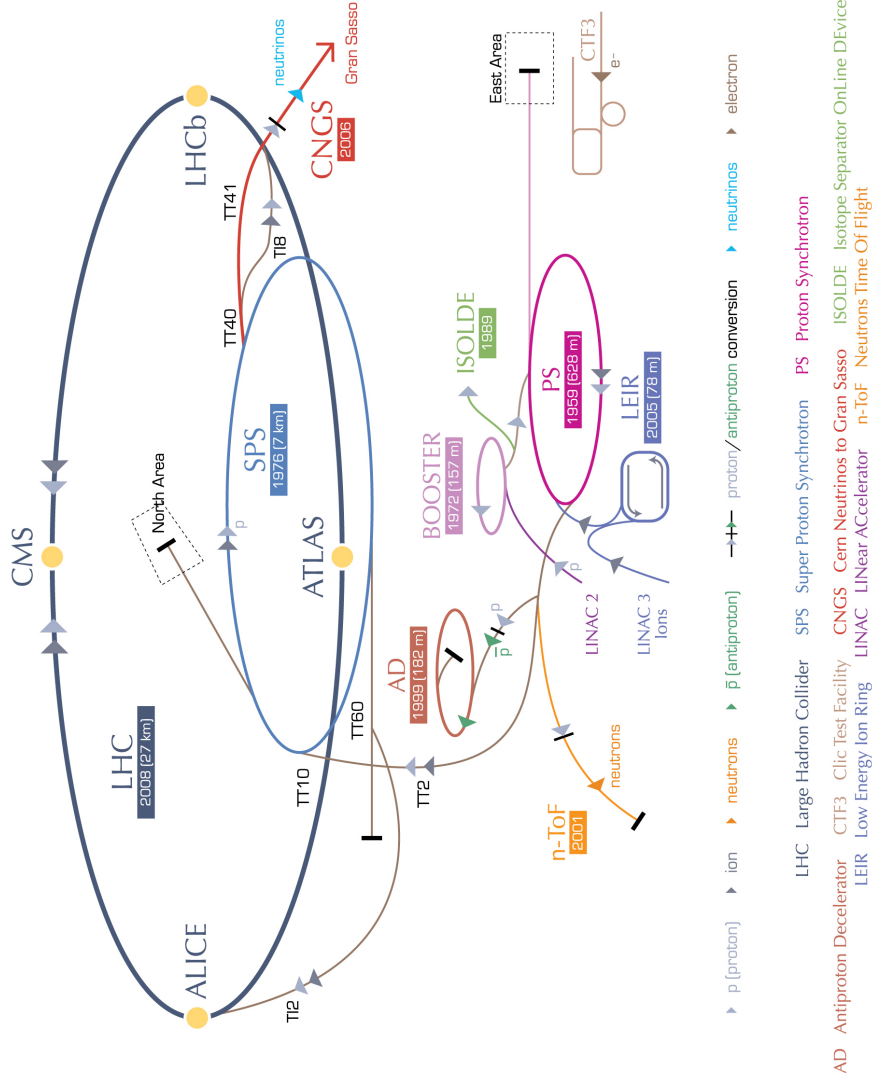
COMPASS already recorded data for investigations of the excitation spectrum of hadrons. Apart from well established hadrons, exotic configurations are searched. Exotic refers to hadrons with properties not consistent with the constituent quark model (QCM). The QCM describes hadrons as $q\bar{q}$ and baryons as qqq state. Within the underlying theory of QCD much more states are allowed, because gluons carry color charge themselves.

Pure gluonic states, so called *glueballs* can be imagined. Lattice QCD predicts the lowest lying state to show up with the quantum numbers of the vacuum $J^{PC}=0^{++}$ in a mass range of 1500 up to 1880 MeV/ c^2 [49], so glueballs should be at energies reachable with modern accelerator technology. However, mixing of glueballs with ordinary meson states makes them especially hard to detect. Gluon rich states are believed to be favored in production mechanisms like central production and identification is realized via their branching ratios.

⁴The non vanishing neutrino mass gives only a tiny correction

⁵ChErekov Differential counter with Achromatic Ring focus

CERN's accelerator complex



European Organization for Nuclear Research | Organisation européenne pour la recherche nucléaire

© CERN 2008

Figure 2.1: Overview of CERN's accelerator complex. COMPASS is located in the North Area, from [20].

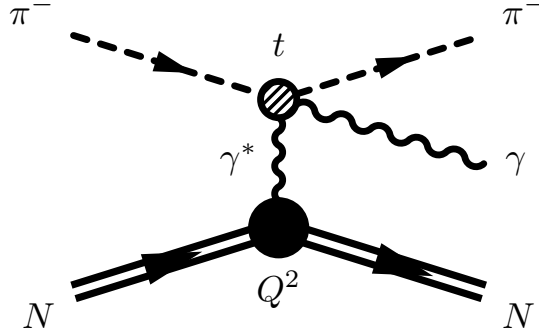


Figure 2.2: The Primakoff effect, from [61].

QCD also predicts the existence of *hybrids*, $q\bar{q}g$ states which can be viewed as a gluonic excitations of $q\bar{q}$ states. These hybrids show up in the excitation spectra of mesons, some of them with quantum numbers not accessible within the $q\bar{q}$ model. This makes things easier, because mixing with other states is only allowed for identical quantum numbers. The ground state hybrid mesons $J^{PC}=0^{-+}$, $J^{PC}=1^{-+}$, $J^{PC}=1^{--}$ and $J^{PC}=2^{-+}$ are predicted to lie slightly under $2 \text{ GeV}/c^2$ [26] and are therefore accessible at COMPASS. One spin exotic candidate, namely the $\pi_1(1600)$ with $J^{PC}=1^{-+}$, was already confirmed by COMPASS in a test run with $190 \text{ GeV}/c$ pions on a lead target [6], but attribution to a specific category is still unclear.

In all described cases COMPASS is well equipped to employ high statistics on different production mechanisms, as well as different decay channels containing both neutral and charged particles, to add further experimental observations. The experimental technique used to disentangle different contributions is *Partial Wave Analysis* (PWA). Intermediate states are expanded in a complete set of Eigenstates and the total angular distribution is then described by a set of complex parameters. These decay amplitudes are fitted to the experimental data inside mass bins. This technique requires high statistics as well as the reconstruction of all final state particles, charged and neutral. The analysis is challenging, since the math sometimes introduces ambiguities and interpretation of the results needs not to be conclusive.

Drell-Yan

During the *Drell-Yan* process a quark and a anti-quark coming from two different hadrons annihilate and produce either a virtual photon or a Z-boson which then decays into two leptons. Muons are especially interesting as a final state, because hadronic background can be strongly suppressed by a hadron absorber. Using this process one can study Parton Distribution Functions (PDF) without requirement of the fragmentation functions. After promising results in several test-runs as in 2009, a full run of Drell-Yan data taking for 2014 is approved.

2.2.2 Muon Program

Gluon Polarisation

The EMC (European Muon Collaboration), the predecessor of COMPASS, measured that the spin of the quarks is not sufficient to explain the total spin of the nucleons. This spin crisis led to the idea that the total spin of the nucleon consists of the following contributions:

$$\frac{1}{2} = \frac{1}{2}\Delta\Sigma + \Delta G + L_z^q + L_z^g \quad (2.1)$$

with in order of appearance the quark spin contribution $\Delta\Sigma$, the gluonic spin contributions ΔG and the angular momenta of quarks L_z^q and gluons L_z^g respectively. Since nucleons are the lightest baryons no orbital excitation is expected, which leaves the gluons to contribute for the missing 75% of the nucleon's spin. Gluons carry only color charge and are thus not directly accessible via photons. Therefore *photon gluon fusion*, a second order process, where the gluon interacts with the photon via a virtual quark anti-quark line, is used. The *open charm* channel, where a $c\bar{c}$ pair is produced fragmenting into a D-meson which is then reconstructed via the invariant mass, is very promising. This channel offers very low background, but suffers from limited statistics. The gluon polarization is then accessed via the cross section asymmetry for different target polarizations [37].

Generalized Parton Distribution Functions (GPDs)

A parton distribution function is the probability density function for finding a parton with a certain longitudinal momentum fraction. The GPDs generalize this concept in a way, that the parton distribution function now also depends on the partons spin projection and its transverse momentum. This way a more detailed picture of the structure of nucleons can be obtained. Experimentally this quantities can be measured in exclusive⁶ processes such as DVCS⁷ and DVMP⁸.

2.3 The COMPASS Spectrometer

2.3.1 Spectrometer Regions

The top view of the COMPASS spectrometer is shown in Fig. 2.3. The spectrometer extends over a length of more than 50m and consists of three main regions: The first part is the beam telescope upstream of the target, the second and third part are located downstream of the target referred to as *Large Angle Spectrometer* (LAS) and *Small Angle Spectrometer* (SAS) respectively. The need for a large acceptance coverage

⁶i.e. all outgoing particles need to be reconstructed.

⁷Deeply Virtual Compton Scattering

⁸Deeply Virtual Meson Production

and the requirement to access a large range of momentum transfer favors the use of a two stage spectrometer. Each stage is grouped around a dipole magnet. All quoted detector performances in this section are taken from [2].

Upstream of the target the spectrometer begins with the final part of the beam line, the Beam Momentum Station (BMS) which is used for momentum measurement of the incoming beam particles on an event by event basis. It consists of a bending magnet, scintillator hodoscopes and scintillating fibre detectors (SciFi) for tracking. The material budget makes this only viable for muon beams. In the hadron configuration of the spectrometer, two CEDARs provide separation of the different particle species. Veto detectors separate the halo from the beam and three silicon stations combined with two scintillating fibres form a fast and high resolution beam telescope.

The LAS, which is the closer one to the target covers a momentum range of about 1-20 GeV/ c . The dipole magnet in the LAS is called SM1⁹ with a field integral of 1.0 Tm and is sandwiched by several tracking detectors. The RICH¹⁰ performs reliable PID¹¹ in a momentum range of one to a few ten GeV/ c . This stage is completed by ECAL1¹² and HCAL1¹³, which have holes matching the acceptance region of the SAS, and a muon filter.

The magnet in the SAS is SM2 with a field integral of 4.4 Tm directly behind the LAS. With the SAS scattering angles up to 30 mrad are covered, a region intentionally left out in the LAS. The basic structure is similar to the LAS, except since there is no RICH in the SAS, the tracking detectors are immediately followed by the second electromagnetic calorimeter (ECAL2). The spectrometer is completed by a beam dump, absorbing remainders of the beam.

2.3.2 Detector Types

The Tracking Detectors

COMPASS operates a large variety of different detector technologies, each carefully chosen to fulfil the demanding requirements in the various spectrometer regions and to cover the overall spectrometer acceptance. Namely the rate capability, time and spatial resolution and the costs per active area have to be tailored according to the needs. Based on these criteria the tracking detectors can be arranged in three categories.

The *Very Small Area Trackers* (VSAT) cover the radial distance of 2.5-3 cm around the beam. In this region the detectors need to stand highest particle rates up to $2 \cdot 10^7$ muons per SPS cycle therefore requiring excellent time or spatial resolution. In this region, SciFis provide a time resolution down to 400 ps. They can be found on different positions along the beam throughout the spectrometer, but are always placed close to the beam. The varying level of beam widening at the given position leads to active areas

⁹Spectrometer Magnet 1

¹⁰Ring Imaging Cherenkov Detector

¹¹Particle IDentification

¹²Electromagnetic CALorimeter 1

¹³Hadronic CALorimeter 1

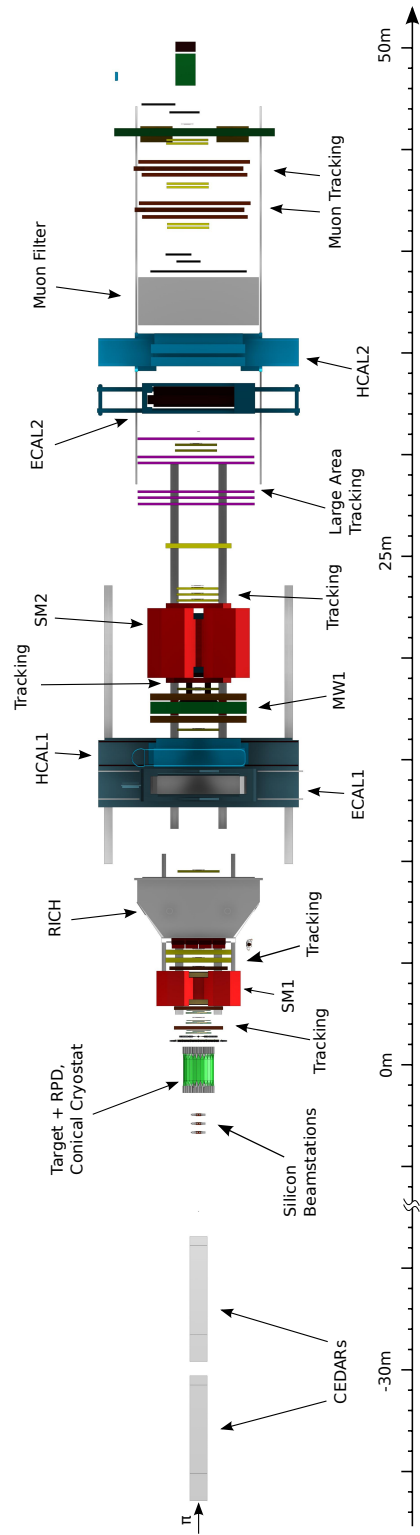


Figure 2.3: Top view of the COMPASS spectrometer in its 2009 hadron configuration, from [56].

between $5.3 \times 5.3 \text{ cm}^2$ and $12 \times 12 \text{ cm}^2$. Silicon microstrip detectors, which are the central part of this work (see Chapter 3), offer excellent spatial resolution better than $10 \mu\text{m}$ and time resolution better than 3 ns (see Chapter 5). The double-sided design is optimized for a minimal material budget to minimise multiple scattering and secondary interactions downstream of the target. The amplitudes recorded on both sides are correlated due to their common active volume, a fact that can be utilized to refine the reconstruction algorithms as will be shown in Chapter 6. The radiation damage is minimized by a radiation hard wafer design as well as operating the detectors at cryogenic temperatures. Since 2008 five micropattern PixelGEM detectors with a novel readout are used in COMPASS. The central part of $32 \times 32 \text{ mm}^2$ is read out via 1024 pixels. This reduces the occupancy in comparison to a standard strip readout and therefore allows the application of the detector centered in the beam. This pixel part is surrounded by a standard orthogonal strip readout with 2×256 strips per projection. The spatial resolution is around $135 \mu\text{m}$ and the time resolution better than 10 ns [3]. Among the *Small Area Trackers* (SAT) are micropattern gas detectors with COMPASS being the first particle physics experiment employing these kind of detectors in a large scale. They cover the intermediate region of 2.5 to 20 cm radius around the beam combining the capability of standing high rates together with good spatial resolution better than $150 \mu\text{m}$ while covering a fairly large area. The acceptance overlap is sufficient to make a relative alignment between the VSAT and the SAT possible. One type of this detector category are the *Micromegas*¹⁴ (MM) detectors. Twelve detector planes grouped in three stations are placed between the target and SM1. This leaves 4 separate planes per station. Each plane has a separate active volume with two planes being mounted on one common frame in way, that two orthogonal coordinates are measured. The second frame of a station is rotated with respect to the first one by 45° , so one MM station measures 4 different coordinates (X, Y, U, V). This is done to reduce ambiguities during the tracking. Each detector plane covers an active area of $40 \times 40 \text{ cm}^2$ with a dead zone of 5 cm diameter centered around the beam. The readout is realized with 1024 strips which have a strip pitch of $360 \mu\text{m}$ for the central 512 strips and of $420 \mu\text{m}$ for the outer two sets of 256 strips each. Special about the Micromega detectors is a metallic micromesh that separates the gas volume into two domains: Inside a rather wide¹⁵ conversion gap the primary ionization takes place. The amplification gap on the contrary is only $100 \mu\text{m}$ thick which results in a high electric field producing a large number of charge carriers in an avalanche. The spatial resolution is around $100 \mu\text{m}$ and the time resolution is better than 15 ns. The other detector type used as SAT are the *GEM*¹⁶ detectors. An active area of $31 \times 31 \text{ cm}^2$ is covered by two sets of 768 readout strips with a pitch of $400 \mu\text{m}$. The holding structure is made from a light-weight honeycomb structure. In the center a hole of 5 cm diameter is left out for the beam to pass through. The amplification stage of this central region can be deactivated during

¹⁴Micromesh Gaseous Structure

¹⁵3-5 mm

¹⁶Gas Electron Multiplier

high intensity beams. The average spatial resolution of all GEM planes is $70\ \mu\text{m}$. An analogue readout mode similar to the one presented in Section 3.6.1 yields an average time resolution of 12 ns.

The large angle acceptance is covered by the *Large Area Trackers*. Three identical *Drift Chambers* (DC) are located¹⁷ around SM1 fully covering the magnets acceptance with a central hole of 30 cm diameter. Several *Straw tube chambers* (Straws) are used downstream of SM1 and in addition 11 *Multiwire proportional chambers* (MWPCs) complete the LAS. The detector resolutions are between 0.2 and 1.6 mm.

Several different targets are available for physics with hadron beam, see Section 2.3.3. Each one of this targets is surrounded by the RPD¹⁸, which is a cylindrical TOF¹⁹ detector especially built for hadron physics surrounding the target. It consists of two layers of scintillator slabs mounted inside a barrel shaped holding structure. The RPD ensures the exclusivity of the measured scattering process by detecting the recoil proton. For the 2009 hadron run a conical shaped cryostat was built fitting nicely into the RPD and housing two silicon stations, see Chapter 3.4.1. The silicon detectors secure precise vertex definition. A detailed review of the requirements and the performance of the vertex detectors is given in Chapter 4.

Particle Identification

Muon Identification can be performed utilizing the muons superb penetration power. Tracking detectors are combined with a massive hadron absorber to reconstruct track segments up- and downstream of the absorber. Segments which can be matched to form a track belong to muons, since no other particles are able to penetrate the absorber. The first muon identification stage is placed in front of SM2, consisting of two stations of *Mini Drift Tubes* (MDTs) around a 60 cm thick iron absorber. In the second stage a 2.4 m thick concrete block is surrounded by *Muon Wall 2* (MW2) and three MWPC stations.

The *RICH* is a useful detector for hadron identification between 5 and 50 GeV/c [3]. The gas vessel has a volume of approximately $80\ \text{m}^3$ at a length of 3 m and is filled with C_4F_{10} at atmospheric pressure. Charged particles crossing the radiator gas cause emission of Cherenkov photons which are reflected by mirrors and then detected. For the peripheral regions²⁰ the photons are converted to electrons via CsI photo cathodes. These electrons are then detected by large scale MWPCs. In the central region a good resolution of the Cherenkov angle is crucial as it determines the mass separation capabilities. Therefore MAPMTs²¹ with a sub-ns time resolution are applied. During Primakoff measurement the RICH is filled with Nitrogen.

¹⁷one upstream, two downstream

¹⁸Recoil Proton Detector

¹⁹Time Of Flight

²⁰About 75% of the surface

²¹Multi-Anode PhotoMultiplier Tubes

2.3.3 Targets

For Hadron Beam

Several different targets together with the flexibility in the choice of beam particles makes COMPASS well equipped to address a large number of physics questions. For hadron beams a 40 cm long *liquid hydrogen target* is available where one basically scatters on protons. In addition several *nuclear targets* have been used. The thickness of the targets depends on the desired radiation length and has to be carefully chosen in consideration of interaction rate as well as multiple scattering of final states. For the Primakoff measurement in 2009 two targets made from Ni and W were used. While the Ni target was used for the primary reactions, the W target served as a feasibility study for a π^0 lifetime measurement. The targets are of disc shape with a diameter of about 30 mm attached to an extreme light weighted target holder which could be inserted in the RPD.

For Muon Beam

For physics using the polarized muon beam also a *polarized target* is required to measure spin-dependent effects. The target material is either deuterated Lithium (${}^6\text{LiD}$) or protons in the form of NH_3 , where in both cases the technique of Dynamic Nucleon Polarization (DNP) [4] is used. The nucleons cannot be polarized directly at affordable costs, so a combination of two separate microwave systems has to be used. The microwaves are polarizing paramagnetic centers, i.e. impurities with an odd number of valence electrons and then transferring the polarization to the nucleons. To build up and sustain the polarization for reasonable times the three target cells with a combined length of 1.20 m are surrounded by a superconductive solenoid creating a highly homogeneous magnetic field of up to 2.5 T. Using a Helium dilution refrigerator the target material is cooled down to 90 mK to counter thermal relaxation. This way relaxation times larger than 1000 h are reached during normal operation while the average polarization is above 50 % and above 85 % for ${}^6\text{LiD}$ and NH_3 respectively.

2.4 Analysis Chain

2.4.1 CORAL - Event Reconstruction Software

CORAL²² is the C++ *reconstruction* software used for COMPASS data. It is a collective software project constantly under construction and review. CORAL is working either on simulated data from the Monte Carlo simulation (see Section 2.4.3) or on raw data recorded in the experiment. The raw data has an event structure, where each event contains the recorded detector information identified by a data header. The purpose of CORAL is to process the raw data into a format that is suitable for physics

²²COMPASS Reconstruction and AnaLysis software

data analysis, i.e. particle trajectories, interaction points and preliminary particle identification. This is also done on an event by event basis, meaning that the different steps of the reconstruction process described below are repeated independently for each recorded event.

Decoding / Digitization

During the *decoding* phase the digitized detector information is extracted from the electronics data format and abstracted into logical units, so called digits. Now the information like time or signal amplitudes of a single electronics channel can be accessed via the object corresponding to the respective detector plane. In case of Monte Carlo data, the digitization is simulated. For each detector the impact point and the energy loss of simulated particle trajectories crossing this detector during one event are supplied. Based on this information for each detector plane a detector response is simulated. After this step simulated and real data should be treated equally in CORAL. The digitization step of the silicon detectors for Monte Carlo generated data was revised during the course of this thesis. The results are presented in Chapter 7.

Clustering

The different digits recorded in a detector plane during one event are combined into *clusters*. This means to connect adjacent digits, that are supposed to result from the same particle trajectory, into one common object. For this reason calibration data like pedestals²³ or timing parameters are loaded from a MySQL²⁴ database that contains all calibration files used in COMPASS. Clusters are a data structure which in CORAL are foreseen to hold the one or two-dimensional position information (including the error) on the detector plane and therefore within COMPASS reference system. This conversion is done using the alignment file, a list of all detectors in use with the three-dimensional coordinates as well as the detectors orientation. Furthermore the clusters contain additional information like signal amplitudes and time values together with the associated uncertainty. In general this information is not saved in the final output. One objective of this thesis is the optimization of the clustering algorithm of the COMPASS silicon detectors as presented in Chapter 6.

Tracking

As already mentioned the objective is to reconstruct complete particle trajectories. For this purpose the clusters are combined to form *tracks* which can be viewed as trajectory *candidates*. This process called tracking is done with the TraFDic²⁵ package. This

²³The average amplitude without a signal present.

²⁴A relational database management system under the free software license GNU

²⁵Track Finding with Dictionary

section is a summary of the different steps executed during the tracking and entirely based on [9].

The first step is the *Pattern Recognition* where all clusters belonging to a track have to be identified among all clusters created from the recorded hits during one event. For this purpose the spectrometer is divided into various zones, where within the zones an approximation of the tracks as straight lines is valid up to the desired value of precision. The spectrometer magnets SM1 and SM2 define borders of zones as well as the target where intentionally the scattering process should occur. In addition the hadron absorbers used in the muon identification stages define zone borders because of there large material budget:

- 1st zone : Target – SM1
- 2nd zone : SM1 – SM2
- 3rd zone : SM2 – MW2
- 4th zone : MW2 – End of spectrometer
- 5th zone : Upstream of the target

The exact borders of the zones in terms of a coordinate along the beam direction can be easily accessed and changed via an options file. The pattern recognition first takes place in different projections of the spectrometer, meaning all detectors in one zone measuring approximately under the same angle. Inside this group of detectors, and therefore a subset of a clusters, the so-called *pivot planes* algorithm is used. Two detector planes act as pivot elements and connecting two clusters with a straight line one can extrapolate where other detectors should have clusters, if indeed the two clusters chosen at the beginning stem from a real particle trajectory. The interval around the extrapolated impact point in which clusters are accepted is usually called *route width*. In most cases a route width of $\pm 2\sigma$ is used, with σ being the spatial resolution of the detector in question. It shall be stressed, that here not the clusters position uncertainty assigned during the clustering (see Section 2.4.1) but instead the detectors spatial resolution is used. It is usually taken to be $\text{pitch}/\sqrt{12}$, although some detectors actually do much better in terms of spatial resolution or offer clusters with different precision. This procedure is repeated successively with all combinations of clusters in the pivot planes. This way a list of one-dimensional *projection track* candidates is formed and subsequently cleaned by cutting on a minimum number of found clusters as well as a maximum value of χ^2 , which is defined as the sum of the squared deviations of a theoretical distribution from the measuring points normalized to the measurement uncertainties. Also different track candidates are only allowed to match up to a specified number of clusters. If this parameter is exceeded, the candidate with the better quality in terms of used clusters and χ^2 is kept, while the other one is rejected. The left over projection track segments are combined in a similar way to obtain *space track* segments.

The main difference is, that combining two projection segments now yields a route in three-dimensional space. This allows to assign cluster coordinates perpendicular to the measured axis. This way an additional consistency check can be performed, rejecting segments where the clusters are reconstructed outside the detectors active area. The cleaning phase is largely similar.

As a prerequisite to the next step, a quick straight line fit for the obtained space track segments candidates is performed. This is realized using a *dictionary* as a look-up table. For all accessible (and reasonable) track parametrizations the crossing point for all detector planes crossed by the track is stored, allowing for a very fast χ^2 -fit. During the *bridging*, track segments from adjacent zones are combined. Again, all possible combinations are fitted, and when the fit process converged, i.e. was successful, the track candidate is rated according to a quality function. The obtained list is again cleaned by dropping combinations where up- or downstream segments are shared with combinations of a better quality.

The *track fitting* is the final stage of the track reconstruction algorithm. A full *Kalman fit* is applied, where the clusters are added successively to the fit, yielding the option of dropping a cluster, without the need of redoing the fit. Another advantage over an conventional χ^2 fit is computational speed. Without going into mathematical details, a Kalman fit is done using $n \times n$ matrices, where n is the dimension of a state vector, i.e. the parametrization of a track candidate. Usually n is 5 in COMPASS. A χ^2 fit in contrast has to deal with square matrices of the size of number of measurements. For COMPASS this number can be up to 200. In the end the fit yields the optimum track parametrization as well as the corresponding error matrix.

To obtain the track parameter between the first and last point, the *smoothing* procedure is applied. This is for example needed for the RICH reconstruction or to analyze detector performances. Smoothing is yielding the mathematically best approximation of the track parameters on the detector plane without usage of the information provided by the plane under consideration. This makes it an extremely useful tool to extract *unbiased* residuals and detector efficiencies. Most of the terms needed for the smoothing are already evaluated once during the fitting step and than stored for future access which makes the process considerably faster.

Vertex Identification and Reconstruction

The interaction point, often referred to as *vertex*, needs to be identified the process often sloppily called “vertexing”. A two phase algorithm is applied. Among the reconstructed tracks a subset is chosen using basic cuts on geometrical properties as well as the time and momentum. As starting hypothesis this tracks are supposed to originate from one interaction point therefore performing a global fit. From this tracks an initial position of the interaction point can be calculated by averaging the z coordinate²⁶ of points of closest approach with the incoming beam track. Now an *inverse Kalman filter* is

²⁶along beam axis

applied, refitting the vertex position and updating the track parameters. Tracks fitting poorly are discarded sequentially with an update after each dismissal. This procedure is repeated until all tracks fulfill the beforehand defined quality criteria. Naturally it is not possible to drop the incoming beam track.

Data Output

The reconstructed information, i.e. tracks, interaction points, particle identification all with the calculated error matrices are stored in *Data Summary Trees (DST)*, which is basically a ROOT (Section 2.4.4) tree allowing for efficient data compression and fast access. As mentioned above, clusters as well as the detector raw information are not stored in the usually used mini DSTs. This can be done specifying separate options resulting in MegaDST (clusters saved) or GigaDST (raw digits saved) as data output.

2.4.2 PHAST Analysis Software

The PHysics [33] Analysis Software Tools (PHAST) is a C++ program capable of handling the mDST data format produced by CORAL. The main concept of PHAST is to provide all information needed for physics analysis at COMPASS in convenient data structures. The main structure is an event, providing easy access to all the tracks and vertices reconstructed with CORAL. In addition general information concerning the spectrometer setup, detectors as well as magnetic- and material maps are available. The individual physics analysis is realized via specific functions that can be easily embedded in the program. During execution this function is called for each event in the mDST. As output either mDST can be used, which is especially useful for basic physics cuts, or using any one of the data types realized in the ROOT framework is also feasible.

During the course of this work a new aspect became available: The Kalman filter used in CORAL was ported to the PHAST framework. This allows an easy refit of tracks on the PHAST level with the potential to add or remove detector planes from the fit, recalculate cluster positions, or change the detector alignment. Especially for the results presented in Chapter 5 this feature was extensively used. The only prerequisite is the usage of MegaDSTs, since the information stored in the clusters is needed for the fit.

2.4.3 COMGEANT

COMGEANT [23] is based on the GEANT²⁷ version 3.21 [22] and used to simulate the COMPASS spectrometer. The detector response is then simulated in CORAL. A variety of different generators can be linked to COMGEANT to simulate different interaction types. It tracks particles through the spectrometer simulating decays and secondary interactions. For each active detector volume, the position and the energy loss are saved. The geometry described is also used within CORAL to account for

²⁷GEometry ANd Tracking

the material budget of the various detectors. Based on these information, tracks are properly propagated through the spectrometer taking into account material effects. This can be done using material maps or the more modern option ROOT geometry which was shown to yield better results.

2.4.4 ROOT

ROOT [18] is an object-oriented C++ framework for data analysis tailored to the needs of high energy physics experiments. It is developed at CERN since 1995 superseding the Fortran-based PAW, and practically the standard framework in the data analysis of all high energy physics experiments. ROOT provides a large number of useful tools for data analysis, like mathematical libraries, fitting algorithms and data structures for handling large amount of data collected in modern physics experiments.

Chapter 3

The Silicon Microstrip Detectors for COMPASS

The COMPASS silicon microstrip detectors are used for beam definition and, during hadron beam, for vertex detection. Since the year 2009 the silicon detectors are equipped with a liquid nitrogen cooling which allows stable operation at cryogenic temperatures of 200 K. The multi-sample readout permits pulse shape analysis improving time resolution considerably. This is used in the cluster finding algorithm, that combines the detector raw information into the clusters used for track reconstruction in CORAL.

3.1 Requirements on the COMPASS Silicon Microstrip Detectors

The COMPASS silicon detectors are used in the beam telescope for beam definition and during the hadron program also for vertex reconstruction. Especially for the latter case, an excellent spatial resolution is needed to obtain the desired angular resolution of up to $50 \mu\text{rad}$. The wafer's active area is exposed to the beam ($2 \cdot 10^8$ particles per spill¹) making a radiation hard design inevitable. In addition, a time resolution in the order of a few nanoseconds is needed. For precision measurements a low material budget is required to reduce multiple scattering, thus a wafer design with double-sided readout was chosen. Furthermore the muon beam of size $8 \times 8 \text{ mm}^2$ [2] has to be covered by the active area. For the vertex detectors downstream of the target, the region of smallest scattering angles has to be covered, where the other COMPASS detectors, located further downstream, have inactive zones.

¹For muon run

3.2 Basic Working Principle

3.2.1 Energy Loss

Bethe-Formula

In principle, two effects occur when a particle passes through matter. The particle loses part or all of its energy and it is deflected from its original trajectory. Since the material budget of the COMPASS silicon detectors was carefully minimized, the latter effect plays only a minor role for the presented analysis and will therefore not be discussed in this work.

For the most common heavy charged particles in the COMPASS environment, i.e. pions, protons and muons, inelastic collisions with the atom's electron shell strongly dominate the energy loss. The number of collisions as well as the transferred energy per collision are of a statistical nature. Usually the energy loss per collision is small compared to the incident particle's total energy, but the large number of collisions in dense media can easily accumulate to a substantial energy loss. Collisions with the electron shell can either be *soft*, when an electron is excited into a higher energy state, or *hard*, if the electron is completely removed from the shell and the atom is ionized. During a fraction of these hard collisions, enough energy is transferred so that secondary ionization from the emitted electron is possible. These electrons are generally referred to as δ -electrons.

The average energy loss per unit path, usually written as dE/dx , can be calculated using the *Bethe-Formula* [10]:

$$-\frac{1}{\rho} \frac{dE}{dx} = 2\pi N_a r_e^2 m_e c^2 \frac{Z}{A} \frac{z^2}{\beta^2} \left[\ln \left(\frac{2m_e \gamma^2 v^2 W_{max}}{I^2} \right) - 2\beta^2 - \delta - 2\frac{C}{Z} \right]. \quad (3.1)$$

Within this formula, N_a is the Avogadro number, m_e and r_e the electron's mass and classical radius, Z , A and I the atomic number, weight and mean excitation potential of the absorbing material, z the charge of the incident particle in units of the elementary charge, W_{max} the maximum energy transfer in a single collision and ρ the density of the absorbing material. In addition, two corrections to the classical Bethe Formula were added: the *density effect correction* δ and the *shell correction* C . These corrections play an important role at high and low energies of the incident particle respectively. For ultra-relativistic particles, the longitudinal electric field contracts, increasing its transverse component. This leads to an effective polarization of the medium resulting in a lower contribution from far-off atoms. Therefore, the strength of the effect increases with the density of the medium. The shell correction on the other hand, is important for lower energies, where the assumption that the atomic electron's velocity is small compared to that of the incident particle is no longer valid.

Fig. 3.1 shows the energy loss as a function of $\beta\gamma$ for different absorber thicknesses calculated according to the Bethe Formula. Particles with $\beta\gamma \approx 3$ are called *Minimum Ionizing Particles (MIPs)*, as the function shows a minimum at this point. Slower

particles experience a rapid increase in the mean energy loss, leading to the *Bragg Peak* in the deposited Energy at the end of the trajectory. The average energy loss for particles faster than $\beta\gamma \approx 3$ is only increasing slowly (*relativistic rise*).

Energy Loss Distribution

Due to the statistical nature of the number of collisions as well as the energy transferred in one collision, the energy loss after a given absorber thickness will be distributed around the mean energy loss given by the Bethe Formula. For thick absorbers with a sufficiently large number of collisions, the distribution approaches a Gaussian, but the tail towards high energies resulting from large energy transfers in single collisions does not vanish. For thin absorbers the situation is significantly more complex. This stems from the fact that large energy transfers can occur in single collisions, which becomes more important at smaller absorber thickness. These sporadic collisions with high energy transfer add a long tail towards higher energy losses to the energy loss distribution giving it the asymmetric skewed shape depicted in Fig. 3.2 known as *Landau* distribution. The mean energy loss is no longer at the peak of the curve but shifted towards higher energies. The probability function $f(\Delta; \Delta_p, \xi)$ for an energy loss Δ is characterized by the *Most Probable Energy Loss* Δ_p and the Landau width $w = 4\xi$ of the distribution [53].

3.2.2 Semiconductor Detectors

Since the 1960's, semiconductors are widely used in high-energy physics for charged particle spectroscopy as well as for position sensing [45]. Where high spatial resolution in the order of a few μm is not an issue, they are competing with gas-filled proportional counters and gaseous micro-pattern detectors. The semiconductor detectors are sometimes preferred because the higher medium density allows compact sizes which in turn offers a quick charge collection and therefore fast response times down to a few ns. Further advantages are the higher spatial resolution in the order of a few μm and in some applications an order of magnitude lower bias voltages.

Among the position sensitive semiconductor detectors, silicon is by far the most commonly used material. All semiconductor detectors use a semiconductor *junction* which forms at the contact surface of n-type and p-type semiconductor material. The doping leads to the formation of volume free of charge carriers, the *depletion zone*. By applying a bias voltage, the thickness of the depletion zone can be increased to macroscopic dimensions. Particles traversing through the detector deposit energy, leading to electron-hole pair creation. On average 3.6 eV are needed at room temperature to create one electron-hole pair in silicon. Due to the electric field, the charge carriers are swept to the surface of the depletion zone and can there be detected.

To obtain high spatial resolution, microstrip detectors can be used [42]. Here the surface of the sensor is segmented to extract the position information. Generally, high resistive n-type silicon is used as a base material, on which p^+ implants form narrow

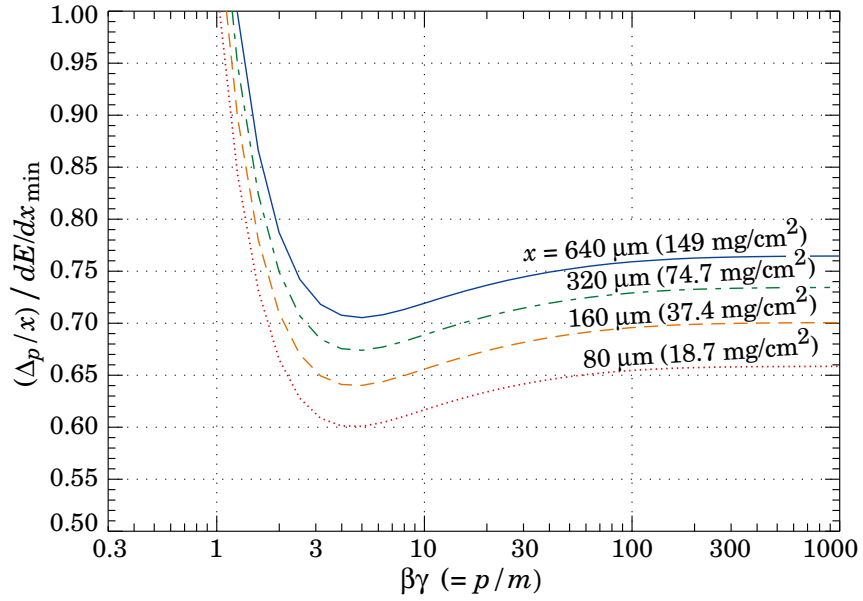


Figure 3.1: Most probable energy loss in silicon scaled to the mean energy loss of a MIP, $388 \text{ eV}/\mu\text{m}$, from [27].

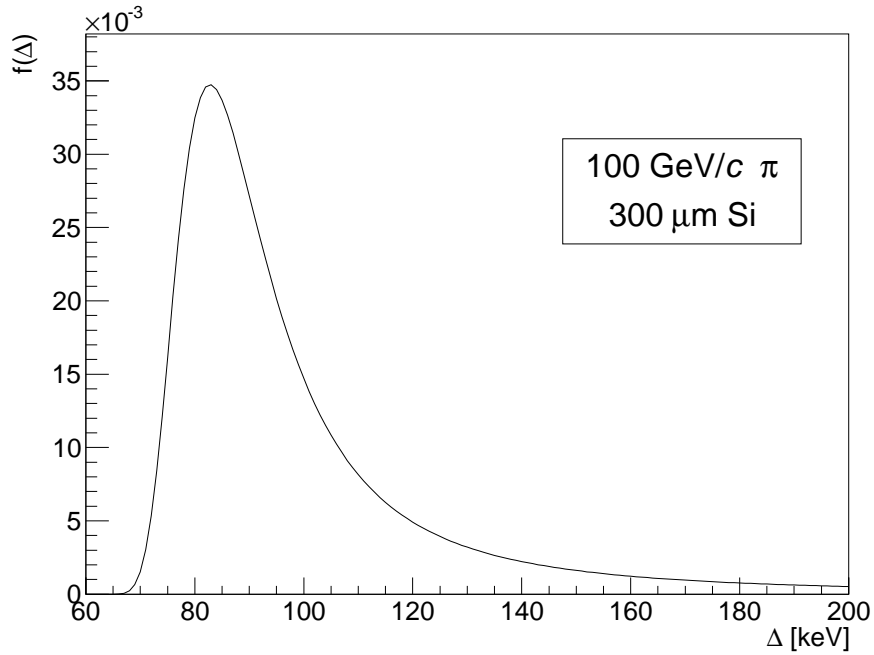


Figure 3.2: Normalized energy loss distribution for a $100 \text{ GeV}/c$ pion and a $300 \mu\text{m}$ silicon layer calculated according to [44] for $\xi=5.0 \text{ keV}$ and $\Delta_p=84 \text{ keV}$.

parallel strips, combined with an n^+ electrode on the other side. Charge carriers created inside the depletion zone will follow the field lines to the corresponding segment or strip. Therefore, only strips which were sufficiently close to the passing particle's trajectory will show a signal significantly above noise level. For the case when one strip collects all generated charge carriers, the resolution can be calculated to be $\frac{\text{pitch}}{\sqrt{12}}$ with typical pitches being around $60 \mu\text{m}$. However, the possibility of improving the spatial resolution by lowering the pitch is limited. For one thing, the number of channels increases which is a mere technical problem. On the other hand, the noise characteristics worsens because of a lower signal-to-noise ratio as the charge is divided among more strips. For this reason, intermediate strips which are not read out are implemented. These strips couple capacitively to the neighboring strips, enhancing the charge sharing and therefore the spatial resolution. If two or more strips show a clear signal, the position information can be refined as shown in Section 3.6.2.

3.3 Wafers and Detector Modules

Depending on the setup, up to ten silicon microstrip detectors are in use in the COMPASS spectrometer. During the rest of this chapter the design of the COMPASS silicon detectors is described together with the employed readout chain. In addition, the infrastructure for cryogenic operation and the various modifications to the detectors are presented. The last section covers the data reconstruction, namely the precise extraction of the signal time and the cluster finding algorithm.

3.3.1 Wafer Design

While the original wafer design was done for the HERA-B [25] experiment by the Semiconductor Laboratory (HLL)² of the Max-Planck-Institutes in Munich [5], a second version was also produced by the Norwegian company SINTEF [58] in Oslo. Both versions differ slightly in the technologies which were applied, a difference that will be discussed later on. The wafers are optimized for high fluences and a double-sided design was chosen as it reduces the material budget by a factor of two compared to a single-sided design. In addition, the signals read out on the two sides of the sensor are correlated due to the common active volume. This correlation can be exploited to significantly improve the data reconstruction as will be shown in Chapter 6.

The active area has a size of $70 \text{ mm} \times 50 \text{ mm}$ with 1280 strips on the long and 1024 strips on the short side at a thickness of $280 \mu\text{m}$. The strips on the two sides are perpendicular to each other in order to obtain a two-dimensional spatial information with one sensor. One side measures only one coordinate, called *projection*. Furthermore the strips are tilted by 2.5° with respect to the sensor edge, optimized for the HERA-B vertex detector. This way four different projections are obtained from two detector modules when mounted back to back. A cross section through a silicon sensor of the

²HallLeiter Labor

HLL design is depicted in Fig. 3.3. A n-type bulk with n^+ and p^+ implants on the n- and p-side respectively leads to a p-n-junction between the p^+ implants and the bulk. The strips are covered with an insulating layer of silicon oxide and, on top of that, with aluminum readout strips. Therefore the readout is working via capacitive coupling which is necessary because of leakage currents induced by radiation.

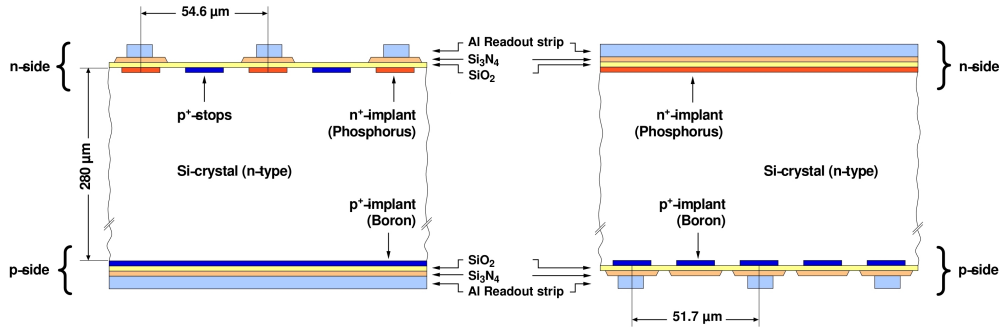


Figure 3.3: Cross section through a silicon wafer of the SINTEF design, modified from [24].

In order to minimize the risk of short-cuts through the bulk on the n-side, an insulation is necessary. This is implemented in the form of either p-stop or p-spray technology. While it is not possible to have both p-stops and intermediate strips at the same time for technical reasons, there is no such limitation with the p-spray technology. The latter design is the original one, done by the HLL while for the SINTEF design, the p-stop technology was chosen. Even though both versions are in use at COMPASS, the one with p-stops and no intermediate strips on the n-side is more common. The strips on the p-side have a pitch of $51.7 \mu\text{m}$, while the pitch on the n-side is $54.4 \mu\text{m}$. A bias ring distributes the bias voltage to the strips via 1M polysilicon resistors. Towards the edge of the sensor the potential needs to be dropped to the bulk level which is done via a multi-guard-ring structure composed of ten p^+ implanted concentric rings [13]. This design makes bias voltages up to 250 V^3 possible. For the COMPASS silicon detectors operated at 200 K, bias voltages of 90 to 160 V are sufficient to fully deplete the silicon bulk [46].

3.3.2 The Detector Module

The wafer described above is the heart of the COMPASS silicon detector module. A COMPASS silicon microstrip detector fully assembled (except for the cables) is shown in Fig. 3.4. It is kept in place by two L-shaped PCB⁴ Boards called *L-Boards* which are glued to the wafer. To reduce thermal stress, only one edge of every L-Board is glued to the wafer. The APV25 readout chips, introduced in Section 3.5, are glued to

³500 V for some

⁴Printed Circuit Board

3.3 Wafers and Detector Modules

the L-Boards. With 128 channels per chip, 10 chips for the long side and 8 chips for the short side are needed. The connection to the sensor is made via a pitch adapter which translates the strip pitch of the wafer to the analog APV input pitch of $44\ \mu\text{m}$. For temperature measurements three⁵ standard PT100 temperature sensitive resistors are glued to the detector as well as to the L-Boards.

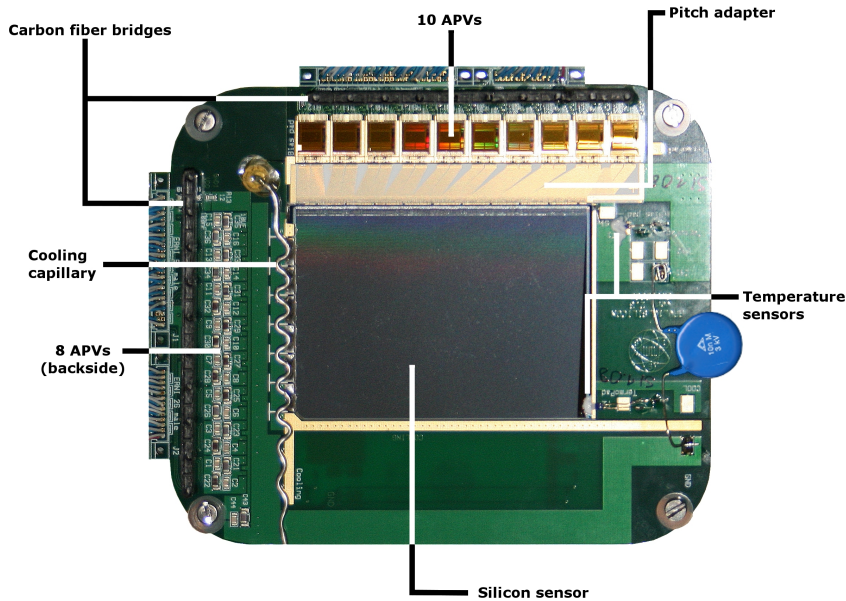


Figure 3.4: Silicon detector module, from [24]

So far the general design of the detector module was described. Several detectors of this basic type were in use at COMPASS since 2001 [35]. While the detector design was always subject to improvements, various changes to the original detector design had to be introduced especially for cryogenic operation (see Section 3.4). Carbon fiber bridges were added to increase the mechanical stability of the L-Boards. This is needed because the cooling to cryogenic temperatures causes thermal stress resulting from the different thermal expansion coefficients⁶ of the materials used, which could lead to the wafer cracking. As cooling medium either gaseous or liquid nitrogen is used. For non-cryogenic operation, gas was used, which only cooled the APVs and prevented temperatures in excess of $60\ \text{C}^\circ$. Liquid nitrogen cooling allows to cool both the APVs and the wafer, which can then be operated at $200\ \text{K}$, see Section 3.4.2. A thin capillary made from Alloy 400 bent into a wavy shape directs the nitrogen through the detector.

⁵1 on the wafer, 2 on the PCB

⁶ $3\ \text{ppm/K}$ compared to $14\ \text{ppm/K}$ for silicon and PCB respectively

The capillaries are soldered to the L-Boards on the opposite side of the APV, thermally decoupling them from the wafer. Historically, the shape was intended to reduce thermal stress, but cooling stability also profited from it. The reason for this being that the wavy shape favors turbulent flow enabling more efficient evaporation of the nitrogen. More details concerning the general design of the detector module are given in [34], while most changes concerning cryogenic operation are discussed in [12].

3.4 Cryogenic Operation

As [15] had shown, the charge collection efficiency (CCE) of irradiated sensors partially recovers for cryogenic operation, see Fig. 3.5. For that reason it was decided to operate the COMPASS silicon detectors with liquid nitrogen (LN_2) cooling. A complete cooling infrastructure as described in this section had to be set up. This includes vacuum-tight cryostats housing the detector modules as well as the nitrogen distribution circuit and monitoring and control equipment. As will be shown in Chapter 5, this decision had the additional benefits of a more stable readout, which is not subject to temperature fluctuations of the surroundings as well as an improved detector performance.

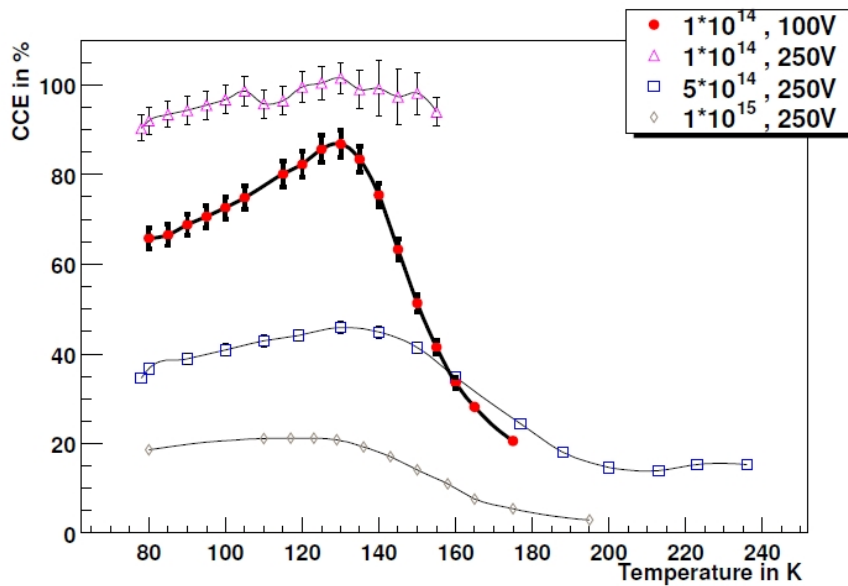


Figure 3.5: Charge collection efficiency for silicon detectors irradiated with various doses, from [15].

3.4.1 The Silicon Stations

One silicon *station*, referred to as $SI0\alpha$ (where $\alpha=1,\dots, 5$ up to now), is housing two detector modules. These modules are mounted back to back (long side is facing outwards) on one common stesalit frame (called shuriken for its form). The readout strips of the first module form an angle of 0° and 90° with respect to the COMPASS main coordinate system, see Section 4.1.1. The second module is rotated by 5° around the beam axis, hence four different projections, denoted as U,V,Y,X sorted according to their position in the direction of the beam axis, are measured by one silicon station. This is done to reduce ambiguities in the tracking. Depending on their purpose, two types of silicon stations are used in COMPASS. These types are now introduced.

Upstream Cryostat

The *upstream cryostats*, also called *beam stations*, were used in all COMPASS runs up to now. They are placed on an optical bench to conveniently adjust position and orientation of the cryostats and therefore of the detectors. Usually three upstream stations are used for beam definition, which is why the detectors are placed centrally in the beam. As the sensors are cooled to 200 K, it is necessary to operate them inside vacuum to avoid aggregation of ice leading to a destruction of the module. The inside of the cryostat has a volume of $240 \times 240 \times 82 \text{ mm}^3$ with the shuriken mounted at four precision holding points in the corners, which assures it being correctly aligned inside the cryostat. A schematic view of a closed upstream cryostat is shown in Fig 3.6. On the atmosphere side of the electrical feed-troughs the repeater cards described in Section 3.5 are mounted. The supply with liquid nitrogen is ensured via the nitrogen inlet on the top of the cryostat. This is a 300 mm long vacuum-insulated pipe, connected to the phase separator on the inside, see Section 3.4.2. The evaporated nitrogen from the phase separator is guided through the nitrogen outlet, after which a flow controller regulates the cooling. On the bottom of the cryostat several standard vacuum ports for the pump, the vacuum gauge and the venting valve are present. The front- and back-side of the cryostat are sealed with light tight *beam windows* with a carefully minimized material budget. The challenge of ensuring mechanical stability to secure vacuum operation with a low material budget was met by using aluminized mylar foil for its low mass density reinforced by a carbon fiber mesh on the inside. Using a standard turbomolecular vacuum pump a typical pressure of 10^{-5} mbar is reached.

Conical Cryostat

Housing two complete stations⁷, i.e. four detector modules used for vertex detection, the *conical cryostat* has been used during hadron runs since 2008. The name derives from its conical shape, designed to perfectly fit inside the inner scintillator ring of the RPD. The closer to the interaction point a detector is placed, the bigger is the angular

⁷SI04 and SI05

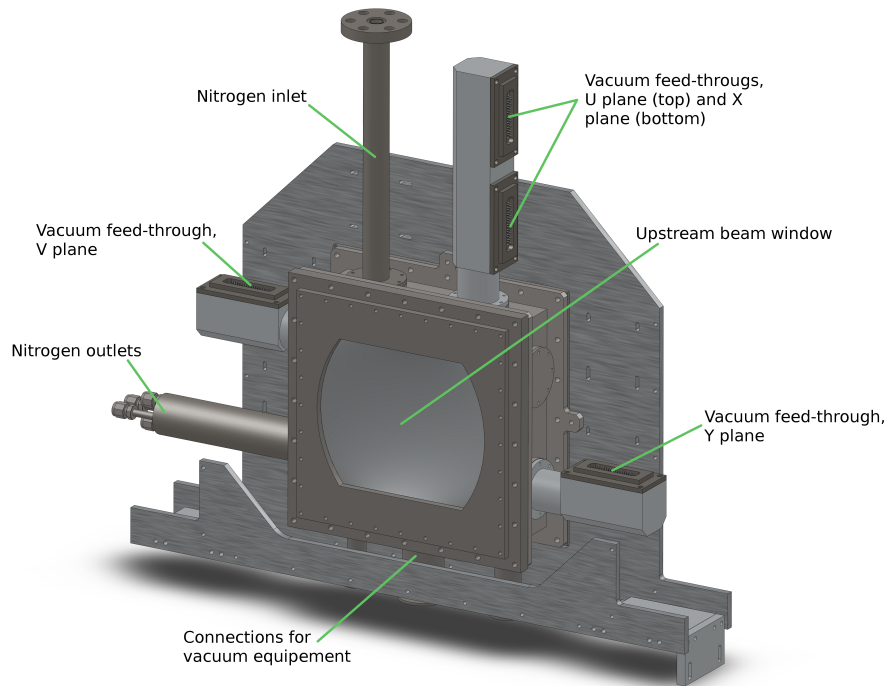


Figure 3.6: Upstream cryostat assembly, from [12].

acceptance region covered by its active area. On the other hand, the lever arm will become smaller, increasing the need for highest spatial resolution and precision alignment to detect scattering angles down to $50 \mu\text{rad}$. The conical cryostat played a central role in the hadron runs 2008/2009, which includes the Primakoff run in November 2009 (see Chapter 4). As the conical cryostat is inside the acceptance of the spectrometer, great care had to be taken to minimize the material budget inside. For this reason, special support frames from CRP⁸ were manufactured and in addition, the phase separator was moved from the cryostat itself into a separate box outside of the RPD. Because of its bigger volume, two vacuum pumps are needed for the conical cryostat, with an additional one for the phase separator box. The upstream and downstream caps of the conical cryostat are closed by removable beam windows made from CRP, again with the intention of minimizing the material budget. The conical cryostat with the front window removed and mounted silicon modules inside is shown in Fig. 3.7. All connections for the vacuum equipment as well as the Nitrogen in- and outlet are mounted on the downstream side of the conical cryostat.

⁸Carbon fiber Reinforced Plastics

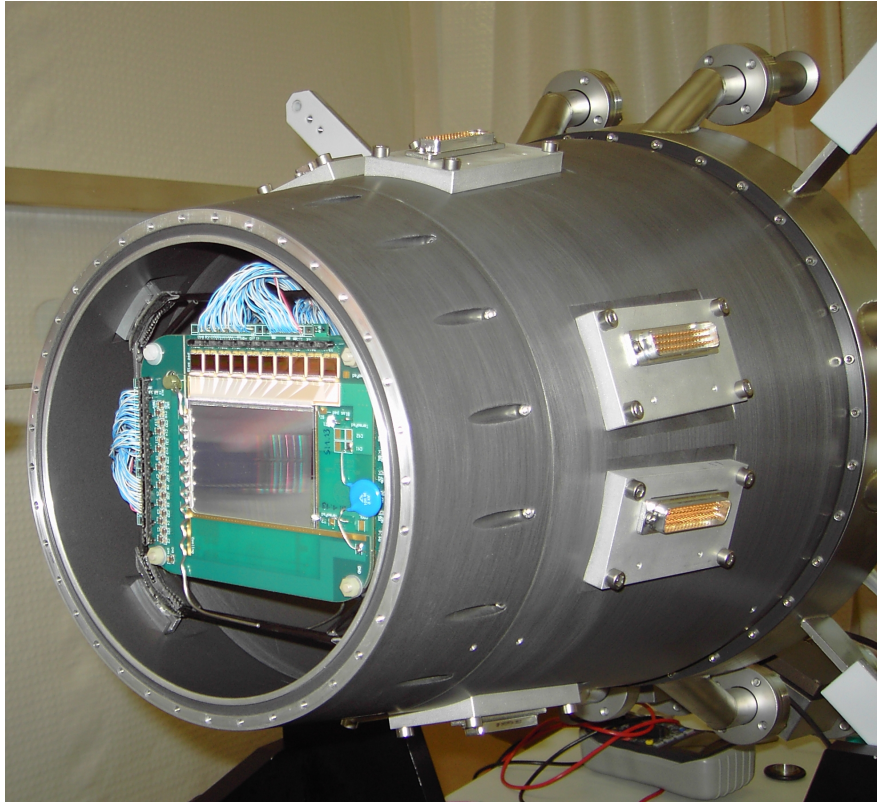


Figure 3.7: Open conical cryostat with mounted detector module.

3.4.2 Cooling Circuit

The simplified schematics of the cooling circuit is shown in Fig. 3.8. The silicon cooling system is connected to the central nitrogen dewar in front of the COMPASS experimental hall. From there, a large buffer volume inside the hall called *valve box* is supplied. The valve box provides a steady flow of liquid nitrogen for the silicon stations as shown in Fig. 3.8(a). The central piece of the valve box is a 50 l steel vessel inside an insulation vacuum and surrounded by a copper shield which is passively cooled by the exhausting gaseous nitrogen. Each station is connected via one vacuum-insulated transfer line, that is continuously pumped during operation. Between the valve box and the transfer lines, cryogenic valves are used allowing a coarse adjustment of the nitrogen flow. For steady and stable cooling these valves are not precise enough. Thus, outside the cryostats after each detector, flow controllers are used to regulate the cooling. These flow controllers are steered by a Siemens SIMATIC S7-300 PLC⁹. In addition all temperature, level and pressure sensors used in the system, are read out and processed by the PLC. During normal operation, the temperature deviation of the silicon sensors

⁹Programmable Logic Controller

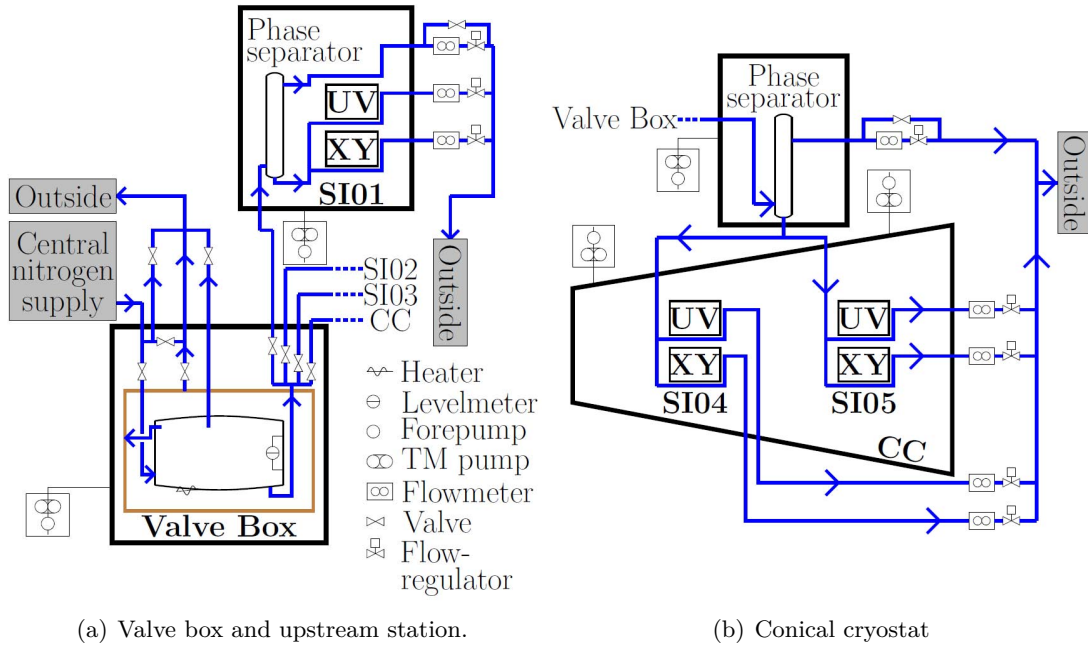


Figure 3.8: Simplified schematics of the cooling system of the COMPASS silicon detectors, from [3].

from the nominal value is lower than 2 K. Inside each station, a smaller buffer volume called phase separator is separating the already evaporated gaseous nitrogen from the liquid phase which is used to cool the detectors. The PLC is monitored and controlled by the software ANIBUS [19]. Various features allow to steer the system and to access previously recorded data conveniently.

3.5 Readout Chain

An overview of the readout chain is shown in Fig. 3.9. The different devices of the readout are described in this section in detail.

APV

The APV25-S1¹⁰ is an analogue pipeline ASIC¹¹ [41], originally intended for read-out of the silicon microstrip detectors in the CMS¹² tracker [28], but is now also widely used within COMPASS. Apart from the GEM, MM and RICH detectors, also silicon microstrip detectors are read out via the APV chip. Each chip supports 128 channels

¹⁰Analog Pipeline Voltage mode

¹¹Application Specific Integrated Circuit

¹²Compact Muon Solenoid

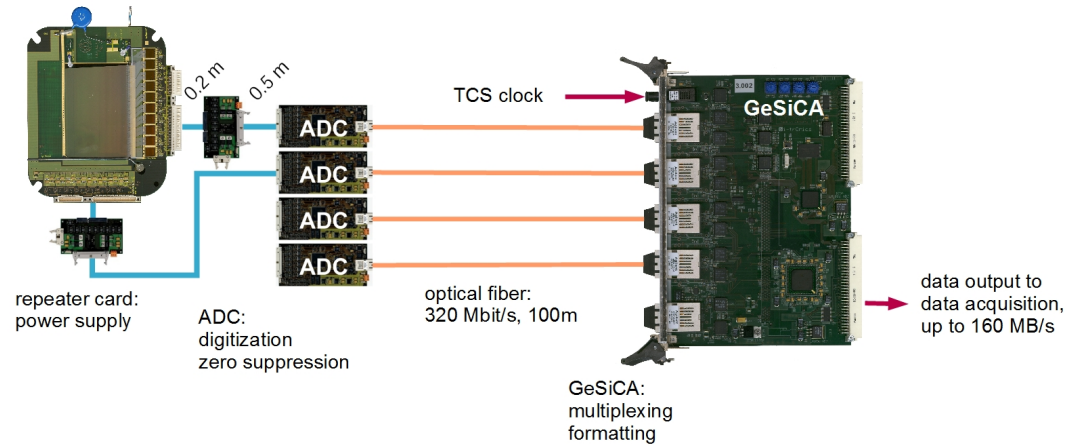


Figure 3.9: Overview of the silicon readout chain, from [12].

with a low noise CR-RC shaping amplifier and a 192 cell deep pipeline written at 38.88 MHz, the frequency of the COMPASS reference clock provided by the TCS¹³. Therefore a maximum latency of 4 μ s is possible. The pipeline is used to compensate for the latency of the trigger. The APV chip can be read out in Peak or Multi Mode. In Peak Mode only one amplitude sample is read out upon a trigger. This method can be used when pile-up is not significant. The APVs reading out the COMPASS silicon¹⁴ detectors are operated in Multi Mode where three consecutive samples are read out for each trigger. These three samples contain information about the pulse shape which is used to extract the time information more precisely, see Section 3.6.

Repeater Card

Thin ribbon cables of approximately 25 cm are connecting the detector modules with the vacuum feed-through connectors (see Section 3.4.1), to which the repeater cards are connected on the atmosphere side. Over these cables the APVs are supplied with power (± 1.3 V) as well as trigger and clock signals coming from the COMPASS TCS. In addition, separate lines for readout of temperature sensors are present, which are decoupled from the data stream. The analog data is repeated by high-speed operational amplifiers before being sent to the ADC¹⁵ card.

¹³Trigger Control System

¹⁴The same for the GEM detectors.

¹⁵Analog Digital Converter

ADC Card

A flat band cable connects the repeater card with the ADC card, called SGADC¹⁶. The incoming analog data is digitized by 10 bit differential ADCs at a sampling rate of 20 MHz¹⁷. One SGADC can handle up to 12 APVs, so one card is used for each silicon projection. Two FPGAs¹⁸ are doing the bulk of the data processing on the ADC card. An algorithm called *zero suppression* is reducing the data rate by rejecting information from channels containing only low amplitude noise. This algorithm subtracts the baseline called *pedestals* from the amplitude for each individual channel. These pedestals have to be recorded beforehand in a dedicated pedestal run and can be thought of as the average amplitudes with no signal present. Afterwards, the *common mode correction* is applied correcting for simultaneous fluctuation of all 128 channels of one APV chip, which can be caused by e.g. instabilities in the APVs' power supply. After baseline subtraction and common mode noise correction were applied to the current channel amplitudes, the remaining value is compared with the noise level of the channel, which was recorded together with the baseline. Only data from channels where the remaining signal is significantly higher than the noise level¹⁹ are sent via an optical fiber to the GeSiCA²⁰ module. A detailed description of the algorithms performed on the ADC is given in [36].

GeSiCA

The GeSiCA distributes the TCS clock as well as the trigger and reset signals to the ADC. The data stream of maximum four ADC cards is multiplexed into one serial data stream and the TCS event header²¹ is added, before the data are sent via an optical S-Link to the DAQ²². One GeSiCA is used per silicon station.

3.6 Data Reconstruction

This section covers the data reconstruction of the COMPASS silicon detectors. Starting from the detector raw data, time and spatial information is extracted.

3.6.1 Time Reconstruction

As already mentioned, the APV25 chip continuously samples the analog signals and as soon as a trigger arrives, three consecutive samples are marked for readout. The latency

¹⁶Silicon Gem Analog Digital Converter

¹⁷An upgrade to 40 MHz is foreseen.

¹⁸Field Programmable Gate Array

¹⁹Usually a factor of four the for silicon detectors.

²⁰Gem and Silicon Control and Acquisition

²¹Three numbers: The spill number during the run, the event number during the spill and a number identifying the event type.

²²Data Acquisition

is compensating for the trigger delay in a way that the rising edge of the signal coincides with the trigger time, however the latency can only be adjusted by multiples of the TCS clock period $\Delta=25.8$ ns. By using three consecutive samples, the time resolution can be refined to a few nanoseconds by pulse shape analysis. The trigger time is measured with respect to the rising edge of the TCS clock which makes it convenient to define the *TCS Phase*:

$$t_{\text{TCS phase}} = t_{\text{TCS clock}} - t_{\text{trigger}} \quad (3.2)$$

The consecutive samples read out are denoted by a_i ($i=1,2,3$) and fulfill the relation

$$a_0 = A(t - 2\Delta) \quad a_1 = A(t - \Delta) \quad a_2 = A(t). \quad (3.3)$$

where $A(t)$ denotes the amplitude of the channel at the time t . These amplitudes depend on the energy loss of the particle traversing the active detector volume. By calculating the ratios between the amplitudes the dependence on the absolute value of the amplitude is removed. Furthermore, it is assumed that the signal shape factorizes in a time dependent function and a time independent factor, so when considering the ratio, also the time dependence drops out. The ratios are defined as:

$$r_0 = \frac{a_0}{a_2} \quad \text{and} \quad r_1 = \frac{a_1}{a_2} \quad (3.4)$$

The dependence of the signal timing functions on the TCS phase can be extracted by using experimental data only, removing the necessity of a theoretical model describing the properties of the electronic circuits. The time dependence of r_0 and r_1 is shown in Fig. 3.10. It can be parametrized using [30]

$$r(t) = r_0 \cdot \exp[-\exp[-s(t')]] \quad (3.5)$$

$$\text{with} \quad s(t') = \frac{a+c}{2} \cdot t' + \frac{a-c}{2} \left(\sqrt{t'^2 + b^2} - |b| \right) + d \quad (3.6)$$

$$\text{and} \quad t' = t - t_0. \quad (3.7)$$

During the calibration process, the parameters of Eq. 3.6.1 have to be extracted from experimental data that are recorded in a specific latency scan at the beginning of every years run. The specifics of the calibration process have been discussed in great detail in [61]. The parametrization mentioned above offers a sufficient number of degrees of freedom to reproduce the observed signal shapes in cryogenic as well as non-cryogenic operation. In the reconstruction, it is of great benefit that $r(t)$ as given in Eq. 3.6.1 is analytical and can be inverted. This permits to perform exact error propagation of the amplitude error through the whole reconstruction process to obtain the correct error of the measured time. This concept was first implemented in the COMPASS online filter Cinderella [51]. The inverse of Eq. 3.6.1 as used in the reconstruction process is given by

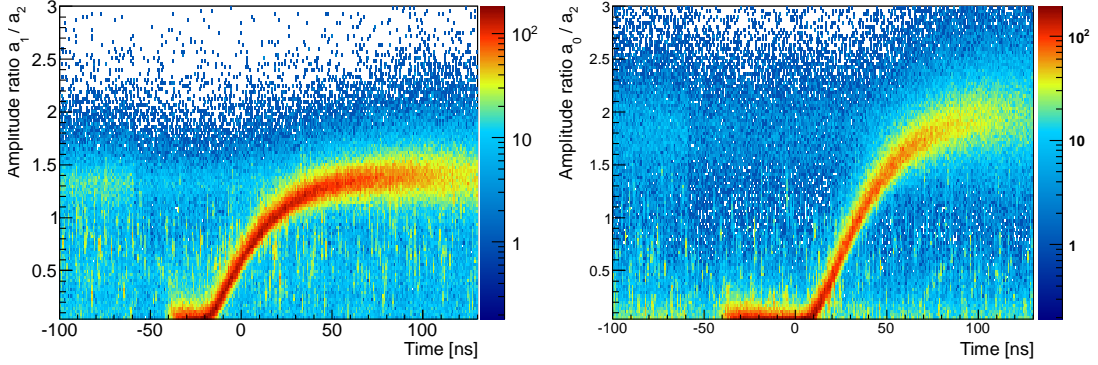


Figure 3.10: Time dependence of r_1 and r_0 obtained in the latency scan for the 2010 beam time.

$$t(r) = t_0 + s^{-1} \left(-\log \left[-\log \left(\frac{r}{r_0} \right) \right] \right) \quad (3.8)$$

$$\text{with } s^{-1}(x) = \frac{1}{2ac} \left[(a+c) \cdot f(x) - (a-c) \cdot \sqrt{f(x)^2 + acb^2} \right] \quad (3.9)$$

$$\text{and } f(x) = x - d + \frac{|b|}{2} \cdot (a-c). \quad (3.10)$$

With the ratios r_0 and r_1 two independent sources per strip for the extraction of the signal time are at hand. Both values are then combined to one strip-time taking into account their individual error. From the pedestal measurement, one knows the uncertainty of the measured amplitudes σ_a , which is propagated to the total uncertainty σ_{r_x} of a ratio r_x via

$$\sigma_{r_x} = \frac{a_x}{a_2} \sqrt{\left(\frac{\sigma_a}{a_x} \right)^2 + \left(\frac{\sigma_a}{a_2} \right)^2} = \frac{\sigma_a}{a_2} \sqrt{a_x^2 + a_2^2}, \quad x \in \{0, 1\}. \quad (3.11)$$

To account for the strong curvature of $t(r)$ (see Fig. 3.10) one has to split up the error σ_{t_x} into an upward $\sigma_{t_x}^+$ and a downward error $\sigma_{t_x}^-$ with

$$\sigma_{t_x}^+ = t_x(r) - t_x(r + \sigma_{r_x}) \quad \text{and} \quad \sigma_{t_x}^- = t_x(r - \sigma_{r_x}) - t_x(r). \quad (3.12)$$

The two signal time values can be combined to one strip-time t by calculating the mean value of t_0 and t_1 , each weighted with the appropriate error. The error σ_x on the time t_x is chosen from the asymmetric errors towards the other time measurement in the following way:

$$\sigma_0 = \begin{cases} \sigma_{t_0}^+ & \text{if } t_0 < t_1 \\ \sigma_{t_0}^- & \text{otherwise} \end{cases}, \quad \sigma_1 = \begin{cases} \sigma_{t_1}^- & \text{if } t_1 > t_0 \\ \sigma_{t_1}^+ & \text{otherwise} \end{cases} \quad (3.13)$$

The combined time t can then be written as

$$t = \frac{t_1\sigma_0^2 + t_0\sigma_1^2}{\sigma_0^2 + \sigma_1^2}. \quad (3.14)$$

One can show the asymmetric errors of the combined strip-time to be

$$\sigma_t^+ = \frac{1}{\sqrt{\frac{1}{(\sigma_{t_0}^+)^2} + \frac{1}{(\sigma_{t_1}^+)^2}}} \quad \text{and} \quad \sigma_t^- = \frac{1}{\sqrt{\frac{1}{(\sigma_{t_0}^-)^2} + \frac{1}{(\sigma_{t_1}^-)^2}}} \quad (3.15)$$

The cluster finding algorithm described in Section 3.6.2 is relying on the strip time information and the correct error propagation.

3.6.2 Cluster Finding

Identifying Clusters

The clustering algorithm called *Cinderella clustering* was originally developed in the scope of the COMPASS online event filter [51]. As a first step, the algorithm combines all adjacent strips where the amplitude exceeds the noise level, to so-called *regions*, that are cluster candidates. Usually, several of these regions are found for each triggered event and projection. At this stage, only the amplitude information is used, leading to a high number of accidental clusters. For example, particularly noisy channels can easily be added to a real cluster and distort the position information, or several neighbouring noisy channels can be combined to a cluster candidate without any particle crossing the detector at this position. Here the time information and the propagated error can help to put things right. For each region, the adjacent strips are successively checked if their time information under consideration of the errors is consistent. This is equivalent to the time difference of two strips being consistent with zero. One can therefore define a consistency criterion in the following way:

$$Y = \frac{|t_2 - t_1|}{\sqrt{\sigma_1^2 + \sigma_2^2}} < Y_{\text{cutoff}}. \quad (3.16)$$

Y_{cutoff} is the most important parameter in the clustering algorithm. Typically, a value of $Y_{\text{cutoff}}=3.5$ was chosen in [51], but a more detailed discussion of the implications of this decision will be given in Section 6.1. The errors σ_1 and σ_2 are chosen from the asymmetric errors of the strip-time (see Eq. 3.15) analog to Eq. 3.13, i.e. towards the other time.

The cluster finding algorithm does not limit the size of a cluster. Adjacent strips are combined iteratively as long as the amplitude exceeds the noise level and the time information of the strips is consistent. To some extent, the algorithm is capable of separating noisy channels from real clusters in this manner and adjacent noisy channels can be identified by their inconsistent time information. The width of the charge cloud in the silicon is around 5-10 μm [57], i.e. significantly smaller than the readout pitch.

Therefore the typical number of strips in a cluster, as expected from diffusion inside the silicon bulk and charge sharing between readout strips, is one or two. The fraction of double-strip clusters is an important quantity to describe the detector performance, because in this case the spatial resolution improves drastically (see Section 5.2). However also clusters composed of three or four (even up to twenty in rare cases) strips are observed in the data. The clusters larger than five strips are solely created by high energy δ -electrons, whereas for smaller clusters there is also a chance of two particles crossing the detector in close proximity with respect to each other, therefore creating overlapping clusters. An extension of the Cinderella clustering dealing with all clusters composed of three or more strips is presented in Chapter 6.

Calculation of Cluster Position

For each cluster identified in the previous step, the position has to be calculated. This is trivial for clusters composed of one strip, where the position of the center of the strip is assigned as the cluster position. For clusters composed of more than one strip the *Center-of-Gravity method* is applied, weighting the position X_i of the strip i with the recorded amplitude sample $a_{2,i}$. The effective strip number X_{CoG} is calculated via

$$X_{CoG} = \frac{\sum_i a_{2,i} X_i}{\sum_i a_{2,i}}, \quad (3.17)$$

also including the special case of a single-strip cluster.

The charge diffusion process is highly nonlinear but can be studied on experimental data. For double-strip clusters the quantity η , which is the fractional charge seen on strip n divided by total cluster charge is of great benefit:

$$\eta = \frac{a_{2,n+1}}{a_{2,n} + a_{2,n+1}} \quad (3.18)$$

Typical charge sharing distributions are shown in Fig. 3.11. Numerical artifacts stemming from the division of two integers have been removed by randomizing the amplitudes with ± 0.5 . For a projection with intermediate strips a charge sharing factor of 0.5 is clearly favored as shown in Fig. 3.11(a). Via capacitive coupling both strips see a comparable amount of charge. For detectors without intermediate strips, a charge distribution between the strips, where the main part of the total charge is collected on one strip is clearly favored, see Fig. 3.11(b). Comparing the charge sharing distribution of the cold silicon detectors with the warm detectors used in 2004, as shown in [24], one can clearly see that a reduction of the noise also enhances the η -distribution at very low and high values. At these values of η , the main part of the total charge is collected on one strip, leaving an amount of charge on the second strip which is comparable to the noise level. With an overall higher noise level as during non-cryogenic operation, it is more likely that these strips will be sorted out during the zero suppression. For example, $\eta = 0.1$ is already strongly suppressed with warm detectors, while still significantly present with the detectors operated cryogenically. A more detailed comparison

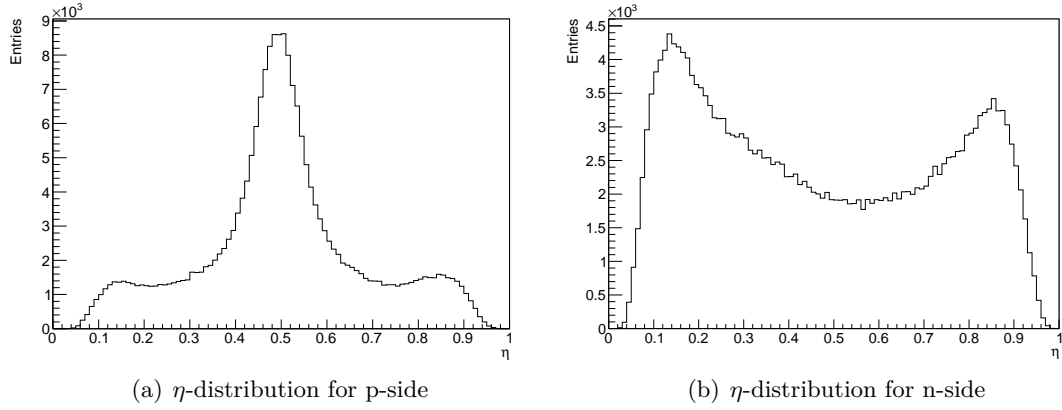


Figure 3.11: Charge distribution for a sensor with intermediate strips (a) and without intermediate strips (b).

between the performance of warm and cold detectors is given in Section 5.5.

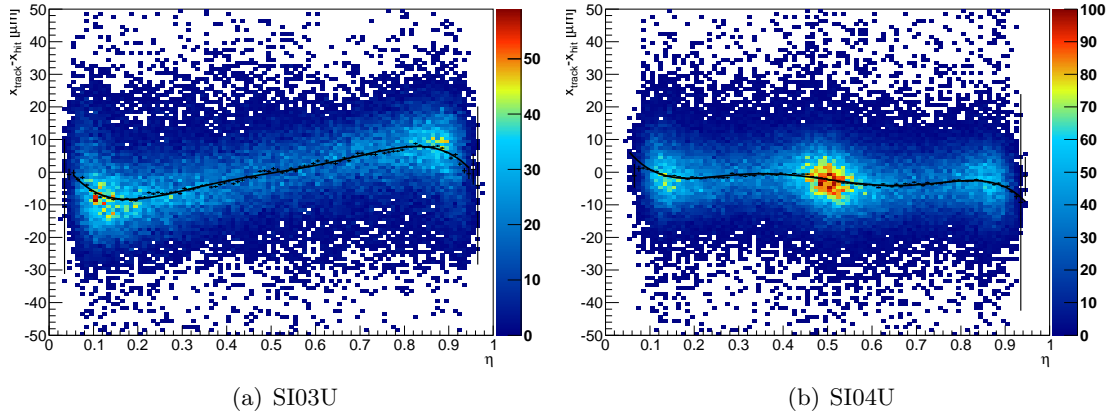


Figure 3.12: Residual distribution versus charge sharing factor η for a plane without (a) and with (b) intermediate strips. For the data shown the η -dependent position corrections were deactivated.

Charge sharing is a non-linear process, because for a linear process Fig. 3.11(b) would be a flat distribution. For that reason, Eq. 3.18 is not the optimal way of determining the cluster position. One can correct for the non-linearity in the case of double-strip clusters by plotting the difference of the track position, as given by the tracking, and the cluster position calculated according to Eq. 3.18 versus η . As shown in Fig. 3.12, the average residual as a function of η varies over $10 \mu\text{m}$ within the range of η . The

Chapter 3 The Silicon Microstrip Detectors for COMPASS

distribution of the average residual can be fitted using 6th and 4th order polynomials in η for sensors with and without intermediate strips respectively. During the clustering method in CORAL, the cluster position of all double-strip clusters is corrected with the corresponding value.

Chapter 4

Alignment for the Primakoff Run 2009

The Primakoff measurement is experimentally challenging, demanding the full performance of the COMPASS silicon microstrip detectors. This includes a highly accurate detector alignment with a precision better than the spatial resolution. In the beginning of this chapter, the principle of the COMPASS alignment procedure is introduced. Next, the special requirements for a successful Primakoff measurement are reviewed, followed by a presentation of several discovered alignment problems. Finally, the run-by-run alignment proceeding and the improvements compared to the initial situation are described.

4.1 The Alignment Procedure

The problems presented in Section 4.3 are all related to some kind of misalignment of the COMPASS spectrometer. For that reason the COMPASS spectrometer alignment procedure shall be introduced in this section, which is done via a summary of [55]. The emphasis is not on a mathematical derivation but to procure the basic idea, which will be requisite for the rest of this chapter.

4.1.1 Coordinate Systems and Formalism

The COMPASS *main reference system* (MRS) will be denoted by $(Oxyz)$, where the z axis is positive and in the direction of the beam, y is pointing vertically upwards and x is chosen in way that the coordinate system is right handed. The origin O was once chosen to be at the target center, but is now on an arbitrary position along the beam axis due to changes in the spectrometer setup. The target position of the Primakoff Ni target in 2009 is roughly at -73 cm.

In addition there is one *wire reference systems* (WRS) for each detector plane in the COMPASS spectrometer. It is denoted by $(O'uvz)$ where the z axis is according to the MRS, u is chosen to be in the measured direction and v orthogonal to it. The origin O' is defined by the intersection point of the beam with the detector plane.

In this Chapter all numerical values in the MRS will be given in cm, for the WRS μm is chosen as basic unit.

During the alignment procedure tracks are approximated as straight lines in the absence of a magnetic field, neglecting multiple scattering and other interactions in the

spectrometer. The full COMPASS alignment procedure also includes a step during which magnetic fields are present. This shall be omitted here, since it is non-relevant for the conducted analysis but details can be found in [55]. Therefore the mathematical representation is reduced to four parameters per track. These are usually chosen to be a space point (x_0, y_0) at a specified detector plane and the slope with respect to z $(m_{x,0}, m_{y,0})$ in the xz and yz plane respectively.

4.1.2 The Principle

The starting point for the spectrometer alignment is the surveyors measurement, which has a precision of 0.5 mm at the level of one sigma [32]. Within the alignment procedure, corrections are derived to these positions, which result in the optimal spectrometer geometry for the track reconstruction. The desired accuracy is usually one tenth of the detectors resolution, i.e. hundred μm for most detectors and better than 1 μm for the silicon detectors. The optimization is based on the minimization of the total χ^2 , which is the sum over all χ_i^2 for all tracks in a given sample of size N :

$$\chi^2 = \sum_{i=1}^N \chi_i^2 \quad (4.1)$$

Each contribution added in Eq. 4.1 depends on a different set of track parameters, which are identical for the complete spectrometer. In contrast, all contributions depend on the same set of alignment parameters. The alignment parameters are the corrections to the surveyors position and in COMPASS usually four different terms per plane are calculated:

- δu : The displacement of the detector plane along the u axis.
- $\delta\theta$: The rotational offset in the WRS.
- δz : The displacement along the beam axis.
- δp : Corrections to the nominal pitch.

The quality of a given set of alignment parameters, i.e. the just mentioned parameters for each of the roughly 200 detector planes within COMPASS, can be evaluated applying various quality criteria. These criteria can be divided into two groups: *relative criteria*, like the number of reconstructed tracks per event are not suitable for a minimization, since their final values for a optimum alignment are unknown. Nevertheless, they present an easy way to directly compare two given sets of alignment parameters. *Absolute criteria* are based on the residual distribution of a given detector plane, where the *residual* is defined as follows:

$$\Delta u = u_{track} - u_{cluster} \quad (4.2)$$

Each of the above given alignment parameters can be related to an expression in Δu :

4.2 Requirements for the Primakoff Run

- $\delta u \leftrightarrow \langle \Delta u \rangle$
The average value of u is sensitive to the detector displacement along the u axis.
- $\delta \theta \leftrightarrow \partial \langle \Delta u \rangle / \partial v$
The distribution of the average of u versus the position perpendicular to the measurement axis as extracted from the tracking, is sensitive to rotational offsets of the detector plane.
- $\delta z \leftrightarrow \partial \langle \Delta u \rangle / \partial u$
The distribution of the average of u versus the track position in the direction of the measurement axis as extracted from the tracking, is sensitive to a displacement of the plane along z . This however is strongly correlated to a uncertainty of the pitch δp for tracks originating from one point, i.e. usually the target.

During the alignment procedure the correction values are determined for all planes simultaneously in a way, that $\langle \Delta u \rangle$, $\partial \langle \Delta u \rangle / \partial v$ and $\partial \langle \Delta u \rangle / \partial u$ are minimized. One track is not sufficient to align the complete spectrometer. Thinking of a track sample of size 1000, and 3 alignment parameters for each of the roughly 200 detector planes in the COMPASS spectrometer, minimizing Eq. 4.1 requires inverting matrices of the size ≈ 5000 . This task is not straight forward, but according to [14] the matrices have a block structure with a large number of zeros which can be taken advantage of. The matrix size is reduced down to the number of alignment parameters, which is still large but independent of the considered track sample.

4.2 Requirements for the Primakoff Run

For the Primakoff measurement, precision tracking is needed to reconstruct scattering angles of the scattered pions down to $100 \mu\text{rad}$ [59]. This number can be derived starting from a transverse momentum transfer (p_T) resolution of about $10 \text{ MeV}/c$ given by the multiple scattering in the target and 100 GeV for the highest-energy pions used in the analysis [52]. The silicon detectors downstream of the target are SI04/SI05, placed inside the conical cryostat (CC). The distance from the target is roughly 1 m and according to [29], systematic effects have to be excluded down to a factor of 10 in the pions scattering angle. This transfers into a maximum misalignment of $\Delta u_{max} = 10 \mu\text{m}$ for the silicon detectors inside the CC.

4.3 Troubleshooting

At the beginning of November 2010 abnormalities in the vertex distribution were discovered by [38]. The distribution of the z coordinate of all reconstructed vertices of the production T38 is shown in Fig. 4.3(a). The main peak presenting the Ni target at roughly -73 cm seems to be composed of two components which can be approximated by two Gaussians. Problematic is the fact, that the Gaussian means show an significant

relative offset of about 0.7 cm. In addition, several artifacts without a representation in the spectrometer were found in the vertex distribution, for example $z=-93$ cm and $z=-3.4$ cm. As shown in [61] some of the problems can be cured by shifting the z position of the conical cryostat roughly 2.5 cm downstream. Even though this shift improved the reconstruction efficiency and the vertex resolution, it was clear that in principle a shift of this magnitude is forbidden by the geometric knowledge of the RPD and CC and therefore the solution could only be viewed as temporary. Nevertheless, these studies provided valuable insight into the nature of the problem. Besides, up to then unsolved alignment problems between silicon and the Micromegas detectors were pointed out by [7].

4.3.1 Silicon Detectors

Offset

First of all, the alignment of the silicon detectors was investigated according to the requirements mentioned in Section 4.3. Therefore, the zone definition in CORAL was changed in a way, that the first zone includes only silicon detectors and FI01. The second zone starts just after the CC. This way a silicon-only tracking with straight trajectories¹ could be performed, providing an optimal tool to evaluate the intra silicon alignment. FI01 was switched off during the tracking and additionally the bridging step from the target zone (now containing all silicons) to the first zone (now starting right after the CC) was skipped in order not to project other possible problems into the silicon alignment. The silicon detectors were divided into two groups² in alternating order along the beam axis. Using only one set while deactivating all other silicon detectors, the unbiased residuals of the switched off planes can be obtained. Tracks where an interaction took place in the target region were excluded by performing a χ^2 cut. This works, because no vertex finding is attempted within a zone and tracks with a kink as created from an interaction can hence not be reconstructed reasonably using a straight line. This way for three runs $\langle \Delta u \rangle$ for all silicon planes was determined. The results are summarized in Table 4.2. The used alignment file is based on the run 81686. The largest deviation observed is $40 \mu\text{m}$, which is more than four times the detector resolution. Since this run started shortly after midnight while the alignment run started on 6:35 p.m., a day-night correlation of the displacements is assumed. The changing displacements can be explained by temperature changes and the resulting thermal expansions of support structures made from aluminium for the CC and the optical bench in case of the beam telescope. During the reconstruction, these large detector displacements were compensated by special CORAL options which account for alignment uncertainties by enlarging the route width³ (see Section 2.4.1) by $50 \mu\text{m}$ and the position uncertainty⁴ by $40 \mu\text{m}$. This implies inevitably an increased probability

¹No magnetic field present around the nuclear targets.

²SI01XY, SI02UV, SI03XY, SI04UV, SI05XY and SI01UV, SI02XY, SI03UV, SI04XY, SI05UV

³TraF dCut [84]

⁴TraF dCut [85]

to pick up uncorrelated hits in tracks. In the end, this caused the main part of the artifacts in the vertex distribution, since only a small fraction of the potential of the silicon vertex detectors was actually utilized. This also triggered a reinvestigation of the silicon detector performance, presented in Chapter 5. To make full use of the potential and to fulfill the demanding requirements of a Primakoff measurement, a run-by-run alignment is necessary. Up to that point, alignment runs were performed weekly or even more infrequent. For the complete Primakoff period which lasted 14 days, only one alignment file was foreseen at the beginning [46]. Purpose of a run-by-run alignment is to provide a distinct alignment file for each run of the Primakoff period. This task was accomplished by [7], the applied procedure is briefly described in Section 4.3.3.

Table 4.1: Alignment summary for three runs from the Primakoff data taking period 2009. The maximal and minimal deviation for X-like and Y-like detectors is shown. The last column shows the maximal movement of planes between the considered runs. The used alignment file is based upon run 81686 which started at 05/11/09 6:35 p.m. All used start times are taken from [46].

Run	Start time	Type	$\langle \Delta u \rangle_{min}$ [μm]	$\langle \Delta u \rangle_{max}$ [μm]	Shift [μm]
81971	12/11/09 14:40	x	0.3	- 5.0	—
		y	0.6	- 5.9	2.7
82006	14/11/09 15:00	x	1.0	- 7.1	4.6
		y	0.1	- 5.3	16
82144	18/11/09 00:40	x	1.7	- 40.0	40
		y	0.6	- 18.0	—

The Pitch

In addition, the exact silicon pitch had to be found. In principle, the design values of the silicon detector pitch are one the best known dimensions (in absolute terms) in the COMPASS experiment. However changes in the order of one per mill cause already severe problems. Therefore the design pitch of $54.677 \mu\text{m}$ and $51.750 \mu\text{m}$ for p and n side respectively, has to be known better than $0.05 \mu\text{m}$. This comes from the fact, that the position of the strips are calculated by multiplying the pitch with the strip number. The long side of the detector has 1280 strips, which means an absolute offset of $35 \mu\text{m}$ for the central strip, supposing an uncertainty of the silicon pitch at the per mill level. A displacement of $35 \mu\text{m}$ is indeed more than half of the readout pitch and roughly 5σ of the detector resolution. As a result, uncertainties in this order of magnitude could not be tolerated. The challenge gets even more complex, since for a set of tracks originating from the same point, i.e. the target, a wrong pitch δp can not be distinguished from a wrong z position δz . This ambiguity is usually disentangled by using tracks parallel to

the beam axis for the z position and a set of radial tracks originating from the target to obtain corrections to the pitch. However COMPASS is a fixed target experiment, which causes a strong boost of all outgoing particles restricting the outgoing tracks to small track angles. In the end, the pitch of two silicon detectors was fixed at the design values minus a correction for the thermal contraction⁵, while all other silicon pitches were initialized at the corrected design value but were subject to the minimization. The corrections are in the order of per mill, which can be attributed to small displacements in the beam direction or at this level of precision even uncertainties in the design values. Two detectors have to be fixed, to compensate for global transformations: adjusting all pitches at the same time favors a reduction of all pitches, since this way the χ^2 of all reconstructed tracks can be reduced. The fixed values act as an anchor preventing for this downscaling of the silicon detectors. For the same reason, the rotational correction of one plane has to be fixed, otherwise the whole silicon telescope could rotate around the beam axis.

4.3.2 The Micromegas Pitch

With twelve planes between the target and SM1 and a nominal spatial resolution of $100\ \mu\text{m}$ the Micromegas detectors, introduced in Section 2.3.2, exhibit a strong weight in this zone, and a misalignment would inevitably degrade tracking performance for angles above $10\ \text{mrad}$. This is roughly the minimum angle with respect to the beam axis needed for a track originating in the target to hit the active area of the MM detectors. Having fixed the properties of the silicon beam telescope as well as the vertex detectors, the precision of the silicon vertex detectors was used to study the alignment of the Micromegas detectors. The zone definition was reset to the standard configuration, leaving SI04 and SI05 as the only silicon detectors behind the target. All other detectors between the target and SM1 were switched off during the tracking and no bridging over the target or SM1 was performed. This way the full precision of the silicon vertex detectors as obtained after the modifications described in Section 4.3.1 could be used without possible other interfering sources of uncertainties. Since in standard tracking condition the redundancy in the region between the target and SM1 is used, standard reconstruction options for the prepattern require more hits than SI04 and SI05 can actually provide. This was changed in the CORAL options file, the corresponding options are given in App. B.1, and compensated during the analysis by requiring a hit in all eight silicon planes downstream of the target and using only highly precise tracks with $\chi^2/NdF < 2$, see Fig. 4.1. A PHAST userfunction extrapolates the tracks to the various MM planes and the track parameters are transformed into the WRS.

This is shown for all planes of station MM01 in Fig. 4.2. The local peaks in intensity are caused by the beam in combination with the central dead zone of the MM's which has a diameter of $5\ \text{cm}$. Due to the limited active area of SI04 and SI05 the outer regions of the MMs cannot be illuminated, because of the geometrical constraints. The average

⁵The effect is in the order of $-2 \cdot 10^4$ for silicon at 200 K.

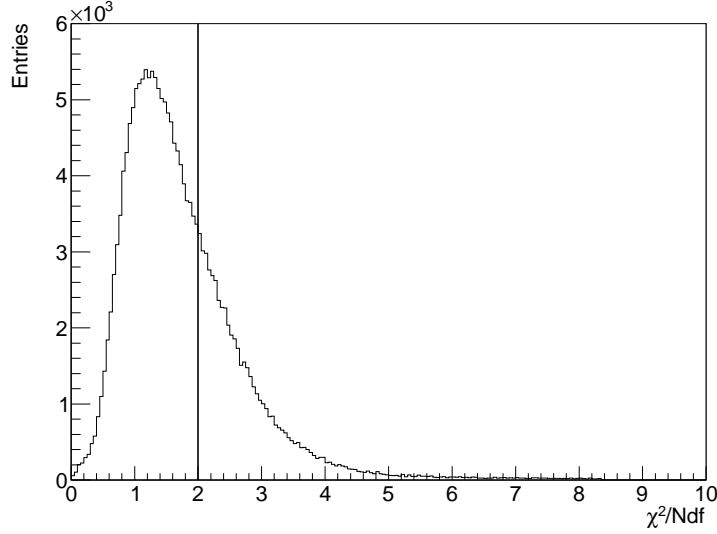


Figure 4.1: χ^2 distribution of tracks reconstructed with SI04 and SI05 only.

residuum for each bin was obtained using the ProfileX() method [16] implemented in ROOT. The obtained points were fitted using a straight line where the slopes can be attributed either to a displacement in z or a wrong pitch. Under the assumption that all tracks originate from the target, the displacement in z can be calculated by:

$$\Delta z = -\frac{\partial \langle \Delta u \rangle}{\partial u} \cdot |z_{\text{plane}} - z_{\text{target}}| \quad (4.3)$$

A negative slope corresponds to a shift downstream and the other way round. Shifts in the direction of z in the order of half percent are forbidden due to geometrical constraints of the mechanical structures as pointed out by [47]. The ambiguity between δz and δp cannot be resolved within the used method, because tracks that are parallel to the beam axis after the target, will in most cases hit the dead zone of the MM. For straight tracks coming from the same point, both parameters are related by:

$$\delta p = \frac{\delta z}{z} \quad (4.4)$$

Checking the used alignment file⁶ revealed deviations from the design pitch⁷ in the order of $1 \mu\text{m}$, i.e. $\approx 0.3\%$ were found. These were realigned by [7] starting from the design values and introducing shifts along the beam axis in the order of a few mm. This improved the situation in a way, that a relative alignment between the silicon and the

⁶detectors.81686.hadron.dat v.1.12

⁷ $360 \mu\text{m}$ for central part and $420 \mu\text{m}$ for the outer part

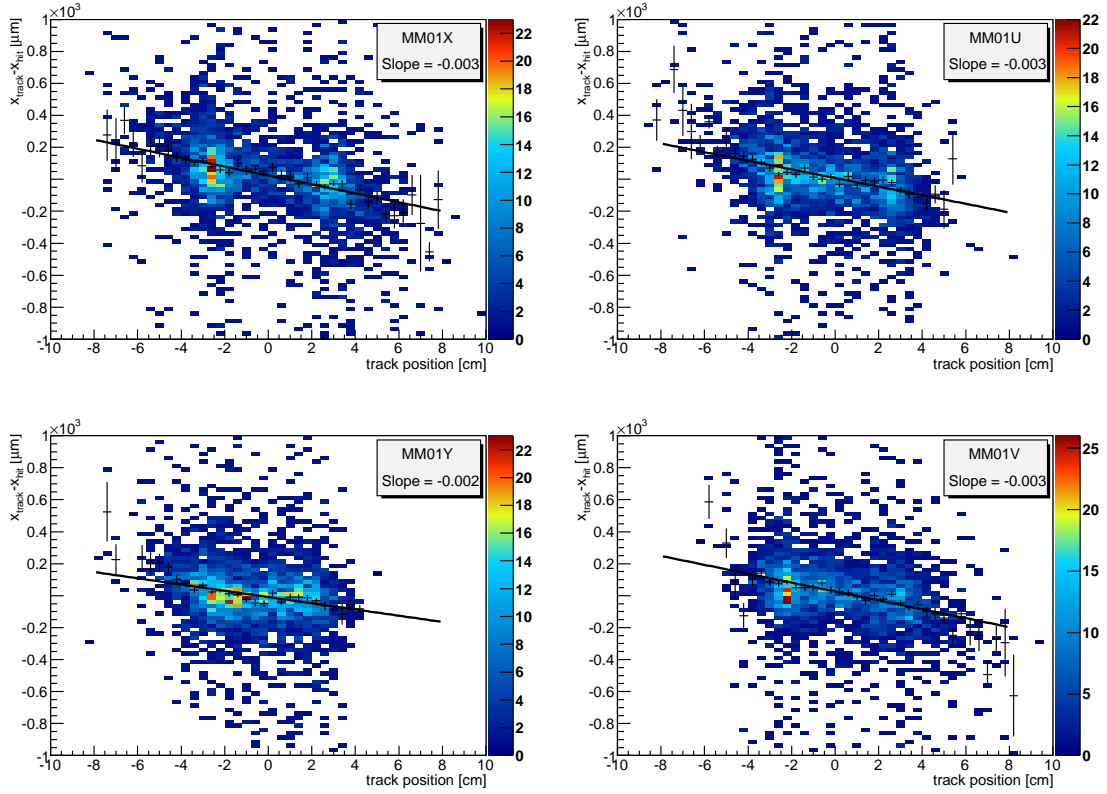


Figure 4.2: Residual versus track position measured in WRS for the four projections of MM01. The average residual as a function of the track position was fitted with a straight line.

Micromegas detectors could be performed successfully. The positive effects on the data quality are discussed in Section 4.4.

Table 4.2: Summary of the obtained slope for all MM planes.

$\partial\langle\Delta u\rangle/\partial u$	MM01U	MM01V	MM01X	MM01Y
	-0.003	-0.003	-0.003	-0.002
$\partial\langle\Delta u\rangle/\partial u$	MM02U	MM02V	MM02X	MM02Y
	-0.002	-0.001	-0.002	-0.001
$\partial\langle\Delta u\rangle/\partial u$	MM03U	MM03V	MM03X	MM01Y
	-0.002	-0.000	-0.000	-0.000

4.3.3 Run-by-Run Alignment

This part is dedicated to a description of the run-by-run alignment devised by [7]. The base is a standard physics alignment produced for one of the the first runs of the Primakoff period. The only special feature is to fix the silicon pitch at the design values. The zone definition in CORAL is again changed to have a zone which only contains silicons and FI01. For each run anew, this zone is aligned keeping the rest of the spectrometer fixed. The orientation of this enlarged silicon telescope with respect to the rest of the spectrometer is secured by activating bridging over the target, although in this zone configuration, the bridging occurs somewhere behind the target. In this step, the silicon pitch is a free parameter for all silicon stations but SI01XY and SI03XY. In addition, the angle of SI04XY is fixed because using the bridging can not prevent for a scaling of all silicon planes as well as a rotation around the beam axis. The changes in the pitch are extremely small, considerably below the per mill level, presumably compensating for minimal misalignment in z . The corrections obtained within the run-by-run alignment over the time are shown in Fig. 4.5.

4.4 Results

In this section, the results of the performed alignment improvements will be discussed. The analysis was restricted to interaction points of Primakoff-like events. This means, vertices formed from the beam particle as measured by the silicon beam telescope and only one outgoing particle. Since this is the most demanding scenario in terms of the determination of the interaction point, problems will occur first in this topology. Furthermore, showing a good performance for the one outgoing particle case, even better performance for other charged channels can be expected. Figure 4.3(a) shows the distribution of the z coordinate of all reconstructed vertices for run 81819 from the production T38 for which the before mentioned shortcomings in the vertex finding were discovered. In contrast, Fig. 4.3(b) shows a test production where a completely new alignment was used and tracks were bridged over the target. Probably the most striking feature is the immense reduction of background. This can be attributed to the additional bridging step, as it allows for straight tracks through the target. This means, whenever two track segments up- and downstream of the target are compatible with a straight line, it is assumed that no interaction apart from multiple scattering took place and both segments are bridged into one track without a vertex in the target region. By this approach, fake vertices are removed from the sample and the target peak at $z \approx -73$ cm becomes narrower. Usually tracks are not bridged over the target, because a strict definition of the term interaction from the point of view of a general purpose program like CORAL is hard to make [8]. The final decision is therefore passed on to user. On the other hand, bridging over the target also allows to reconstruct interaction points outside of the target area, i.e. in a silicon detector downstream of the target, allowing a clearer separation of interactions inside the target from background. For the Primakoff analysis it was decided to activate bridging over the target for data mass production.

The fit shown in Fig. 4.3(b) is a combination of two Gaussians and a quadratic polynomial for the background. The two Gaussian components can be roughly identified by small and large angle scattering. For a pure single Gaussian distribution a smaller binning to eliminate acceptance effects would be needed. In principle the used approach is a binning of the different angular components using two bins and therefore only an approximation, which however works reasonably. The Gaussians are defined in a way, that the area under the function is given by the first fit parameter. The pure number of vertices in the target peak however is not a good number to compare, since because of the bridging option removes fake vertices, the area will decrease. It was later shown by [60] on the three charged pion physics channel, that a small fraction of physics events are lost, but can be recovered using ROOT geometry instead of material maps to account for the material budget of the spectrometer. The offset between the two components shrinks down from 6.5 mm to 0.3 mm and the weighted width neglecting the offset of both components, i.e. the vertex resolution in z direction, is reduced by 43%. Additionally the artifacts vanished, the remaining peaks are identified in Fig. 4.4(a). In the projection even the two silicon wafers of each SI04 and SI05 are separated visibly into two peaks around $z=-11$ cm and $z=23$ cm respectively. The peaks at $z=-15$ cm and $z=27$ cm are representing the beam windows of the conical cryostat housing the silicon vertex detectors.

Figure 4.4 shows a comparison between T38 and the new test production where the scattering angle is plotted versus the z position of the vertex. The main vertical bands are labeled in both figures. In T38 the overall picture is dominated by the horizontal band below 0.5 mrad where more or less all z positions are equally likely. Also for example for SI04 a dependence of the reconstructed z position on the scattering angle is visible. For lower scattering angles, the z position of SI04 gradually shifts to higher z values in the reconstruction, which is unphysical. This behavior was cured, the peaks are much narrower and the background was clearly reduced. The vertex resolution depends on the scattering angle as one would expect, a clear target peak can be observed for scattering angles larger than 0.6 mrad, while for smaller angles the resolution deteriorates abruptly. The dip in the main target band at 1 mrad clearly shows that the scattering angles are not uniformly distributed. The three components multiple scattering, coulomb scattering and nuclear scattering produce a minimum at roughly 1 mrad [38].

The movement of the silicon detectors is due to thermal expansion of the support structures and therefore expected to correlate with the temperature inside the experimental hall. The run-by-run alignment determines shifts for all silicon planes in relation to one alignment file, on which the whole run-by-run alignment is based. Using the run number and the COMPASS logbook, a time value for each shift can be obtained. Figure 4.5 shows the movement of all U-planes of the silicon detectors over the time for the complete Primakoff period. The time is calculated as the time difference of the start of the particular run and the first run in the Primakoff period. In addition, the tempera-

ture trend is shown, which is recorded by the COMPASS DCS⁸. A clear correlation is seen, which strongly supports the assumption, that the detector movements are caused by thermal expansion. It shall be stressed, that due to inelastic components in the thermal expansion a total agreement of the curves is not expected. Between $t=150$ h and $t=200$ h the offsets are systematically higher. These runs are the ones using a muon beam. For several muon runs the residual distributions were checked without showing any suspicious characteristics. The different phase space of hadron and muon beam results in a different weighting of the tracking detectors and therefore in a slightly different positioning of the silicon detectors with respect to the rest of the spectrometer. Figure 4.6 shows the vertex resolution for the main Ni target versus the scattering angle of the single outgoing particle. The horizontal lines indicate the acceptance of the tracking detectors between the target and SM1, covering the respective angular acceptance. The PixelGEM detector employs two kinds of readouts as introduced in Section 2.3.2. The inner part GP01P is readout via pixels, while for the outer part GP01XY a conventional strip readout was chosen. The ordinate of the lines is sorted according to the detector appearance in the direction of the beam. To calculate the vertex resolution in z , Fig. 4.4(a) was divided into several components for different scattering angles θ in steps of $\Delta\theta=1$ mrad and the target peak was again fitted using two Gaussians and a quadratic polynomial for the background. The shape could be reproduced very well, i.e. $\chi^2/Ndf < 2$ for all fits. The combined width of both components was calculated according to:

$$\sigma = \frac{A_1 \cdot \sigma_1 + A_2 \cdot \sigma_2}{A_1 + A_2} \quad (4.5)$$

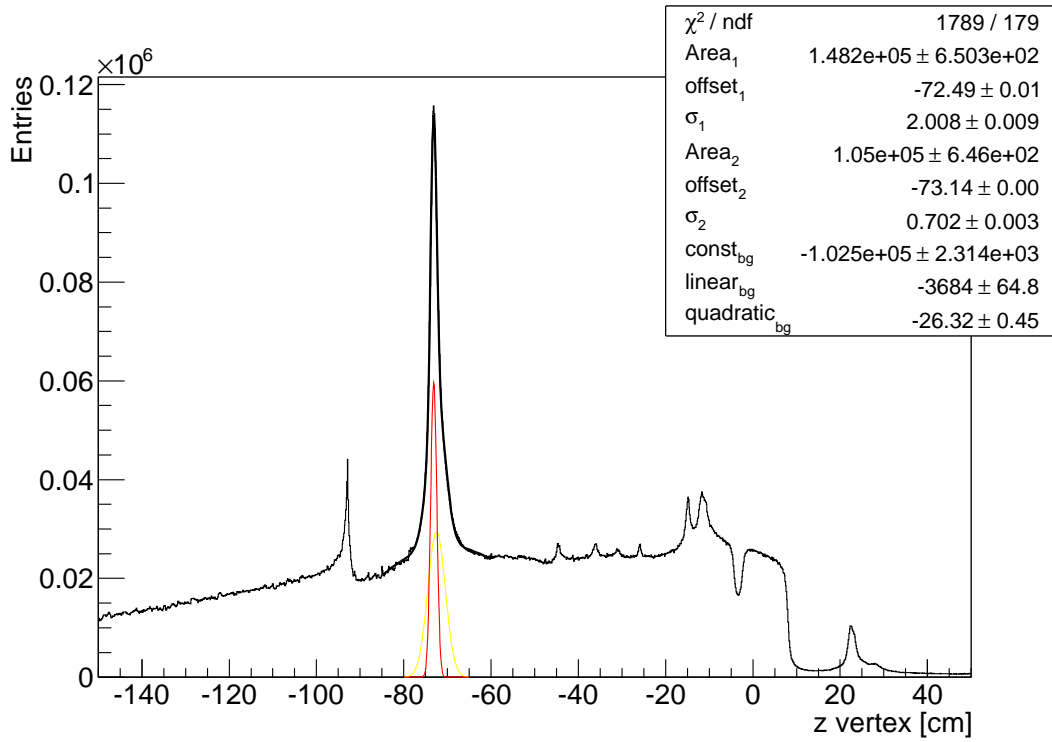
Here A_1 and A_2 denote the area under the curves, i.e. the integral. This makes Eq. 4.5 the average weighted with the integral of the Gaussian. Starting from smallest scattering angles, the vertex resolution improves drastically due to simple geometrical reasons. The first point corresponds to the angular range $\theta < 1$ mrad where the vertex resolution is low due to geometrical reasons. The vertex resolution has local minimum at $\theta_{min}=10.4$ mrad and $\sigma_{z,min}=0.66$ cm, which was obtained by fitting a quadratic polynomial around the minimum⁹. For higher scattering angles the resolution gradually degrades. A possible explanation is that for larger angles the charge cloud within the MMs is widened, which reduces the spatial resolution. Outside the acceptance of GP01XY, the absence of this major detector even accelerates this trend. Further studies are needed for clarification.

⁸Detector Control System

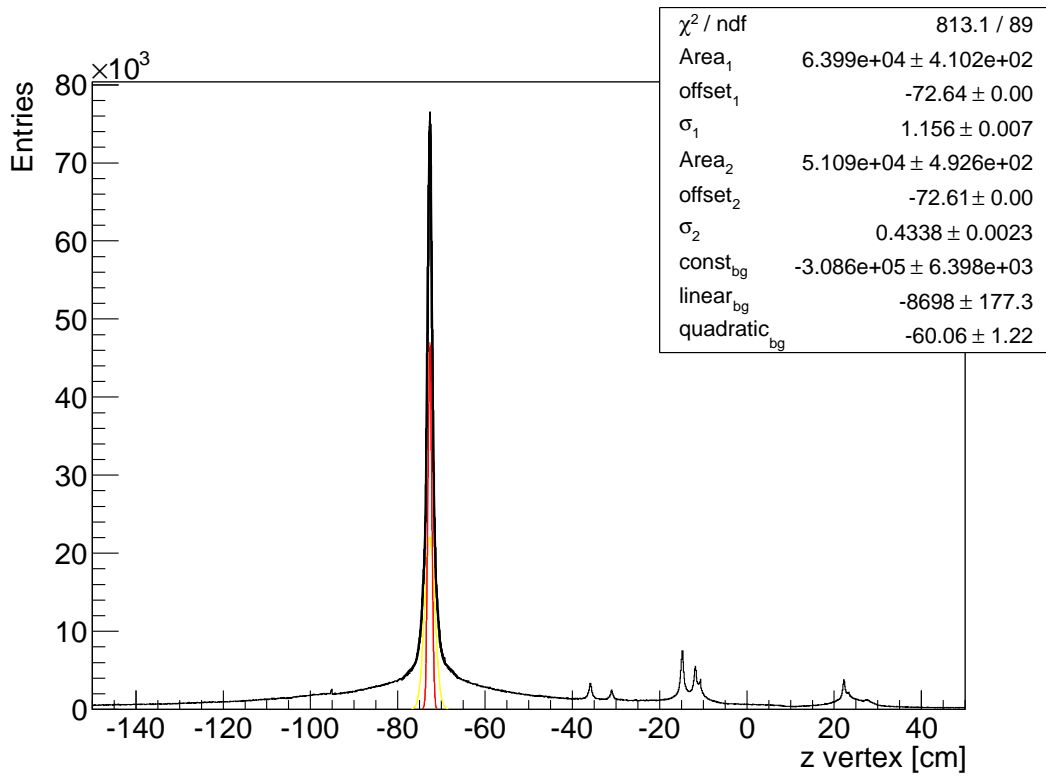
⁹Every function is a quadratic polynomial in leading order around an extremum.

4.5 Conclusion and Outlook

The need for a run-by-run alignment for the Primakoff measurement was shown. This is an important lesson learned especially with a view to the forthcoming high statistics Primakoff run in 2012 at COMPASS. This is the only way to make full use of the silicon detectors potential. However, also the relative alignment between the silicon detectors and the other tracking detectors upstream of SM1 has to be done with great care. The run-by-run alignment is now gradually done for many other hadron physics periods in 2008 and 2009, enhancing the spectrometer performance.

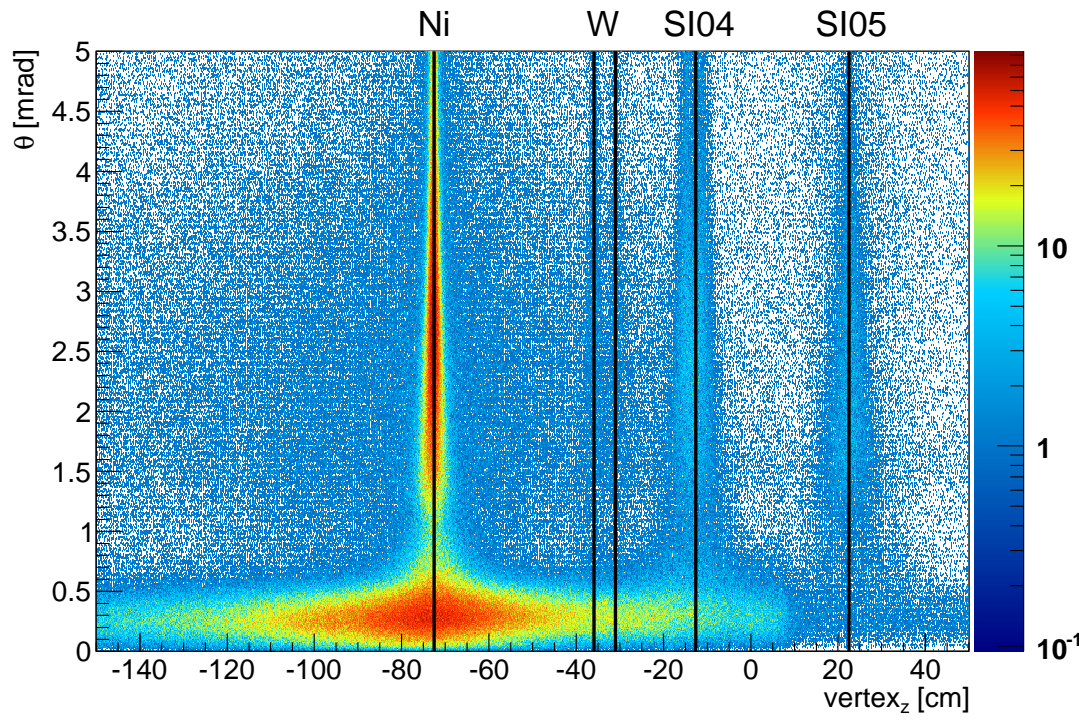


(a) T38



(b) Test production

Figure 4.3: Distribution of vertices along the z axis for run 81819. Fig. 4.3(a) shows the initial situation. The data shown in Fig. 4.3(b) include the alignment improvements as well as bridging over the target.



(a) Test production with activated bridging over the target.

Figure 4.4: The scattering angle versus the vertex position along the z axis is shown. For the old T38 production the broad background band dominates the picture and several tracking artifacts can be seen. These vanish in the new production and a clear correlation between scattering angle and vertex resolution is present.

Figure 4.5: Determined shifts of all silicon U-planes for the complete Primakoff period compared to the temperature trend inside the experimental hall. The zero point for the calculation of the time values is set to the first run of the Primakoff period.

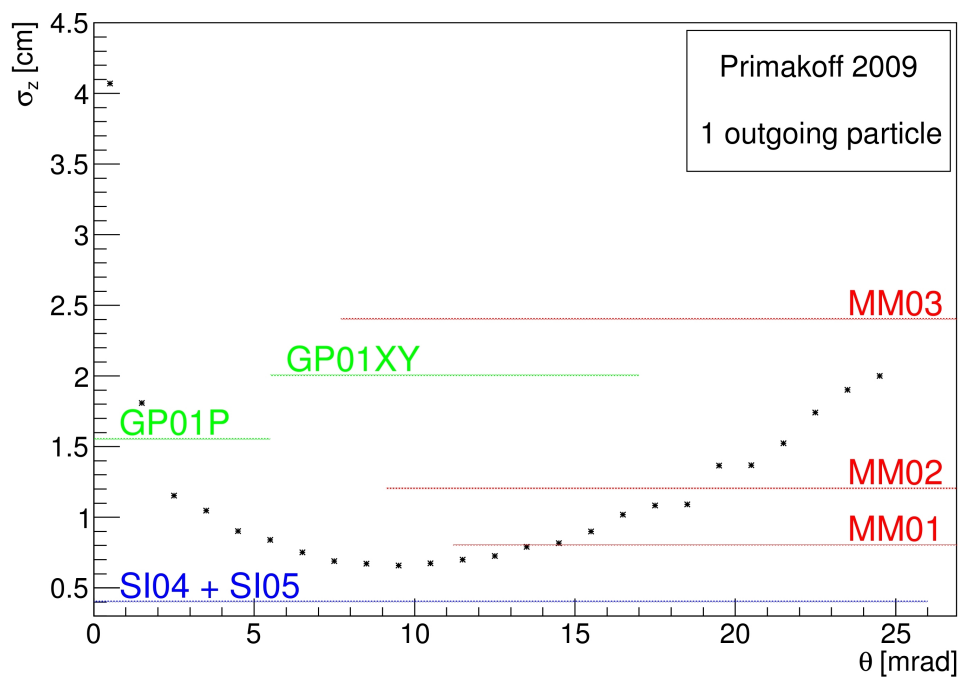


Figure 4.6: Vertex resolution of the Ni target along the z axis versus the scattering angle for one outgoing particle. The horizontal lines mark the acceptance region of the involved detectors between target and SM1, their ordinate is sorted according to the appearance of the detectors as in the direction of the beam. Shown are the two silicon stations inside the conical cryostat SI04 and SI05, the pixel and strip part of the first PixelGEM detector GP01P and GP01XY, as well as the three Micromegas stations MM01, MM02 and MM03.

Chapter 5

Performance of the Silicon Microstrip Detector for COMPASS

In this chapter, studies of the performance of the COMPASS silicon microstrip detectors are presented. Beginning with the signal amplitude, followed by the spatial and time resolution abilities and the detection efficiency, a complete overview of the COMPASS silicon detector characteristics is given. Since prior results [61] were based on a preliminary alignment, a first real insight into the performance of the detectors in cryogenic operation is given. The analysis was done during nominal physics beam condition for the Primakoff data taking period in 2009. In addition a short comparison between the performance in cryogenic and non-cryogenic operation is presented. The last section sums up the obtained results in a table.

5.1 Signal Amplitude

The signal amplitude is directly related to the deposited energy. Energy deposition is a statistical process with the total amount of energy distributed according to the Landau distribution, as introduced in Section 3.2.1. In addition, other effects come into play: The charge collection efficiency (CCE) determines the fractional charge that is actually collected at the readout strips. Radiation damage can permanently lower the CCE. The wafers are damaged by non-ionizing energy loss, which creates defects in the lattice acting as charge traps inside the silicon. Typical release times of these traps are much longer than the signal times, i.e. the trapped charge is lost for readout. In addition, there is always a certain amount of noise within each signal. This is taken into account using the pedestal measurements. Average values lie between one and two ADC channels for a single strip. The distribution of the *cluster amplitude*, which is the sum of the samples a_2 (as introduced in Section 3.6.1) of a cluster, is shown in Fig. 5.1 together with corresponding distribution for single-strip and double-strip clusters respectively. To obtain a clean sample of signal amplitudes, only clusters ascribed to a reconstructed track were used. This suppresses the low-amplitude tail coming from noise. The overall distribution was fitted with a convolution of a Gaussian and a Landau distribution, the former accounting for the binding energies of the atomic electrons [39]. The implementation of this function is provided by [17]. It can be parametrized using the Landau width, the most probable value (MPV), the area covered

by the distribution and the σ of the Gaussian component, where the latter lies between 6 and 8 ADC channels. As [11] had shown, the width of an energy loss distribution for thin silicon absorbers is significantly wider than the Landau width. In this application the convoluted Gaussian can be partially regarded as a phenomenological approach, also taking into account the electronics noise. Further an additional broadening of the distribution is introduced, because the recorded sample a_2 does usually not coincide with the signal maximum, as the APV samples are spaced in time by the TCS period of 25.8 ns, see Section 3.5. The maximum of the signal is related to a_2 via the TCS phase as introduced in Section 3.6 and the theoretical signal shape given in [24]. Corrections of up to 20% to the individual samples are expected which will narrow the distribution shown in Fig. 5.1. The most probable value can be used to fix the scale of the measured cluster amplitudes. A MIP creates roughly 30000 free charge carriers in a 280 μm thick silicon layer [54]. Altogether the function describes the data better than a pure Landau distribution. However, deviations from the data are observed for high cluster amplitudes. Starting from roughly 70 up to 150 ADC channels the data lie slightly above the fit, whereas for cluster amplitudes higher than 150 ADC channels, it is the other way around. This suggests that the highest cluster amplitudes are shifted downwards, which can be explained by some fraction of the total deposited energy escaping the active volume. This is in agreement with the expectation, as this is not foreseen in the applied theory. Furthermore the cluster amplitude distribution for single-strip and double-strip clusters is depicted separately. For double-strip clusters, the high amplitude tail is far more pronounced. The spread of the charge cloud depends on the deposited energy, as the total number of created charge carriers in the active volume is only subject to small relative fluctuations. Moreover both distributions differ largely in their width and MPV, which is attributed to the non-linearity of the charge sharing.

5.2 Spatial Resolution

5.2.1 Method

For analysing the spatial resolution of the COMPASS silicon detectors, 2009 Primakoff data (see App. A) were chosen. Five complete stations of silicon detectors were operated stably at 200 K. On special request, during the physics data production also the silicon clusters were written to the output. This way during the analysis the cluster information, i.e. the time and the position of all silicon clusters are available, which permits the use of the Kalman filter lately implemented in PHAST (see Section 2.4.2). On this level also cuts on the track quality could be applied. In the final track selection several criteria were requested. For one thing the measured track momentum needs to be above 10 GeV/ c . Tracks with a lower momentum were cut out, because they are more prone to multiple scattering than their high-momentum counterparts. This way only beam tracks and tracks which were bridged through SM1 are taken into account. Furthermore the time of the track, calculated according to Eq. 5.6 in CORAL from all clusters contributing to the track, with respect to the trigger time needs to be smaller

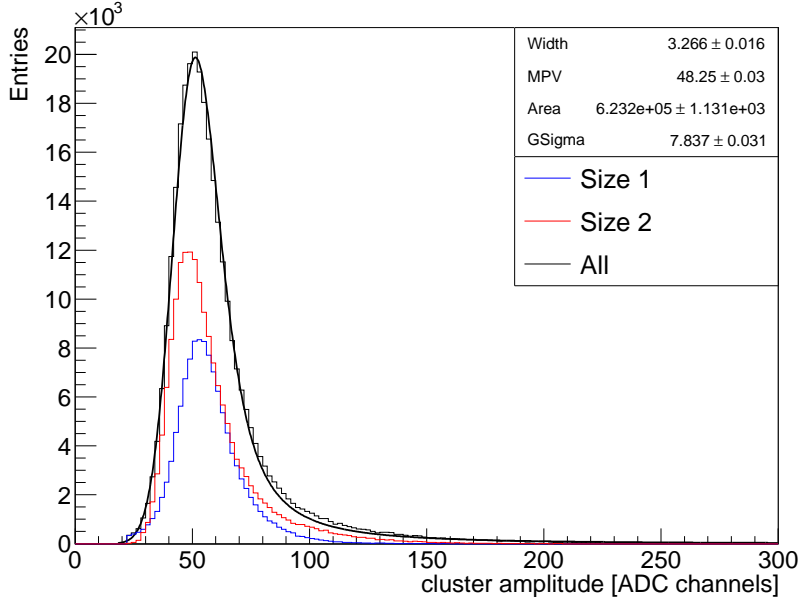


Figure 5.1: Signal amplitude of clusters assigned to tracks for SI02V. The fit shown is a convolution of a Gaussian and a Landau distribution [39].

than 5 ns. The SciFis clearly dominate this weighted mean with a time resolution of 400 ps, compared to which the bias introduced by one silicon plane is negligible. For the left-out "off-time" tracks a reliable readout of all involved silicon detectors is not guaranteed, since the signal height is exponentially decreasing. The analysis was done solely using the silicon detectors, requiring a cluster attributed to the track either in all planes upstream or downstream of the target. For each track passing the track selection step, the track was refitted using 18 silicon planes¹ *active*, and keeping the plane under examination *passive*. This way an *unbiased* evaluation of the detector performance is ensured. After refitting the track, the smoothed track parameters as introduced in Section 2.4.1 at the z coordinate of the detector plane are obtained and transformed into the WRS (see Section 4.1.1). Then the distance of track to the nearest hit in the detector plane can be easily calculated. Even though at this time the track position at the plane is very precisely known, its error still influences the overall width of the residual distribution $\sigma_{residual}$. To minimize this influence, the track was required to have an assigned double-strip cluster in the closest silicon plane measuring the same coordinate. Because the uncertainty of the track position σ_{track} and of the *intrinsic detector resolution* $\sigma_{intrinsic}$ are independent, both contributions add up quadratically:

$$\sigma_{residual}^2 = \sigma_{intrinsic}^2 + \sigma_{track}^2. \quad (5.1)$$

¹20 SI planes in total, SI02X inoperable

5.2.2 Fitfunction for Single-strip Clusters

Exemplary the unbiased residual distribution of SI04X is shown in Fig. 5.2, only taking into account clusters with exactly one strip. With exclusively single-strip clusters, one would expect as spatial resolution $\text{RMS}=\text{pitch}/\sqrt{12}$. This can be easily derived by calculating the standard deviation of a rectangular function with the length of one pitch. For the COMPASS silicon detectors this would be roughly $15\ \mu\text{m}$, but in the data all detectors show a better spatial resolution. The fact that actually a cluster composed of only one strip is *observed* includes already additional information about the position of the track, see Fig. 7.1. For the region in the middle between two strips the probability to end up with a single-strip cluster is smaller than 10%. This can be viewed as an effective pitch reduction for single-strip clusters. Nevertheless the distribution is not Gaussian, but flattened at the top. The result can be described by one step function convoluted with a Gaussian for each side like given in Eq. 5.2. This function has no analytical form but is commonly known as the *error function*, denoted by $\text{Erf}(x)$ in the following. It is implemented within the ROOT framework.

$$f(x) = c \cdot \text{Erf}\left(\frac{\mu_1 - x}{\sigma_1}\right) + c \cdot \text{Erf}\left(\frac{x - \mu_2}{\sigma_2}\right) \quad (5.2)$$

The standard deviation σ of 5.2 not only depends on σ_1 and σ_2 but also on μ_1 and μ_2 , because these quantities define a relative offset between the two components. Generally the standard deviation of an arbitrary probability distribution can be calculated by [53]:

$$\sigma = \sqrt{\text{E}[x^2] - \text{E}[x]^2} \quad (5.3)$$

with $\text{E}[a]$ denoting the expectation value of a . The Integrals for this particular case have been performed using the Mathematica Online Integrator [48].

$$\text{E}[x^2] = \frac{c}{2} (\sigma_1^2 - \sigma_2^2 + 2\mu_1^2 - 2\mu_2^2) \quad (5.4)$$

$$\text{E}[x]^2 = \frac{c}{3} (2\mu_1^3 - 2\mu_2^3 + 3\mu_1\sigma_1^2 - 3\mu_2\sigma_2^2) \quad (5.5)$$

The normalization integral was calculated to be $2c(\mu_1 - \mu_2)$. Equation 5.2 plus a Gaussian background was applied to fit the residual distribution shown in Fig. 5.2. With the obtained fit parameters the standard deviation of Fig. 5.2 is calculated to be $\sigma=6.4\ \mu\text{m}$. The “effective” pitch is therefore roughly $22\ \mu\text{m}$ which is less than half of the design value.

5.2.3 Results

With the track sample described in Section 5.2.1 the spatial resolution of the COMPASS silicon detectors could be determined. All findings are for planes which were passive during the fitting process, therefore not biasing the results. A distribution of the distance of the cluster position from the track is shown in Fig. 5.3, where besides

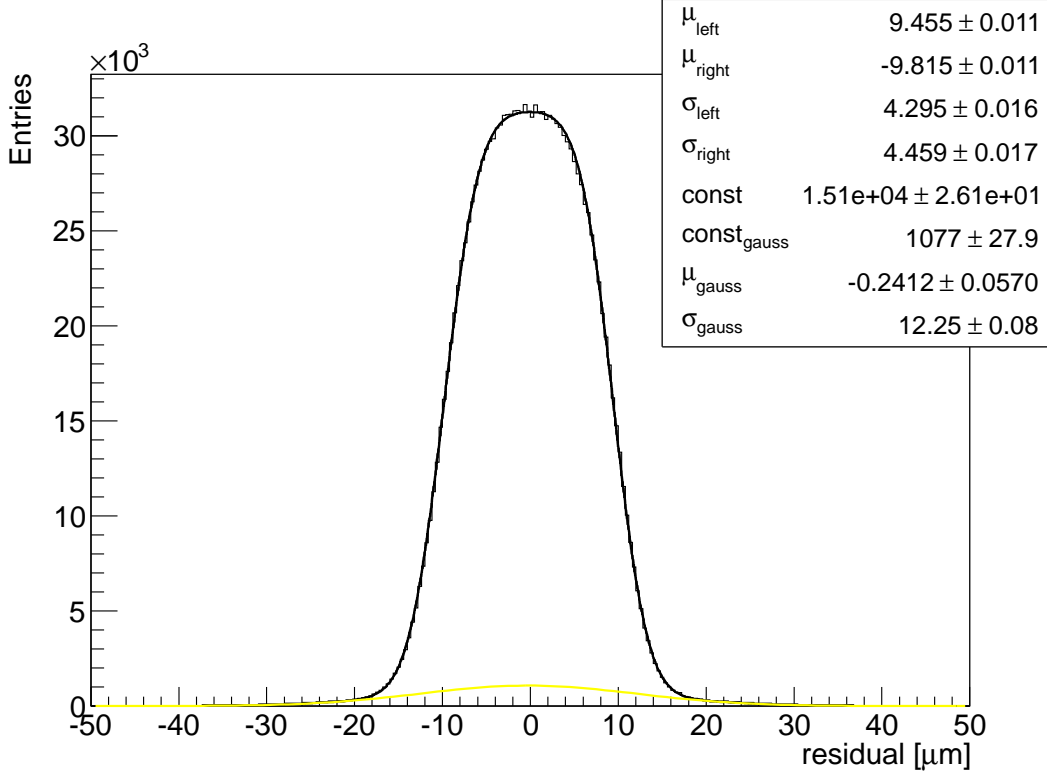


Figure 5.2: Residual of SI04X for single-strip clusters. Fitted with Eq. 5.2 plus a Gaussian background (yellow). The standard deviation is calculated to be $6.4 \mu\text{m}$.

the total distribution also the subsamples of one-strip and double-strip clusters are depicted. The first was fitted using Eq. 5.2 plus a Gaussian background and the latter with a combination of two Gaussian functions with a coinciding mean value. Clusters composed of three or more strips are not shown separately, but included in the overall distribution. All quoted resolutions are obtained from the RMS of the corresponding residual distribution in the range $\pm 50 \mu\text{m}$, unless stated otherwise. The width of the residual distribution for single-strip clusters is more than 40% wider than the corresponding distribution for double-strip clusters. For the latter, the position is refined according to Eq. 3.17 which gives a large enhancement in precision. A larger fraction of two-strip clusters therefore improves the performance of the plane drastically. This fraction in turn, depends mainly on the wafer design, because intermediate strips on a sensor increase the charge sharing and therefore the fraction of double-strip clusters. All Y and V planes have intermediate strips, while among the X and U planes, only the detectors in SI02, SI04 and SI05 have intermediate strips [61]. The difference in the wafer design was illustrated in Section 3.3.1. For this reason, the percentage of two-strip clusters varies from 33% up to 67%. The average fraction among all planes with

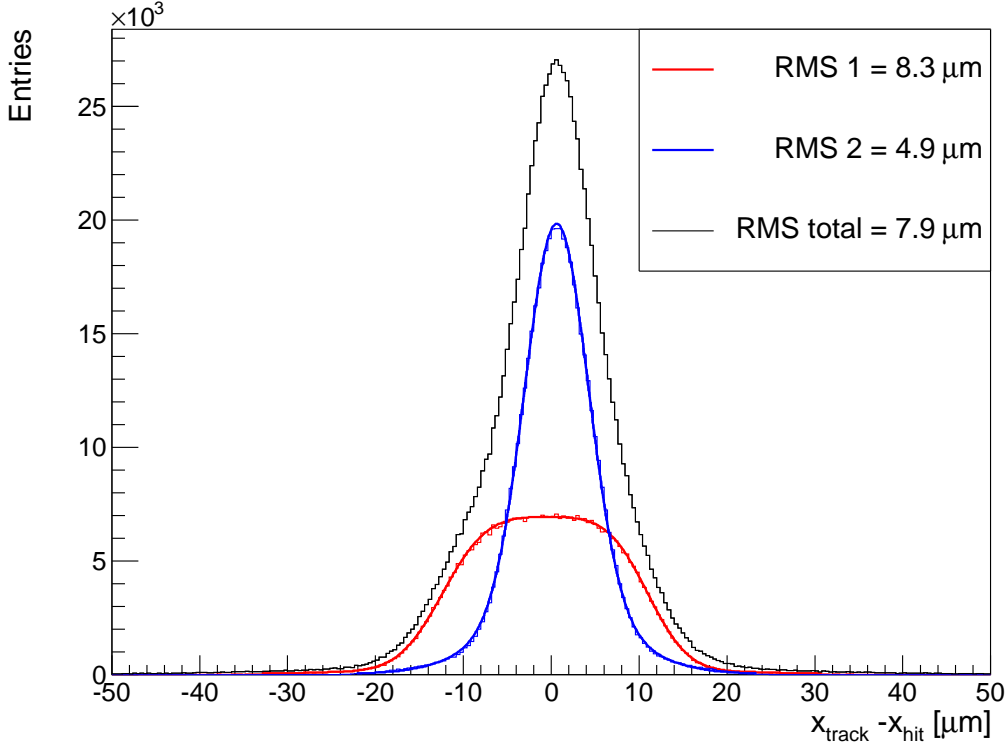


Figure 5.3: Residual distribution for SI01Y in muon beam.

intermediate strips is 57% and 35% for planes without intermediate strips respectively. This directly shows up again in the average intrinsic spatial resolution, which is $6.8 \mu\text{m}$ and $8.5 \mu\text{m}$ for planes with and without intermediate strips respectively. The smallest obtained value for the intrinsic spatial resolution is $5.0 \mu\text{m}$ for all clusters and all planes perform better than $10 \mu\text{m}$. For two-strip clusters the best spatial resolution is found to be $3.3 \mu\text{m}$.

Clusters composed of three or more strips significantly contribute to the RMS of the total residual distribution. An extension of the clustering algorithm used for the results presented in this chapter, that is treating all clusters larger than two strips and significantly improving the performance for these cases is presented in Chapter 6.

5.3 Time Resolution

Figure 5.4 shows the signal time distribution for a typical silicon plane (here SI01X) in standard muon beam conditions for 2009 Primakoff data (run 81974). The cluster times and the errors are extracted from the raw data according to the algorithm described in Section 3.6.1. The figure shows the contributions from single- and double-strip clusters separately since they were shown to have a relative offset in time [24]. This offsets

5.3 Time Resolution

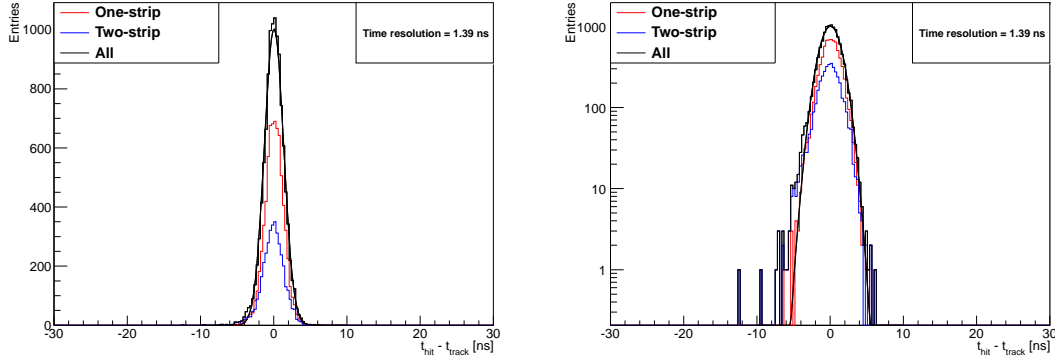


Figure 5.4: Timing distribution of SI01X fitted with a Gaussian. The obtained σ is 1.32 ns. The time resolution stated is the RMS of the distribution shown in the histogram, with clusters outside this range being discarded. Unfolding the track time error of 0.375 ps, the intrinsic time resolution of 1.34 ns is calculated. Since the track time is dominated by the contribution of the two SciFi planes, the bias can be neglected. The right side shows the identical distribution but in logarithmic scale.

were first taken into account in the time calibration by [61] and during this work new time calibrations for the Primakoff period were created and used for this analysis. The time resolution given is the RMS of the shown histogram, where clusters outside the shown range are discarded. This distribution was obtained with the same tracks used in Section 5.2.1. In addition the track time was required to be within 2 ns of the trigger time. Furthermore, only hits within an time window of $5\sigma_t$ around the track time were considered, a condition which is fulfilled for more than 99.6% for all planes. The track time is calculated within CORAL as the weighted mean of all cluster times belonging to the track.

$$t_{track} = \frac{\sum_{i=1}^n \frac{t_{cl,i}}{\sigma_{cl,i}^2}}{\sum_{i=1}^n \frac{1}{\sigma_{cl,i}^2}} \quad (5.6)$$

This way also the track time error σ_{track} can be calculated (roughly 0.3 ns) and deconvolved to obtain the intrinsic timing resolution of each detector plane. In all timing distributions, one finds a dominant Gaussian component with some non-Gaussian outliers, which are supposed to stem from particular noisy channels or pile-up tracks. During high intensity beams, i.e. standard run conditions, the tails of signals can still be present when the next signal already arrives, therefore distorting the amplitude measurement which leads to a falsified signal time. In addition to the RMS of the distribution, also a Gaussian fit was performed, both shown in Table 5.1. The Gaussian width can be up to 15% smaller than the RMS in extreme cases, as the RMS is

Table 5.1: Time resolution for all silicon planes. Clusters outside the range of ± 30 ns were discarded for the calculation of the RMS. Additionally the σ of a performed Gaussian fit is given. All readings are in ns.

Detector	SI01U	SI01V	SI01X	SI01Y	SI02U	SI02V	SI02X	SI02Y
σ_t	1.35	1.56	1.27	1.49	1.78	1.78	—	1.84
RMS	1.44	1.71	1.34	1.61	1.84	1.93	—	2.00
Detector	SI03U	SI03V	SI03X	SI03Y	SI04U	SI04V	SI04X	SI04Y
σ_t	1.22	1.89	1.57	1.69	1.75	1.79	1.59	1.76
RMS	1.34	2.11	1.88	1.79	1.96	2.11	1.75	2.01
Detector	SI05U	SI05V	SI05X	SI05Y				
σ_t	1.64	2.13	1.81	1.93				
RMS	1.77	2.33	1.92	2.15				

sensitive to non-Gaussian outliers. The average intrinsic RMS $\langle \text{RMS}_i \rangle$, i.e. with the track time error unfolded, is 1.84 ns, while the corresponding average Gaussian sigma $\langle \sigma_i \rangle$ is 1.68 ns. The highest obtained value for the time resolution is a RMS of 1.34 ns and a Gaussian σ of 1.22 ns. All planes are better than 2.5 ns (RMS) for both muon and hadron beam. The average performance in hadron beam is within 2% of the values observed with muon beam. This is because the muon beam used during the Primakoff period has only a factor of 1.3 higher beam intensity. Partly because the signal decay time decreased from 127 ns in non-cryogenic operation to 74 ns in cryogenic operation [61], this does not result in significantly more pile-up. The time information of one sensor, i.e. two projections can be combined into one common time value. In this context the amplitude correlation can be exploited to effectively suppress noise or clusters affected by pile up. First of all, the fitted Gaussian sigmas of the two projections on one detector module were combined into one common time resolution for the two projections according to

$$\frac{1}{\sigma_{AB}^2} = \frac{1}{\sigma_A^2} + \frac{1}{\sigma_B^2} \quad (AB) \in \{(UV), (XY)\}. \quad (5.7)$$

Secondly, the time information of two clusters was combined using Eq. 3.14 and then the distribution around the track time was examined. The results obtained with both methods are summarized in Table 5.2. For the wafer SI01XY, the combined time resolution obtained from one fit is $\sigma=1.08$ ns. One should note, that the track time uncertainty was not deconvolved in this case. The results from both methods agree within 5%. A timing at this level of precision could offer interesting capabilities as outlined in Section 6.5.

Table 5.2: Combined time resolution for all silicon sensors. Clusters outside the range of ± 30 ns were discarded.

Wafer	SI01UV	SI02UV	SI03UV	SI04UV	SI05UV
σ_t [ns]	1.11	1.39	1.14	1.36	1.46
RMS [ns]	1.36	1.56	1.42	1.78	1.80
Wafer	SI01XY	SI02XY	SI03XY	SI04XY	SI05XY
σ_t [ns]	1.08	—	1.26	1.28	1.45
RMS [ns]	1.29	—	1.57	1.70	1.77

5.4 Efficiency

The *total efficiency* of a detector is defined as the total number of events registered in the detector divided by the total number of events emitted by an arbitrary source [45]. The total efficiency is composed of two factors, namely the *geometrical* efficiency or *acceptance* and the *intrinsic* detection efficiency. Since the geometrical efficiency is given by the active area of the detector and the distance from the target, this work will concentrate on the determination of the intrinsic detection efficiency. The intrinsic efficiency is defined as the ratio of *signals observed* in a plane over the total number of *signals expected* in the plane. By the restriction to expected tracks, the geometrical contribution is removed. A signal is expected when the detectors upstream and downstream of the plane under consideration have measured the track and the extrapolation between the measured points crosses the active area of the detector plane. For the decision, whether a track is seen in a plane, its impact point on the plane is calculated. The track is accepted if a cluster within a certain route width around this impact point is found. In addition, a cut on the time difference between the cluster time and the track time can be applied. Inside this work, the same options as used during the CORAL prepattern were chosen for the evaluation. This means $\pm 3\sigma_{res}$ in space and a rather large value of $\pm 16\sigma_t$ in time. Technically the efficiency plots shown in Fig. 5.5 were created filling two identically binned two dimensional histograms. One was filled every time a track crossing the plane was found, the other one only if in addition also a cluster fulfilling the cuts is present. The bin to be filled was determined by the track position at the detector plane, as provided by the tracking but with coordinates given in the MRS (see Section 4.1.1). By dividing the second histogram with the first one, the two dimensional efficiency map of the plane can be derived. The average efficiency over all silicon planes is 99.1% for muon beam and 99.3% for hadron beam. Fig. 5.5(b) shows the efficiency plot for SI04U, which is located downstream of the target. The active area is uniformly illuminated due to scattering in the target and no dead or noisy strips are present. Nevertheless the beam spot can be identified as the circular deep red shape in the middle. At the border of the active area, some points with local low efficiency down

to 90% can be seen. This can be explained by the low statistics in this region, because at the very edge tracks are not reconstructed reliably. Fig. 5.5(a) shows the same plot for SI03X, located in the beam telescope. The beam spot is much more prominent framed by a circle of points where the efficiency drops down to 97% locally, again due to the high fluctuations at smaller number of available tracks, biasing towards lower efficiencies. The low statistics can already be observed in the number of reconstructed tracks shown in Fig. 5.6. The ring shaped structures are supposed to result from the beam trigger, which was a scintillator disc and the target discs, but no studies to clarify this could be conducted.

5.5 Comparison with Non-Cryogenic Results

Cryogenic operation of the silicons was mainly intended to increase their radiation hardness, but in addition several beneficial side effects are observed. A faster signal time and lower noise level increase time and spatial resolution. As since the last analysis of the performance given in [61], quite some development was done on related topics, e.g. Chapter 4, it is hard to disentangle the different components of the observed improvements.

Unambiguously the time resolution could be improved clearly by the cryogenic operation as already observed in [61], making it beneficial to introduce the known correction for the time offset for different cluster sizes. For the comparison to be concise, the Gaussian sigma of the fit is used since this is also the method applied in [24], where the reference values of the time resolution are taken from. The result is summarized in Table 5.3. The average time resolution was improved from 3.0 ns and 2.0 ns to now 1.8 ns and 1.4 ns for planes with intermediate strips and without intermediate strips respectively.

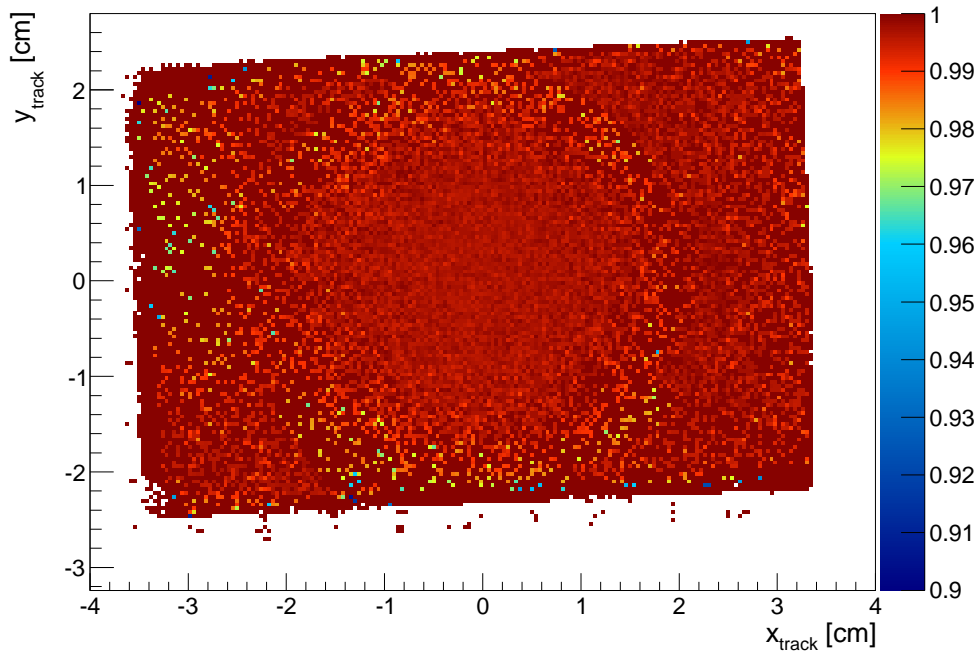
Table 5.3: Comparison of the average time resolution as obtained from a Gaussian fit in cryogenic and non-cryogenic operation. All values for non-cryogenic operation are taken from [24].

Detector type	Non-cryogenic	cryogenic
intermediate strips	3.0 ns	1.8 ns
no intermediate strips	2.0 ns	1.4 ns

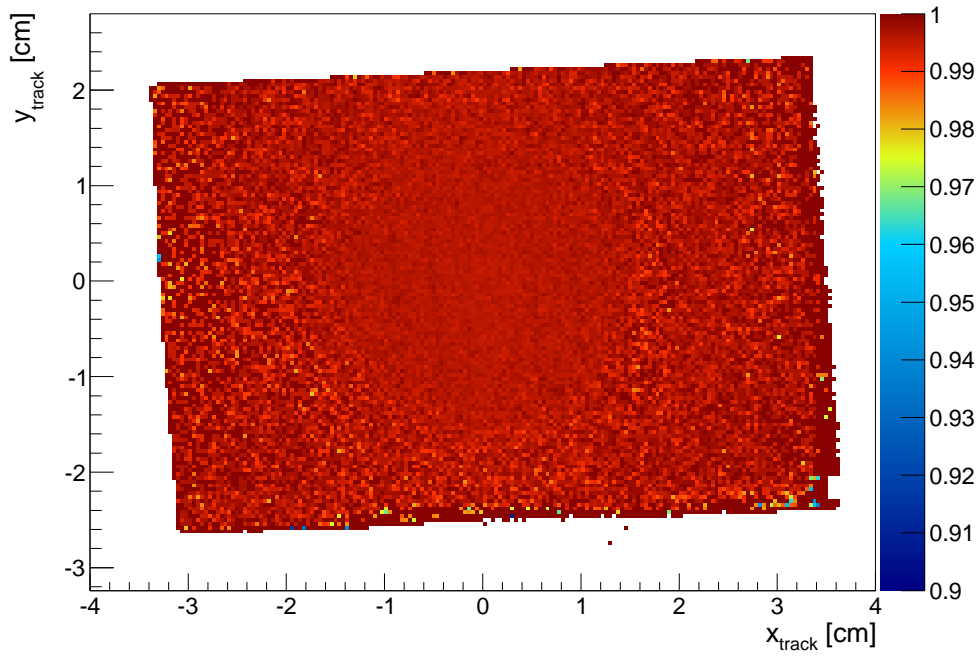
The reference values were still obtained with the systematic offset in the cluster times of different sizes. Again in [24] an improvement from 3.0 ns to 2.6 ns was estimated, which is not sufficient to explain the observed improvement. A meaningful distinction between hadron and muon beam was not attempted, since for the Primakoff measurement the beam intensities of hadron and muon beam differ only by a factor of 1.3 [46].

The spatial resolution is closely connected to the charge sharing behavior and the

5.5 Comparison with Non-Cryogenic Results



(a) SI03X



(b) SI04U

Figure 5.5: Two dimensional efficiency plot for a plane from the beam telescope (a) and downstream of the target (b).

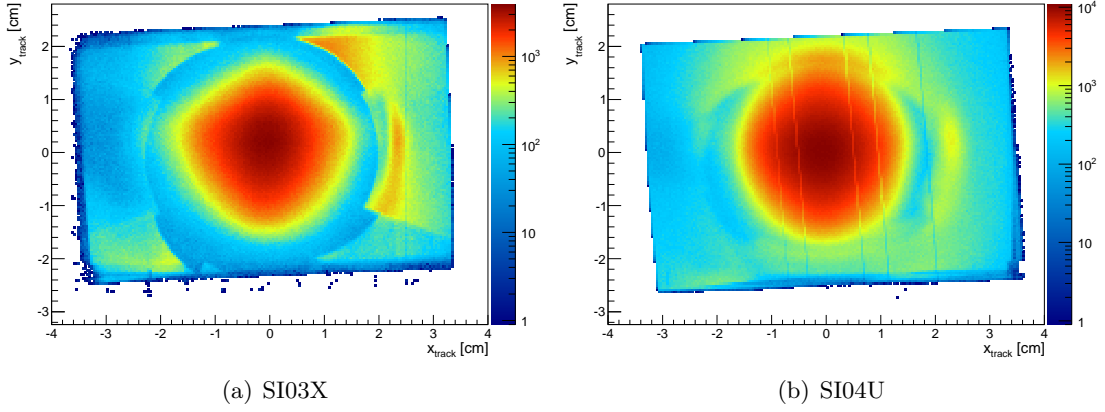


Figure 5.6: Expected tracks in SI03X (a) and SI04U (b). The ring shaped structures are supposed to result from the beam trigger and the target discs. The low statistics in some regions is also visible in the efficiency map shown in Fig. 5.5.

noise level. The cryogenic operation lowered the noise level which allowed to regain double-strip clusters at very high and low values of η , i.e. very small amplitudes on one of the two strips. In non-cryogenic operation these small signals were not distinguishable from noise and therefore suppressed. In particular, the percentage of clusters with size 2 among the total number of clusters increased from an average of 50% and 30% [2] for planes with and without intermediate strips to 57% and 34% respectively. This implies an improvement of the spatial resolution. Unfortunately, the applied alignment procedure described in [24] differs from the one described in Chapter 4 in the fact, that for the 2004 data only the detector position was adjusted, but not the pitch and the rotational angle. This might cause a non negligible contribution to the spatial resolution quoted in [2]. Overall the spatial resolution improved from an average of $8 \mu\text{m}$ and $11 \mu\text{m}$ for planes with and without intermediate strips to $6.8 \mu\text{m}$ and $8.5 \mu\text{m}$ respectively.

Table 5.4: Comparison of the average spatial resolution and the fraction of double-strip clusters in cryogenic and non-cryogenic operation [24].

Detector type	Non-cryogenic	cryogenic
intermediate strips	$8 \mu\text{m}$ 50%	$7 \mu\text{m}$ 57%
no intermediate strips	$11 \mu\text{m}$ 30%	$9 \mu\text{m}$ 34%

5.6 Summary

The results of this chapter are summarized in Table 5.6. For the spatial resolution, the RMS of the residual distribution of one-strip and two-strip clusters are given. In addition the RMS of the complete residual distribution with deconvolved track error can be found. The fifth column, shows the fraction of size two clusters compared to the total number clusters, followed by the corresponding fraction for clusters composed of three or more strips. Next the time resolution as obtained from a Gaussian fit with deconvolved track time error is shown followed by the intrinsic efficiency of the plane. In the last column, the high voltage setting during the 2009 Primakoff period is given. SI02X was rendered inoperable in an incident at the beginning of the Primakoff period, so no values are stated.

Table 5.5: Performance overview of the COMPASS silicon detectors. All RMS values are given in μm . The column ‘‘Cls 3’’ shows the fraction of clusters that are composed of three or more strips.

Plane	RMS ₁	RMS ₂	RMS _{<i>i</i>}	Cls 2 [%]	Cls 3 [%]	$\sigma_{t,i}$ [ns]	Eff [%]	HV [V]
SI01U	11.2	7.2	8.2	37.5	4.3	1.35	98.8	95
SI01V	8.4	4.9	7.6	48.9	5.8	1.56	98.9	95
SI01X	12.3	7.7	9.6	32.9	2.0	1.27	99.4	75
SI01Y	8.3	4.9	7.4	52.0	5.4	1.49	98.9	75
SI02U	7.8	5.8	7.6	58.3	6.4	1.78	99.3	135
SI02V	7.3	4.2	7.1	55.7	6.8	1.78	98.3	135
SI02X	—	—	—	—	—	—	—	—
SI02Y	6.9	4.2	7.1	54.4	9.0	1.84	98.9	130
SI03U	10.2	3.4	7.8	33.8	2.6	1.22	98.9	60
SI03V	7.7	3.6	7.0	51.8	5.1	1.89	99.2	60
SI03X	10.9	3.6	8.3	36.2	2.6	1.57	99.7	85
SI03Y	7.7	3.6	7.1	50.1	8.3	1.69	98.8	85
SI04U	7.7	3.7	6.6	64.9	9.2	1.75	99.6	115
SI04V	8.2	4.2	7.3	53.9	7.0	1.79	98.7	115
SI04X	6.8	3.7	6.4	59.3	6.5	1.59	99.4	110
SI04Y	8.0	4.1	7.1	53.9	6.4	1.76	98.7	110
SI05U	5.9	3.3	5.0	68.6	6.9	1.64	99.5	105
SI05V	7.1	4.0	6.8	55.8	8.9	2.08	99.3	105
SI05X	7.2	4.3	5.7	67.0	9.5	1.81	99.5	120
SI05Y	6.6	3.4	6.5	53.8	11.8	1.93	99.0	120

Chapter 6

Improvement of the Clustering Algorithm

This chapter starts with a discussion of the currently used Cinderella clustering, as introduced in Section 3.6.2. The results presented in the previous chapter were obtained with this algorithm. Two optimizations and the technical implementation are presented and their impact on the tracking is evaluated. Further possibilities for enhancing the clustering algorithm are given in the outlook.

6.1 Analysis of the Current Situation

In Chapter 5 it was shown, that the Cinderella clustering works successful for single-strip and double-strip clusters. A typical residual distribution for clusters that are composed of three strips, is shown in Fig. 6.1. Clearly a double peak structure is seen, which is attributed to either δ -electrons, overlapping tracks or noise contribution. The RMS of residual distributions for clusters which are composed of three or more strips is generally larger than $15 \mu\text{m}$. The fraction of such clusters varies from a few percent to up to 10% for some detectors in the conical cryostat, as shown in Table 5.6. These clusters cannot contribute to precision tracking, since their accuracy is at least a factor of two lower than needed (and in most cases also achieved). There is also the possibility, that the contribution of such clusters screws up tracks, because either their direction is distorted in a way, that bridging fails, or the track is dropped because of the increased χ^2 . Additionally the detector performance is significantly deteriorated, since the total RMS of most residual distributions is dominated by clusters composed of three or more strips.

6.2 Misidentified Double-strip Clusters

6.2.1 Approach

In the course of this analysis, it was realized that quite a large part of the double peak structure in Fig. 6.1 can be explained by a regular double-strip cluster, that picked up a third strip with an amplitude of about 10 ADC channels by mistake. Typical cluster amplitudes are around 52 ADC channels, see Section 5.1 and Fig. 5.1. For a cluster where the three strips have the amplitudes 8, 26, 26, in the following the abbreviated form (8,26,26) is used. Calculating the weighted mean according to

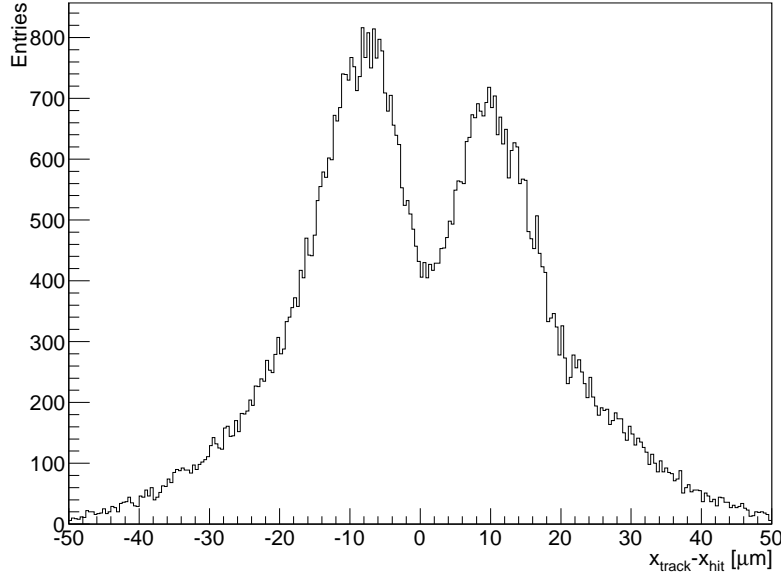


Figure 6.1: Residual distribution for SI02V restricted to clusters of three strips. The main contribution of the double peak structure is from noise. Overlapping tracks and δ -electrons account for roughly 30%. The RMS of the shown distribution is $16\mu\text{m}$, while the peaks at about $\pm 10\mu\text{m}$ have a Gaussian σ of roughly $7\mu\text{m}$.

Eq. 3.17 for a (8,26,26) and a (26,26) cluster respectively, yields a spatial difference of $0.2 \cdot \text{pitch} \approx 11\mu\text{m}$. This is in good agreement with the peak positions seen in Fig. 6.1. Such pickup of noise is unavoidable, since the clustering algorithm is very sensitive to the parameter introduced in Eq. 3.16. A stricter cut, i.e. lowering Y_{cutoff} means, that adjacent strips are cut more often, because the time coincidence criterion is harder to fulfill. For small amplitudes the relative uncertainties are large, as are the resulting errors on the time measurement, making a time cut inefficient. Therefore by tightening the cut one runs the risk of splitting regular two-strip clusters. This situation is shown in Fig. 6.2. For this distribution $Y_{\text{cutoff}}^* = 3.5$ was used within the Cinderella clustering instead of the usual value for cryogenically operated detectors $Y_{\text{cutoff}} = 20$. Clearly the sharp drops at $\pm \text{pitch}/2 \approx 27\mu\text{m}$ can be seen, which are a result from actual two-strip clusters that were split into two one-strip clusters by the Cinderella clustering algorithm. The width of the distribution is not meaningful, as the data were extracted from a preliminary alignment and using an enlarged silicon route width (Section 4.3.1).

This motivated the introduction of an additional step in the clustering algorithm: All clusters composed of three strips are checked whether they contain a strip at the border with the sample a_2 being smaller than 15 ADC channels. These strips are then removed from the clusters. This procedure was further extended to four-strip clusters. Again the resulting cluster is required to have size two, and the signature allows two

Figure 6.2: Residual distribution for SI05V restricted to single-strip clusters, illustrating a too strict cut on Eq. 3.16 in the Cinderella clustering, namely $Y_{\text{cutoff}}=3.5$. Clearly the sharp drops at $\pm\text{pitch}/2 \approx 27 \mu\text{m}$ can be seen, which result from actual two-strip clusters that were split into two one-strip clusters.

strips with small amplitudes on one side e.g. (8,10,48,24) or one on both sides e.g. (8,58,32,14) of the cluster.

Table 6.1: Summary of the properties of the clustering improvement described in this section.

Naming	Input size	Created clusters	Output size
Misidentified double-strip clusters	3, 4	1	2

6.2.2 Performance

The above described approach was integrated into the existing clustering algorithm in CORAL. In order to study the impact of this modification, CORAL was modified in a first run to tag all candidates for modification, i.e. clusters composed of three or four strips and the explained structure. In a second run the cutting was conducted and the resulting double-strip clusters were again tagged. CORAL was run twice on exactly the same raw data (given in Table A.2) changing no other option. For the tagged clusters, the spatial resolution was determined from the RMS of the unbiased residual distribution as shown in Fig. 6.3. In the shown example of SI03U, the RMS was reduced by almost a factor of 3 from $21.7 \mu\text{m}$ to $7.8 \mu\text{m}$ and at the same time the integrated number of clusters within a window of $\pm 25 \mu\text{m}$ increased by 40%. Table 6.2 summarizes the performance of the new algorithm in comparison to the old one. The last column gives the percentage of clusters that show the required structure with respect to the total number of clusters composed of three and four strips. While this fraction is roughly at 70% for all planes, the absolute number varies by a factor of ten. The latter was estimated by integrating the residual distribution in the interval $\pm 25 \mu\text{m}$. The largest number of clusters created by the new algorithm is observed at the detectors inside the conical cryostat, i.e. the stations SI04 and SI05, which were equipped with a capacitor configuration, that increased the noise¹. Additionally the cooling in SI05 was not as stable as in the other silicon stations, causing temperature fluctuations of several Kelvin, that in turn lead to more noise. Intermediate strips influence the total number of modified clusters, as can be seen in SI01 and SI03, where in both cases the U and X plane have no intermediate strips and the lowest absolute number of modified

¹This is intended to be changed in the future.

clusters among all planes, while in the V and Y planes a significantly larger number was observed.

Table 6.2: Improvement for three- and four-strip clusters due to the changed clustering algorithm described in Section 6.2. The last column gives the fraction of modified clusters with respect to the total number of clusters composed of three or four strips.

Detector	RMS _{old} [μm]	RMS _{new} [μm]	Int _{old} [-25;25]	Int _{new} [-25;25]	Fraction [%]
SI01U	24.0	15.1	2743	3468	62
SI01V	18.2	9.2	8414	9362	65
SI01X	25.7	16.6	2059	2598	60
SI01Y	18.6	9.4	7893	8894	67
SI02U	17.4	10.8	11043	11633	71
SI02V	16.5	7.1	11449	11793	68
SI02X	—	—	—	—	—
SI02Y	15.0	7.0	15768	16465	66
SI03U	21.7	7.8	4081	5707	67
SI03V	19.1	6.1	7379	8828	66
SI03X	22.2	7.8	3913	5757	65
SI03Y	15.6	5.6	14154	15979	67
SI04U	15.9	8.6	25865	26410	75
SI04V	17.6	11.6	17919	19029	67
SI04X	18.6	11.2	15935	15935	69
SI04Y	19.1	11.8	14002	15088	62
SI05U	15.1	9.1	25356	25631	76
SI05V	16.2	9.9	21013	22202	69
SI05X	15.6	10.0	24991	25570	76
SI05Y	15.4	8.6	25633	27378	67

6.3 Amplitude Correlation

As introduced in Section 3.3.1, the COMPASS silicon detectors have a double sided readout. The projections read out on the two sides of a sensor thus have one common active volume, therefore the deposited energy from one particle passing through the detector is the same for both projections. Hence, the recorded signal amplitudes should agree within the noise margins of the electronics. This *amplitude correlation* is demonstrated in Fig. 6.4, where for each reconstructed track the cluster amplitudes (as

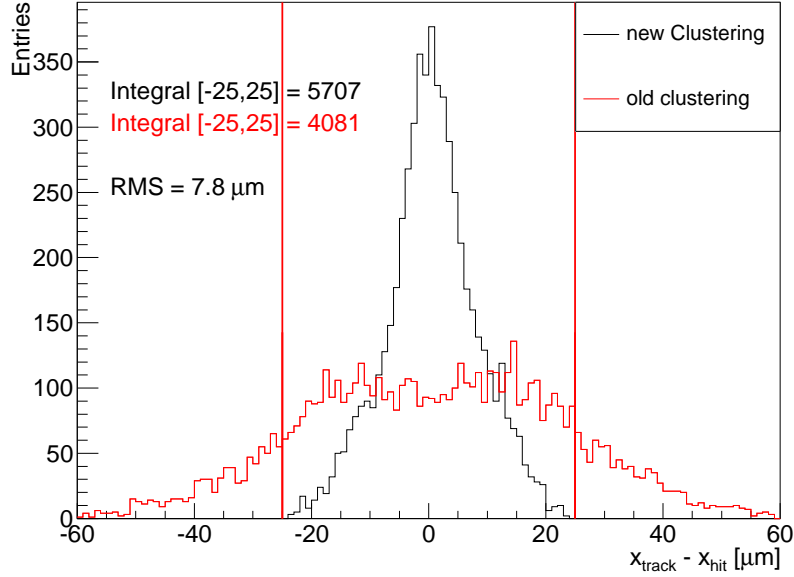


Figure 6.3: Comparison between old and new clustering as described in Section 6.2 using exactly the same data. Only clusters that showed the described structure are shown for the old clustering and the distribution for the new clustering is restricted to modified clusters. The plane presented here as an example is SI03U. The corresponding plots for the other silicon detectors together with a list of the used data are given in App. A.

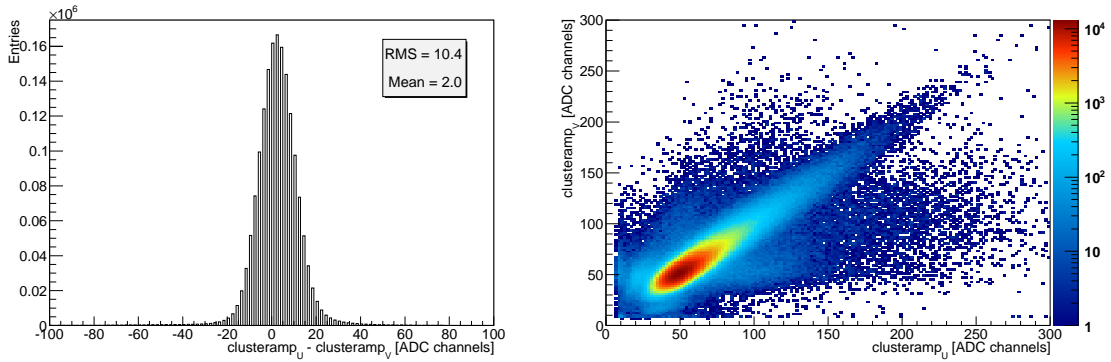


Figure 6.4: Amplitude correlation of SI02U and SI02V exemplarily. The Gaussian σ of the amplitude difference is 8 ADC channels.

introduced in Section 5.1) of the assigned clusters on the two projections on one wafer were compared. The additional information can be used to disentangle clusters from δ -electrons as well as from tracks creating overlapping clusters, because the latter ones are usually not overlapping in both projections. Such an approach was not implemented in CORAL prior to this thesis for several reasons. Firstly, CORAL is designed in a way that the clustering step is done inside the method `CsDetector::clusterize()`, which is called for each `CsDetector` separately [1], as by design each single silicon projection is one `CsDetector` object. For that reason, the raw information of for example SI01V is not directly available during the clustering step of SI01U. Secondly, significant effects on the tracking were expected, and thorough studies were needed before a new clustering could be used for mass production. During this work, the technical problem was solved and a first version of a new clustering exploiting the amplitude correlation was designed and implemented. Studies on the impact on the tracking have been performed.

6.3.1 Technical Aspect

As a definition, a pair of silicon projections which is physically on the same wafer is denoted as *mates*, and accordingly SI01V will be denoted as the *mate plane* of SI01U. The technical challenge was overcome by adding an additional member variable to the `CsSiTrackerDetector` class, holding a pointer to the mate plane. The method `CsSiTrackerDetector::clusterize()` had to be modified in way, that when called for all Y and U planes, nothing is done. On the other hand, during the clustering step of X and V, the projections skipped before have to be clustered additionally. This was done to be independent of the sequence in which the silicon planes are clustered in CORAL. Since the Cinderella clustering described in Section 3.6.2 is working as intended for most clusters, it was decided to keep it as the basis and add an additional step called *mate clustering* on top of it. Consequently, the Cinderella clustering is executed in all cases where the prerequisites (e.g. time calibration available) are fulfilled.

Below, the different steps of the mate clustering are described. From the output of the Cinderella clustering all clusters composed of three or more strips are selected. Other clusters are not affected by the new algorithm, especially the good performance for single- and double-strip clusters shown in Section 5 is not altered.

Amplitude Matching

For each selected cluster, it is tried to match the cluster amplitude with two clusters from the mate plane as precise as possible. The sum of the cluster amplitudes of the two selected clusters on the mate plane is denoted by a_{sum} in the following, while for the cluster amplitude of the cluster under examination a_{large} is used. The clusters on the mate plane contributing to a_{sum} are restricted on single- and double-strip clusters, which are required to have a minimum cluster amplitude of 20 ADC channels. This minimum amplitude was introduced to avoid usage of noise clusters. In this step of the process, the time information are not reliable, as the cluster which is considered

6.3 Amplitude Correlation

cut, has most probably a distorted time information making a simple time coincidence criterion between the three clusters hard to define. An extension could be to refit the signal of the large cluster, based on the amplitudes and reconstructed time information of the two selected mate clusters.

The outcome of the amplitude matching for SI05V and SI05U is shown in Fig. 6.5, namely the selected a_{sum} versus a_{large} . It should be stressed, that only the best found combination per event is shown and not the large number of combinations that was actually tried. The two-dimensional plot has a prominent diagonal band, in which a_{sum} and a_{large} agree well. Above this band an enrichment is present, where a_{sum} is larger than a_{large} . This can be identified with the peak at roughly -50 ADC channels in the distribution of the difference between a_{large} and a_{sum} shown in Fig. 6.6. This value agrees with the most probable signal of one particle, it is assumed that the particles that caused the large cluster in one projection were even closer in the mate projection, i.e. the clusters had a larger overlap. The resulting cluster in the mate projection has twice the most probable cluster amplitude distributed among only one or two strips. Similar findings are seen in Fig. 6.4(b) as non diagonal sub bands.

In addition, Fig. 6.5 shows a horizontal band for $a_{sum} < 40$ ADC channels. The corresponding one-dimensional distribution of a_{large} is shown in Fig. 6.6. Within this band several scenarios leading to clusters composed of three or more strips are included. For small values of a_{large} the distribution is dominated by clusters created from noise only, since a charge distribution where on three or more strips a signal was recorded, while the total cluster amplitude does not exceed 40 ADC channels seems unlikely to result from a real trajectory. Higher values a_{large} inside this band, that are not compatible with noise, are attributed to δ -electrons that create clusters larger than two strips in both projections at same time. The most probable amplitude is roughly 75 ADC channels. This fact supports the assumption of δ -electrons, because the MPV is too large to be noise and most likely not a result from two particles due to the small recorded amplitude. However, the latter case is attributed to the slight shoulder of the distribution around 110 ADC channels.

Depending on the outcome of the amplitude matching and the size of the cluster which is considered split, three cluster types are distinguished in the algorithm. The three cases are summed up in Table 6.3 and described in detail in the following.

Table 6.3: Naming convention of the different cluster types. The input size states the number of strips the input cluster is allowed to have in the particular category. In the last column the cluster size of possible outcomes is given.

Naming	Amplitude Matching	Input size	Nr. of created clusters	Output size
Real mates	successful	> 2	2	varying
Factor 0.5	failed	$= 3$	2	2+2
δ-clusters	failed	> 3	2	2+2

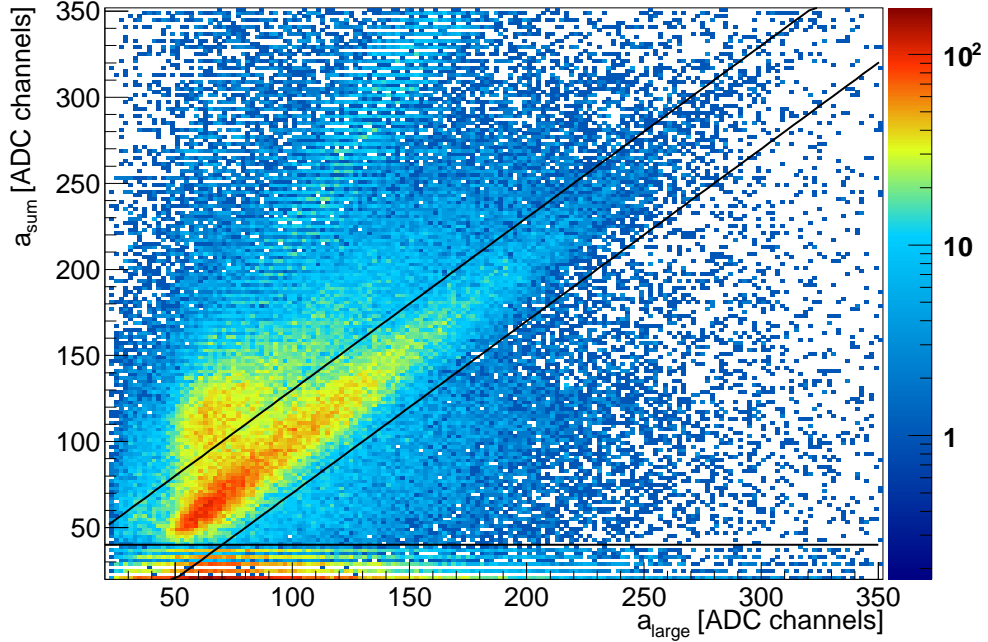


Figure 6.5: Cluster amplitudes a_{large} of clusters composed of three or more strips on SI05V, matched with the cluster amplitudes of two single- or double-strip clusters a_{sum} on SI05U. The lines indicate the domain around the diagonal where the amplitude matching is defined successful.

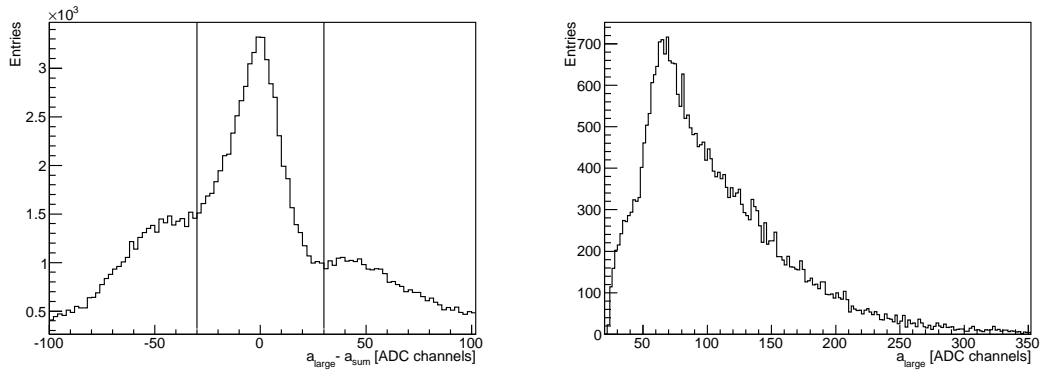


Figure 6.6: The left side shows the difference between a_{large} and a_{sum} . The right side is the cluster amplitude distribution of a_{large} for $a_{sum} < 40$ ADC channels, i.e. the one dimensional projection of the part of Fig. 6.5 that lies below the horizontal line. The most probable value is roughly at 75 ADC channels.

Real Mates

In Fig. 6.5 the outcome of the amplitude matching described above is shown. The plotted lines indicate the region where the amplitude matching is considered successful:

$$|a_{large} - a_{sum}| < 30 \text{ ADC channels} \quad \text{and} \quad a_{sum} > 40 \text{ ADC channels.} \quad (6.1)$$

The second cut arises from the fact, that each summand of a_{sum} is required to have a cluster amplitude of at least 20 ADC channels to avoid the use of noise clusters. This set of cuts should be considered preliminary, as no detailed studies on their impact have been conducted. In addition, for some planes the main band where the amplitude correlation is fulfilled differs from the bisection line, meaning that the rise is slightly steeper. The first cut therefore still has to be tuned carefully for each detector plane individually.

By utilizing the amplitude correlation additional information concerning the cluster under examination is extracted, namely the cluster amplitudes of the two original overlapping clusters, that were combined into one large cluster by the Cinderella clustering. However, information about the size of these clusters is lost, since the size depends strongly on the distance of the track's impact point from the next strip, as shown in Fig. 7.1. This quantity is different for both projections, for that reason it was decided not to restrict the size of the created clusters. The primary cluster is split according to the proportion of the cluster amplitudes of the two mate clusters. In more detail, the fraction of the cluster amplitude of the new created clusters is the same as for the two mate clusters. This however introduces an ambiguity, that can not be resolved, since one does not know on which side the small clusters should be created. The size of the new created clusters therefore depends on the specific case.

Factor 0.5

In case the amplitude matching was not successful, i.e. the best found combination does not fulfill the cuts given in Eq. 6.1 and the cluster under examination is composed of exactly three strips, two new double-strip clusters are created. Thus the middle strip has to be divided between the outer strips. For this division the factor 0.5 is used, but in principle every number between zero and one is possible. The basic situation is complicated to examine, since δ -electrons (see Section 6.3.1) and overlapping clusters resulting from several tracks are both expected in this category. For the latter case, the amplitudes of the outermost strips could contain information about the initial energy deposition of both tracks separately, and therefore a hint how to divide the middle strip. This is not case for clusters resulting from δ -electrons. An effective extension of the η -correction (see Section 3.18) for clusters composed of three strips is described in Section 6.6.

Even though the optimum performance might not be reached yet, it is nevertheless a significant improvement as shown in Section 6.3.2. The algorithm yields two new bordering clusters, with the possibility of one fake cluster being created. This is a cluster

without a corresponding particle. Such clusters are likely to be sorted out during the tracking, as a similar approach to resolve the left/right ambiguities of drift detectors is working well in CORAL [9]. Since the number of fake clusters is small compared to the overall number of clusters defining a track, the distortion of the track position is small. Therefore the fake cluster leads to a higher χ^2 value in the fit, compared to the corresponding track candidate where only the fake cluster was replaced by its partner. Thus the track candidate containing the fake cluster is ascribed a lower priority and then likely to be dropped during the cleaning stage. A description of the prepattern and tracking in CORAL is given in Section 2.4.1. On the contrary, the additional cluster may permit the reconstruction of an additional track, which is the intention behind the procedure.

δ -Clusters

Clusters composed of four strips or more are expected to result from δ -electrons, hence the label δ -clusters is used. δ -electrons are single high energetic electrons which can cause large clusters depending on the angle α with respect to the particle trajectory under which they are emitted. The number $dn/d\omega$ of δ -electrons per cm having energies between ω and $\omega + d\omega$ is given by [43]:

$$\frac{dn}{d\omega} = \frac{2\pi N}{mv^2} \frac{1}{\omega^2} \left[1 - \beta^2 \frac{\omega}{\omega_m} + \frac{\pi\beta}{137} \left(\frac{\omega}{\omega_m} \right)^2 \left(1 - \frac{\omega}{\omega_m} \right) \right] \quad (6.2)$$

where $\omega_m = 2mc^2\beta^2\gamma^2$, e and m are the electron's charge and mass and N the number of free electrons per cm^3 in the medium. From classical kinematics the ejection angle α between the original trajectory and the direction of the δ -electron can be calculated:

$$\cos^2 \alpha = \frac{\omega}{\omega_m} \quad (6.3)$$

The basic kinematics is sketched in Fig. 6.7. If emitted in forward direction, i.e. $\alpha \approx 0$, the distortion of the reconstructed track position should be small, because the δ electron is within the direct proximity of the charge cloud. However, the path of δ -electrons is a ziczac [40], this weakens the dependence of overall direction of the path to the emission angle. The δ -electrons emitted in forward direction have the highest energies, and therefore also the highest range in silicon.

A 40 GeV/ c pion has a 2.5% chance of creating a δ -electron of roughly 200 keV or more. Such a δ -electron has a range of almost 90 μm in silicon which is almost twice the readout pitch. Small distortions of the cluster position, i.e. one additional strip with a signal above noise level, are covered by the approach of the factor 0.5 clusters, described above. However the chance to create a δ -electron of 600 KeV is still 1% for the above mentioned pion. Such δ -electrons can traverse through the silicon bulk, because their range is roughly 450 μm [40]. This can shift the cluster position calculated according to Eq. 3.17 by multiples of the pitch, as the center of gravity is somewhere around the center of the cluster, depending on the exact amplitude values. The high energetic

delta electron introduces an asymmetry, the track lies in one of the outer borders of the cluster. Therefore, for all clusters composed of four strips and more, where the amplitude matching failed, two new clusters are created using on the one hand the first two and on the other the last two digits of the original cluster as shown in Fig. 6.7. The distance of the created cluster is larger than $50\ \mu\text{m}$, the second cluster is therefore in the majority of cases sorted out during the prepattern. The line of argument is similar to the one presented in the previous subsection.

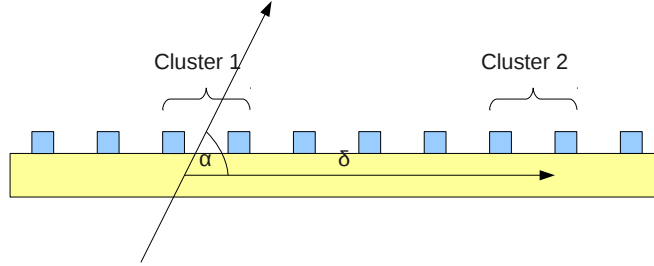


Figure 6.7: Basic kinematics behind δ -clusters. Two new clusters are created from on the one hand the first two and on the other the last two strips. The angle with respect to the particle trajectory, under which the δ -electron is emitted, is denoted with α .

6.3.2 Performance

In this section the results of the new mate clustering are discussed. Table 6.4 summarizes the main findings: The RMS of all affected clusters in comparison to the RMS of the identical clusters, as obtained with the Cinderella clustering, and the appearance of the different cluster classes, as introduced in Table 6.3. The RMS is reduced to less than half of the original value for all planes. The contribution from the factor 0.5 clusters clearly dominates with 50 to 75%. The splitting according to a reliable amplitude correlation works out in an average of 12%, where the values span from 5 to 22%. Having a closer look at Fig. 6.8, which shows the residual distribution separated into the different cluster classes, the most striking feature is again a double peak structure, but with a reduced offset of the two components. This is introduced by the factor 0.5 clusters, where the splitting factor is arbitrarily chosen to be 0.5. The real mate clusters show a well-defined peak, but are limited in statistics. The RMS is comparable to the RMS of the overall distribution. The δ -cluster distribution shows two smaller side peaks at roughly $\pm 30\ \mu\text{m}$. These are the cases, where the situation was rather more complex than the naive picture shown in Fig 6.7. It seems likely, that one of the two strips selected on the right side of the original cluster was actually noise, which could be cured by trying different strip selections towards the center of the large cluster until the outermost selected strip exceeds a threshold comparable to the one in Section 6.2. Another explanation could be, that two or more tracks with overlapping clusters were

present and only one of the tracks could be reconstructed. For an investigation of the latter scenario, the revised simulation of the silicon detector response as introduced in Chapter 7 could be of benefit.

Table 6.4: Summary of the mate clustering. RMS values for the clustering described in Section 6.3 with appearance of different contributions according to Table 6.3. The RMS for the corresponding clusters as calculated with the Cinderella clustering is given for comparison. As SI02X was rendered inoperable, no amplitude matching for SI02Y could be performed.

Plane	RMS _{new} [μm]	RMS _{old} [μm]	Real mates [%]	Factor 0.5 [%]	δ [%]
SI01U	15.0	38.4	18.0	60.2	21.8
SI01V	14.1	38.2	5.2	73.2	21.7
SI01X	15.1	38.7	9.4	66.4	24.1
SI01Y	14.1	38.9	10.2	67.1	22.7
SI02U	13.9	38.4	17.8	61.0	21.2
SI02V	13.5	38.4	6.4	69.8	23.9
SI02X	—	—	—	—	—
SI02Y	13.9	38.5	—	75.2	24.8
SI03U	14.7	38.1	17.0	60.4	22.6
SI03V	13.6	39.3	4.7	71.8	23.5
SI03X	14.6	39.0	10.3	66.0	23.7
SI03Y	14.3	36.4	8.6	71.2	20.2
SI04U	17.5	36.9	19.6	50.7	29.6
SI04V	18.6	39.8	12.5	57.6	29.9
SI04X	17.9	41.5	11.6	58.7	29.7
SI04Y	17.5	43.1	16.7	59.9	23.3
SI05U	15.4	36.8	21.8	50.7	27.6
SI05V	16.7	39.2	9.5	63.9	26.6
SI05X	16.1	38.3	14.2	55.7	30.1
SI05Y	16.5	37.5	13.7	65.2	21.1

6.4 Results

The impact on the tracking was studied using 28 chunks of Primakoff data from the year 2009. As a first step, misidentified 3 strip clusters were corrected. This increased the total number of events written to the mDST file, see Section 2.4.1, by 2.3%. The correlation is given, because in standard Primakoff production options only events where at least one primary vertex was found are written to the output file. As the cluster errors

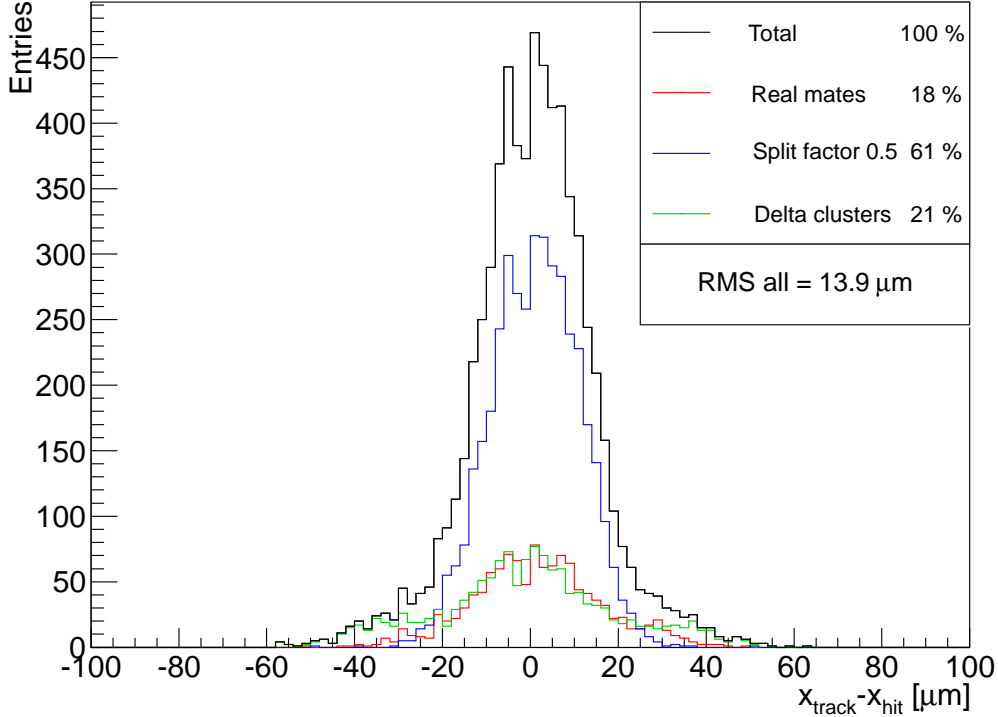


Figure 6.8: Residual distribution of the complete mate clustering introduced in Section 6.3, separated into the different contributions for SI02U.

were adjusted according to the uncertainties observed in real data, for this application the χ^2 value of the fit is not a good quantity to judge the track quality. Hence, the number of reconstructed tracks which were bridged at least over the first spectrometer magnet are counted, i.e. the tracks are required to begin within the conical cryostat and end behind the SM1. According to [52], physics cuts for the Primakoff analysis eliminate tracks with time offsets larger than 5 ns with respect to the trigger, hence an according cut is applied. Going from the Cinderella clustering to the first correction, which removes the noise strips, the number of these tracks increases by 0.5%. The new end point of the bridged tracks is uniformly distributed among the detectors behind SM1. On top of that, the impact of the mate clustering was tested, i.e. with the improvements already listed active additionally the mate clustering was used. The gain in the number of events is 0.2%, at the same time the number of good tracks increases by 0.3%. Complementary a first check on a physics channel was conducted [60]. Using different reconstruction options in CORAL, the number of reconstructed 3 charged pion diffractive dissociation (see Section 2.2.1) events out of the same chunk from 2008 data were counted. Depending on the exact reconstruction options, the gain

is between 0.25% and 2.3%. The best improvements are seen for the most sophisticated options. This means using the small silicon route width (Section 4.3.1) is obligatory, while this in turn conditions also the use of ROOT geometry (see Section 2.4.3). In addition, using special tracking options originally developed for the Primakoff analysis works very well in combination with the new clustering. These options essentially consist of a special bridging method (Section 2.4.1) for certain parts of the RICH detector, which contribute significantly to the material budget under small scattering angles. In this configuration the maximum gain of 2.3% is observed. From a logical point of view, the new clustering has the largest impact for the small mass region, where the decay angles are small and therefore tracks are more prone to overlap within a silicon projection. Hence, detailed studies using mass spectra are supposed to show even larger improvements for the low mass region.

6.5 Outlook: Particle Identification with COMPASS Silicon Detectors

A short investigation was done to test ideas to use the COMPASS silicon detectors for particle identification (PID) [29]. No detailed studies were conducted, but instead a short overview to some basic concepts, their applicability to the COMPASS environment and the COMPASS silicon detectors is briefly discussed. If more detailed studies show promise, a possible approach is roughly sketched.

One hypothesis was, whether the silicon vertex detectors could be used as a time of flight detector (ToF) for relativistic recoil protons from the target. Considering a recoil proton with a momentum of $1 \text{ GeV}/c$ a clear deviation of the protons velocity from the speed of light is present. Namely the velocity of such a proton is about $0.73c$ which translates with the 96 cm distance from the target to the last silicon detector inside the conical cryostat into a flight-time of 3.20 ns. Compared to a particle with $v \approx c$, this results in a difference of the flight-times of 1.2 ns. Combining the time information of the last two silicon planes according to Eq. 3.14 as done in Section 5.3, a time resolution of about 1.5 ns can be reached while the event time has an uncertainty of approximately 0.5 ns. Combining both uncertainties quadratically, the time resolution is roughly 1.6 ns which means a capability at the level of 0.75σ . However the best silicon detectors show a combined time resolution of 1 ns, which would mean 1.2σ confidence level. The reason why SI05XY has a worse performance is probably due to instabilities in the cooling, as well as a capacitor configuration that causes noise. Both shortcomings will be eliminated in the course of the preparations for the Primakoff run in 2012. A more elaborate study should be performed using the data recorded in 2012.

A further approach was to use dE/dx to identify recoil protons. According to Fig. 3.1 a difference of about a factor of two can be expected at $1 \text{ GeV}/c$ between protons ($\beta\gamma=1.1$) and pions ($\beta\gamma=5.2$). This increases rapidly for lower momenta, because the protons experience already the drastic rise in the energy loss for momenta lower than

6.5 Outlook: Particle Identification with COMPASS Silicon Detectors

the one of a MIP. The eight silicon planes behind the target can be used to measure a set of four consistent amplitude pairs, which are proportional to the deposited energy. These sets can be used to rule out statistical fluctuations in the energy deposit by using a truncated mean omitting the highest amplitude. Because the energy loss is distributed according to a Landau distribution, that is asymmetric towards high values, only the highest value is omitted, while the lowest can be used. A brief preexamination suffered from the fact, that the amplitude sample which is recorded, is usually not in agreement with the signals maximum amplitude. This causes a fluctuation of roughly 20% which can be corrected using the TCS phase and the theoretical signal shape, where the latter is given in [24].

The prepared data were used for another finding. Defining a new quantity Π [29]:

$$\Pi = \log_{10} [(a_{2,4U} - 60) \cdot (a_{2,4X} - 60) \cdot (a_{2,5U} - 60) \cdot (a_{2,5X} - 60)], \quad (6.4)$$

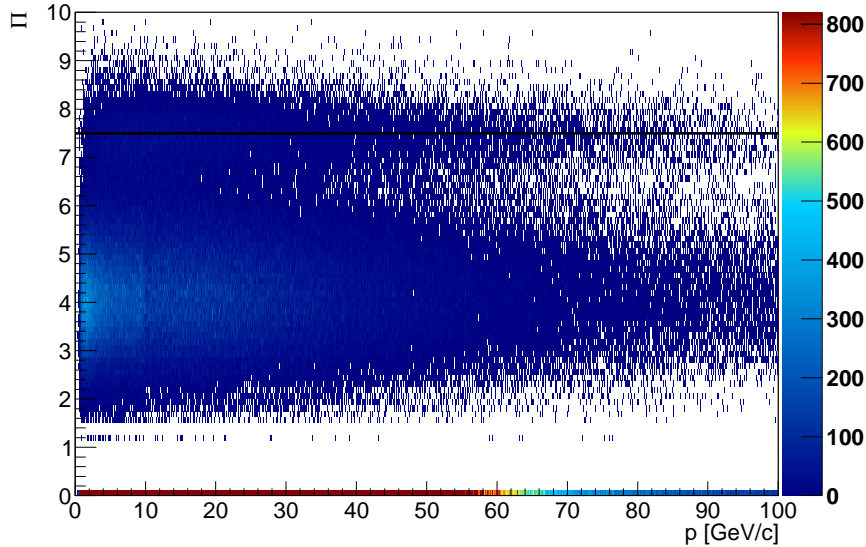


Figure 6.9: Π as defined in Eq. 6.4 over the particle momentum. The black line marks the band at $\Pi=7.5$, which corresponds to an average amplitude in the silicon of twice the most probable one. This band is supposed to stem from conversion electrons.

where $a_{2,ij}$ denote the amplitude samples observed in S_{ij}. In this particular definition only the X-like planes are included. Each pair of round brackets can be viewed as the deviation of the measured from the most probable amplitude. A plot of Π versus the particle momentum is shown in Fig. 6.9. The black horizontal line marks a sub band at $\Pi=7.5$, which is present in the data independent of the momentum. The seen thinning towards higher momenta is due to the underlying momentum distribution. In this band, every measured amplitude has roughly twice the most probable amplitude, independent

of the measured momentum. A possible explanation for this behavior are two tracks overlapping in at least one projection within some micrometer over the distance from SI04 to SI05 (i.e. 35 cm). Conversion electrons are expected to show this characteristics. In any case, at the moment there is no possibility to identify this type of tracks in the physics analysis. Due to the very small decay angles smaller than 1 mrad, the two tracks are quasi inevitably reconstructed as one track. The amplitudes measured in the silicons on the other hand are not available at the PHAST level, where the physics analysis is done. If these tracks are indeed created by conversion electrons, this information could be of great benefit for the Primakoff analysis though [29]. The second horizontal band around $\Pi=4.0$ can be explained by two tracks overlapping only in SI04 while in SI05 the distance was already sufficient to be resolved as two clusters. In addition, Fig. 6.9 shows a large enrichment in the first bin at $\Pi=0$. Every time in one projection a cluster amplitude of 60 ADC channels or less is measured, the corresponding factor in Eq. 6.4 is zero or negative and the same is true for the argument of the logarithm.

6.6 Conclusions and Outlook

During this work the basis for a way to a new COMPASS silicon clustering was built. A first version of the algorithm was implemented and tested up to a point, where it can be used as the standard clustering algorithm for data mass production. The new clustering showed promising performance in terms of reconstructed events, tracks bridged after SM1, as well as in a short test with a three pion final state physics channel. The recent results are preliminary and further developments will increase the performance of the system.

First of all, narrowing the route width of the silicon detectors (see Section 4) unbosomed, that for some detectors the average residual of single- and double-strip clusters differ by several μm . This is evident for Fig. A.6(d) where the mean values differ by roughly $2.5 \mu\text{m}$. Adding a shift to all single-strip clusters at the stage of the Cinderella clustering, an improvement of the total resolution in the order of some percent is expected. This position shift can not be compensated by the alignment, since here only the plane as a whole can be shifted, which affects clusters of all sizes the same way. Therefore an additional calibration file should be created. At best this could be combined with the long standing plan of implementing the detector resolution as a calibration file. This calibrations of course would have to be created carefully and additionally, since a significant impact on the cluster positions is expected. Therefore the need for a new (run-by-run) alignment in order to make full use of the improvements should be reviewed subsequently.

Secondly, the mate clustering offers a wide parameter space, which is still mostly unexplored. Detailed studies on the impact of minimal cluster amplitudes, absolute or relative cuts on the amplitude matching as well as including the time information should be conducted to release the full potential of the now available information. On any account a set of cuts that defines the success of the amplitude matching should be integrated

for each silicon detector individually.

The factor 0.5 clusters are the majority created in the new mate clustering, however the treatment of these clusters is probably not yet at its optimum. Under the assumption, that the large clusters was created from two overlapping clusters that result from two tracks, the outer strips contain to some extent information about the initial energy deposition of the two tracks separately. A promising approach is to apply Eq.3.18 to the first and the last strip of the cluster to calculate the optimal splitting factor as a function of this pseudo η . Then in the reconstruction the optimal value depending on the charge distribution of the outer strips could be used. This reasoning however does not work out for clusters created from δ -electrons, since here the charge cloud of the track and the δ -electron have a common origin. The success of the described approach therefore will at least partially depend on the relative abundance of clusters created from two tracks and δ -electrons. It should be possible to extract this number for the COMPASS silicon detectors during nominal beam conditions using the revised simulation of the detector response presented in Chapter 7.

Further the enrichment above the bisecting line in Fig. 6.5 and the side bands in Fig. 6.4(a), suggest to drop the limitation on clusters of size three or larger within the mate clustering. A profile at roughly 120 ADC channels, clearly shows two separated peaks. The main peak on the diagonal consists of single tracks where due to the statistical nature of the energy loss, a large energy was deposited and consistently detected in both planes, or of two tracks with overlapping clusters in both projections. Whereas for the secondary peak the detected amplitude in one plane is about half of the amplitude detected in the mate plane. This means that two tracks were actually overlapping in one projection, but not in the other. The long term objection should be to find one or several suitable mates for all clusters of a silicon plane. This way the bigger part of noise clusters could be suppressed.

With this in mind, the silicon Monte Carlo decoding was revised in Chapter 7, allowing now to use the full silicon clustering on Monte Carlo generated data. This allows to conduct new systematic studies to further improve the clustering algorithm.

Chapter 7

Simulation of the Detector Response

The COMGEANT software introduced in Section 2.4.3 is used to simulate the COMPASS spectrometer. Based on the trajectory position at the detector plane and the energy loss inside the active volume, the respective detector's response is then simulated within the digitization step of CORAL. The digitization of the COMPASS silicon microstrip detectors has been revised using Monte Carlo techniques to allow a systematic continuation of the analysis presented in the previous chapter. The general principle is introduced, followed by a detailed discussion of the various improvements conducted. An outlook on the impact of the performed revision as well as ideas for further improvements are presented.

7.1 General Principle

COMGEANT provides the *impact point* and the *exit point* of the trajectory to the detector plane's active volume, the *energy loss* inside the active volume as well as the *trigger time*. Using these quantities, the digits (see Section 2.4.1), thereafter processed in the clustering algorithm, have to be created. All detector characteristics are supposed to be simulated in way, that for once using the same algorithm on real data and on Monte Carlo data is possible and the distributions describing the detector's characteristics are as similar as possible to reality. For the case of the COMPASS silicon detectors this means starting from the above mentioned properties, realistic signal amplitudes with three samples, like the APV readout chip provides, have to be created. This is a prerequisite for using the standard clustering algorithm described in Section 3.6.2. Further the size of the cluster has to be appointed with the fraction of double-strip clusters compared to the total number of clusters being of particular interest. In case a double-strip cluster is created, the total charge (i.e. amplitude) has to be divided between the two strips. For all these quantities a phenomenological approach has been preferred to a microscopic model, as this offers the advantage of reliably reproducing all quantities which were taken account, while being reasonably fast. This advantage can not be neglected, since the steps introduced in this section are repeated up to hundred times per event. The chosen approach makes excessive use of *random numbers*. All main statistical distributions are implemented in CORAL¹. To account for noise in any

¹namely the CsRandom class

case usually a Gaussian distribution is used, while for any binary decisions e.g. the cluster size, uniformly distributed random numbers $\in[0;1]$ together with a probability distribution are applied.

7.2 Signal Amplitude

The initial point for the generation of the signal amplitude is the energy loss provided by COMGEANT. To emulate an amplitude correlation between the signals of two planes which are on the same wafer, the average of both values is used for further computation. In order to get the total created charge more realistic, it is randomized using several detector specific constants which have to be given in the CORAL options file. This way the total charge integral is obtained. The signal shape is taken into account by a special function adopted² from CORAL's `CsGEMDetector` class, returning the normalized amplitude ratios which are then used to create three samples similar to the APV readout chip. These parameters were tuned to reproduce the cluster amplitude distribution according to the real data case shown in Fig. 5.1. In addition, the time calibration for Monte Carlo data was redone³, as the used calibrations did not match the signal shape of the amplitude generator [60]. Using the signal generator to reproduce the time dependence of the ratios, the parameters of Eq. 3.6.1 could be determined for the MC signal generator⁴. The respective trigger time is smeared out according to a Gaussian and a noise contribution is added to the three signal samples, hence the final observed time distribution for the silicon planes is now a Gaussian centered around zero.

7.3 Cluster Size

For each simulated trajectory it has to be defined, on how many adjacent strips a signal above the noise level is created. This is closely related to the track's impact point on the detector plane and the propagation of the charge cloud. For the sake of simplicity, a phenomenological approach was chosen and restrained to single- and double strip clusters only. This is on all accounts reasonable, since these types account for more than 95 % of all clusters for nominal detector configuration. The distance of the particle trajectory's impact point on the sensor to the center of the nearest strip is denoted with x_{dist} :

$$x_{dist} = x_{track} - x_{strip} \tag{7.1}$$

For bins in x_{dist} the number of double-strip clusters was counted together with the total number of clusters (this is a flat distribution). Dividing both histograms one obtains

²Thanks to Phillip Zimmerer for this work.

³In combination with Monte Carlo data, hard coded calibrations are used, since typically no database connection is available.

⁴This calibrations are now hard coded in the CORAL source code.

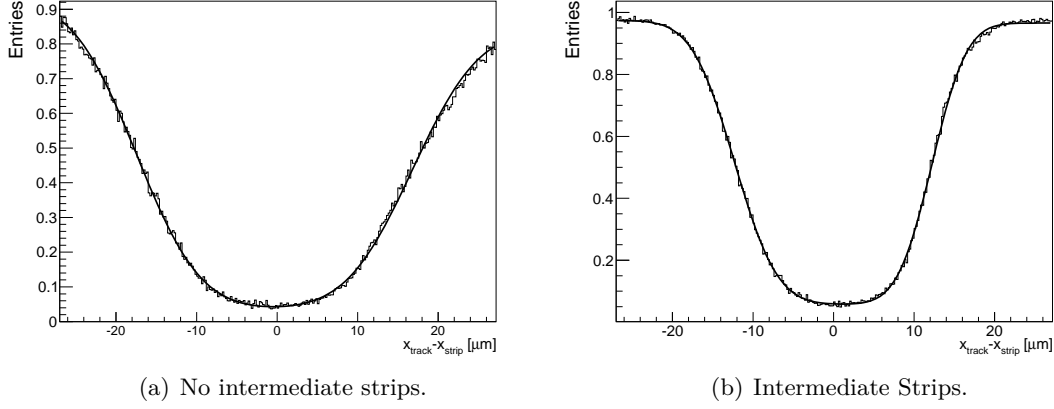


Figure 7.1: Probability for a double-strip cluster in bins of x_{dist} .

the probability for a double-strip cluster in bins of x_{dist} . The results for a sensor with and without intermediate strips are shown in Fig. 7.1. This distribution was fitted using

$$P_{cls}(x_{dist}) = a \cdot \text{Erf}\left(\frac{b - x_{dist}}{c}\right) + d \cdot \text{Erf}\left(\frac{x_{dist} - e}{f}\right) + g \quad (7.2)$$

with $\text{Erf}(x)$ being the Error function implemented in ROOT.

For a sensor with intermediate strips the obtained parameters are

$$a=0.45 \quad b=-17.46 \quad c=8.85 \quad d=0.40 \quad e=16.82 \quad f=9.18 \quad g=0.88, \quad (7.3)$$

whereas without intermediate strips the data can be described using

$$a=0.45 \quad b=-12.28 \quad c=5.92 \quad d=0.45 \quad e=12.24 \quad f=4.81 \quad g=0.97. \quad (7.4)$$

Inside the CORAL digitization step these functions are used to determine the size of a cluster. For this purpose Eq. 7.2 is evaluated using the extracted parameters and x_{dist} as given by COMGEANT and compared to a random number uniformly distributed in $[0;1]$. If the random number is smaller than the function value, a double-strip cluster is created, otherwise the whole charge is assigned to a single strip. The total fraction of double-strip clusters can be calculated by integrating Eq.7.2 and normalizing the result:

$$\text{Fraction of size 2 clusters} = \frac{\int_{-p/2}^{p/2} P_{cls}(x) dx}{\int_{-p/2}^{p/2} 1 \cdot dx} \quad (7.5)$$

with p being the detector's pitch. Calculating the integral numerically for Eq. 7.3 and Eq. 7.4, the result is 54.3% and 33.4 % for a plane with and without intermediate strips, respectively. The parameters were extracted for SI01Y (intermediate strips) and SI01X (no intermediate strips). A comparison of the simulated fraction to the value extracted from real data as given in Table 5.6 yields an agreement within two percent.

7.4 Charge Sharing

The charge sharing behavior is an important property of a silicon microstrip detector. Since the clustering algorithm works with the Center-of-Gravity Method introduced in Section 3.17, the charge sharing enters directly into the cluster position and has therefore a large impact on the reconstruction of Monte Carlo data. The quantity η , describing the charge sharing between two strips, was already introduced in Eq. 3.18. The distribution of η is simulated based on x_{dist} . As can be seen in Fig. 3.11, the features of the η -distribution change significantly in the presence of intermediate strips. In the following the relation between x_{dist} and the mean value of η is extracted and the algorithm as implemented in CORAL is presented for both cases separately.

7.4.1 No Intermediate Strips

In Fig. 7.3(a) η is shown versus x_{dist} for a sensor without intermediate strips. In the absence of intermediate strips the main part of the charge is usually collected on one strip, whereas collecting an equal amount of charge on both strips is more rare. The two-dimensional histogram was binned in η in order to obtain a set of one dimensional distributions (slices). This can be viewed as the distribution of x_{dist} for a fixed η . Within a bin of η the distribution can be approximated by a Gaussian up to a reasonable precision as shown in Fig. 7.2(a), while this is not true for vertical slices as shown in Fig. 7.2(b). Each slice was fitted using a Gaussian and the mean value $\overline{x_{dist}}$ as a function of η was found to be well described by:

$$\overline{x_{dist}}(\eta) = a \cdot \tanh(b \cdot (\eta - c)) + d + p/2 \quad (7.6)$$

with p being the detector's pitch. The values of the parameters were obtained by performing a χ^2 minimization within the ROOT framework.

$$a = 0.49 \quad b = -0.19 \quad c = 26.05 \quad d = 0.50 \quad (7.7)$$

Evaluating Function 7.6 with the parameters given in Eq. 7.7 can be seen as the solid black line in Fig. 7.3(a). Although reproducing the behavior not perfect, the obtained agreement is sufficient and as the hyperbolic tangent is implemented inside the standard math libraries, a fast evaluation inside CORAL is possible. In addition, all $x \in [0;pitch]$ are mapped to a physical value of $\eta \in [0;1]$. The function is symmetric around $\eta=0.5$ and $x_{dist}=26$, which is roughly pitch/2 and therefore meeting what was expected.

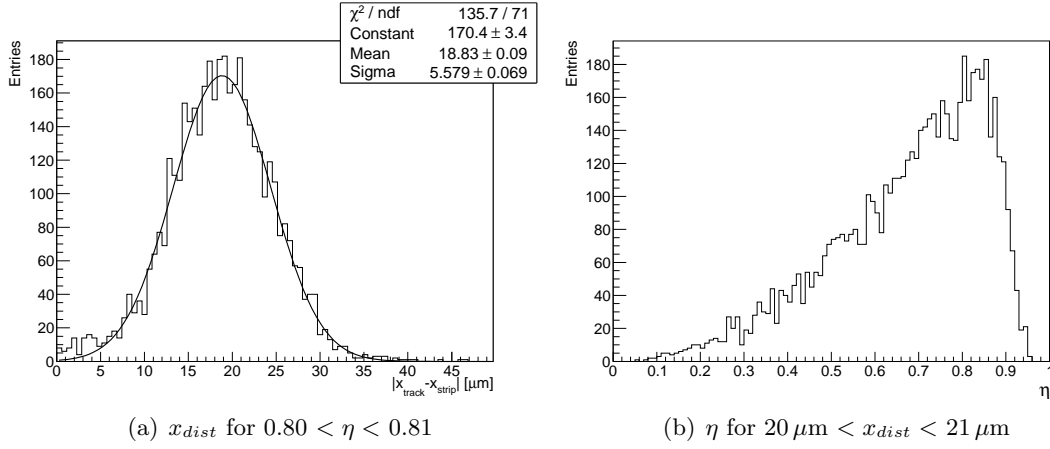
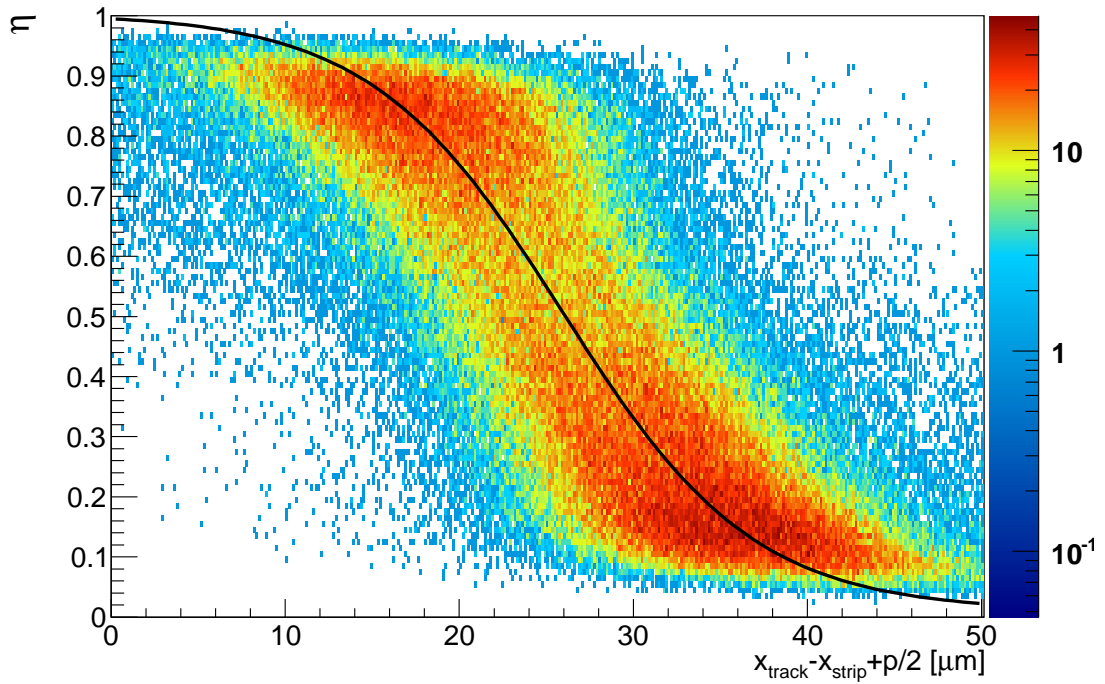


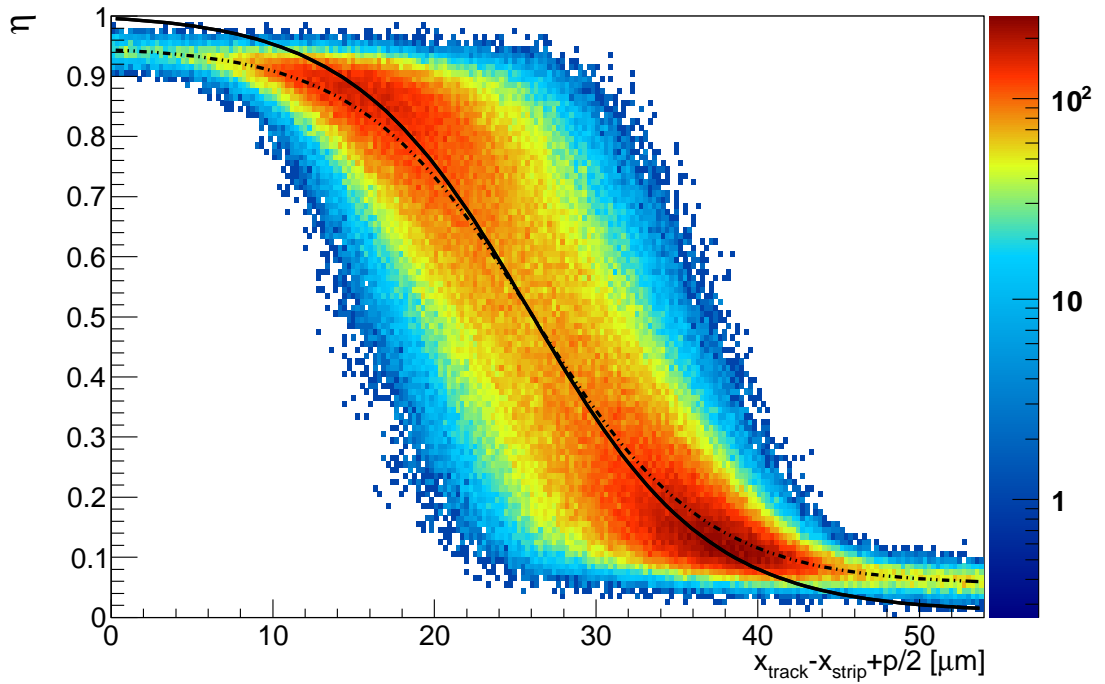
Figure 7.2: Exemplary one-dimensional distribution of Fig. 7.3(a) for a plane without intermediate strips.

Within the digitization step of CORAL, x_{dist} is the independent variable, i.e. for each simulated trajectory starting from x_{dist} , η has to be calculated. As shown in Fig. 7.2(b) the mapping from x_{dist} to η is not convenient within a bin of x_{dist} . Therefore a different approach was realized [29]. As mentioned above, within an η -bin the distribution of x_{dist} can be approximated by a Gaussian, where the mean value and the width σ were already determined for all slices. The width is constant at $\sigma_0=5.3$ up to a few percent over the whole range of η . This is a requirement for the developed algorithm. Starting with $x_{dist} = x$ the slice of η is calculated using Eq. 7.6 in which x_{dist} is distributed around the mean value x . Next a Gaussian random number with width σ_0 is obtained and added to x , resulting in x' . Once again, but now for x' , the value of η is calculated which is distributed around x' . This is the final result for η .

While this basic idea generally works, the result requires additional tuning. This comes from the fact, that emulating x_{dist} for fixed η with a Gaussian for $\eta \approx 1$ and $\eta \approx 0$ is a rather poor approximation since the distribution has an asymmetry towards $x=\text{pitch}/2$. Further, Eq. 7.6 fails to reproduce the distribution in this region, yielding values for η which are not present in real data, as the fit is largely determined by the data points around the center. Towards the borders, the tanh is too flat, leading to a too pronounced enrichment of the peaks in Fig. 7.4(a). To cure these problems, several steps were taken. For one thing, parameter a in Eq.7.7 was changed from 0.49 to 0.45. Figure 7.3(b) shows the function both with the original (solid line) and the modified parameter (dashed line) respectively. This is a scaling of the function in η which affects mainly the asymptotes, while the overall shape especially around the symmetry point is only changed slightly. The physical meaning is to limit the accessible range of η to be in agreement with the real data case. This measure corrects for accessible values of η within the algorithm, but not for the slope at the outliers.



(a) Real data



(b) Simulation

Figure 7.3: Charge sharing distribution versus the distance of the particle trajectory from the next strip, derived from real data (a) and obtained from simulation (b) for a plane without intermediate strips. The solid line is the function given Eq. 7.6 with the parameters presented in Eq. 7.7, while for the dashed line a was changed from 0.49 to 0.45.

The next step was to account for the track position entering in Fig. 7.3(a), which is only known up to a certain precision (usually better than $3 \mu\text{m}$) for real data. To account for this fact, at the start of the algorithm x is randomized by a Gaussian distribution. To tackle the problem introduced by the slope, a shift towards the middle depending linearly on x_{dist} is favored by up to a factor of 2. As a last step, the electronics noise contribution inevitably observed in Fig. 7.3(a) is added in the simulation by slightly randomizing the outcome η of the original algorithm with a Gaussian distribution. The simulated distribution can be compared to real data in Fig. 7.3, while Fig. 7.4 shows a comparison of the one dimensional projection. The ratio of the peak intensities to the minimum around 0.5 is for both peaks reproduced quite nicely. Also the peak positions (≈ 0.14 and ≈ 0.86) are reproduced within some percent.

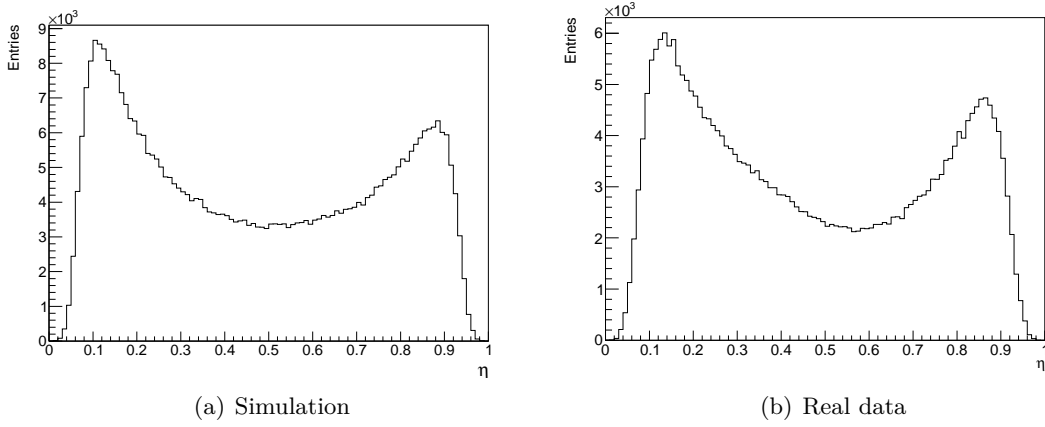


Figure 7.4: Comparison between the simulated charge sharing and the corresponding distribution extracted from real data for a plane without intermediate strips.

7.4.2 Intermediate Strips

The starting point for the simulation of the charge sharing is again the distribution of η versus x_{dist} as shown in Fig. 7.6(a). In contrast to Section 7.4.1, here a binning in fixed values of x_{dist} is useful, because within these bins the distribution of η is nearly Gaussian as shown in Fig 7.5(a).

This simplifies the algorithm considerably. Again the two-dimensional distribution was converted to one-dimension for pragmatic reasons. This was done by fitting the separate bins with a Gaussian and showing the mean value $\bar{\eta}$ versus x_{dist} . The average η as a function of x_{dist} can be described by the product of two hyperbolic tangents, where p is the detector's pitch:

$$\bar{\eta}(x_{dist}) = a \left(\tanh \left(\frac{b - x_{dist} - p/2}{c} \right) + d \right) \cdot e \left(\tanh \left(\frac{f - x_{dist} - p/2}{g} \right) + h \right). \quad (7.8)$$

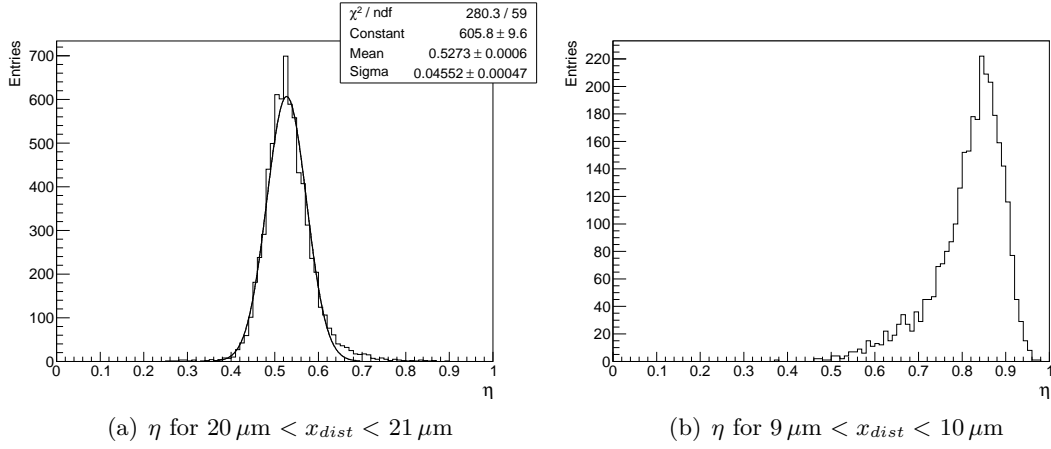


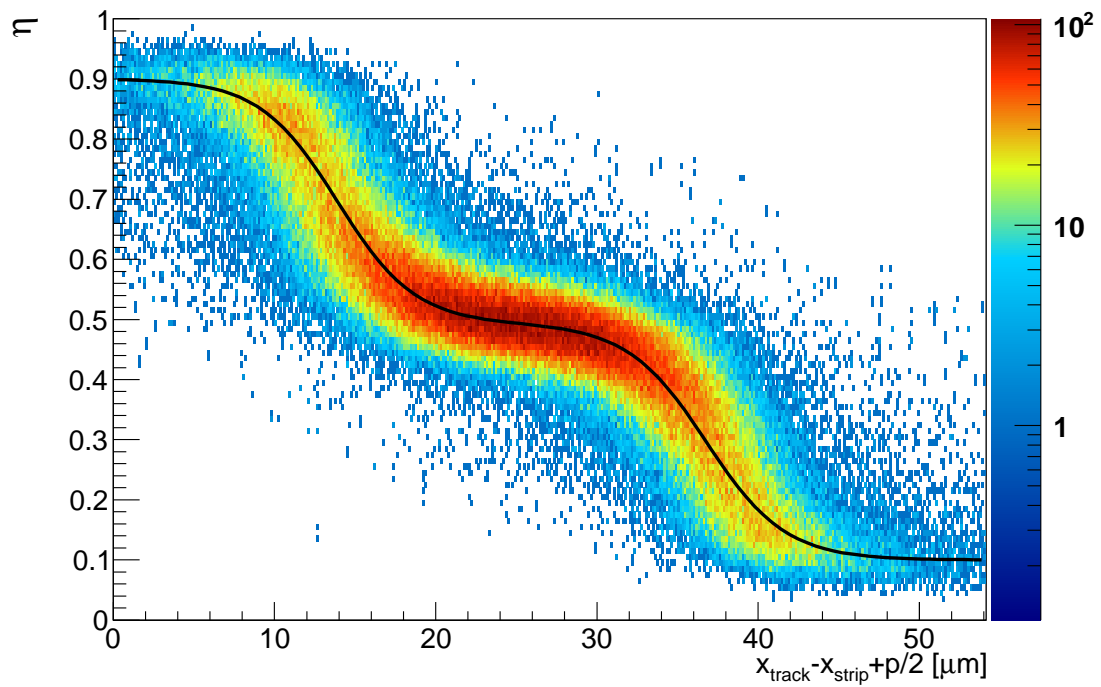
Figure 7.5: Exemplary one-dimensional distribution of Fig. 7.6(a) for a detector with intermediate strips. While (a) is reasonably described by the Gaussian fit, (b) shows an asymmetry towards $\eta=0.5$.

A χ^2 minimization yields the following results:

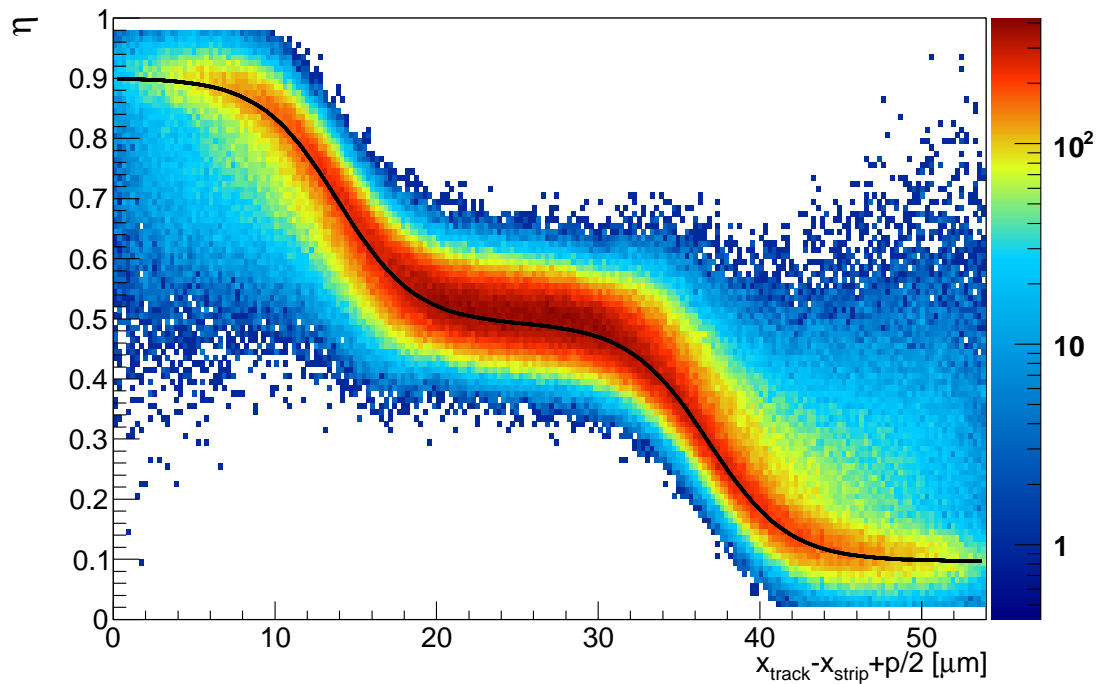
$$\begin{aligned}
 a=1.42 & & b=36.84 & & c=4.99 & & d=2.11 \\
 e=0.05 & & f=13.89 & & g=4.80 & & h=0.20
 \end{aligned}
 \tag{7.9}$$

The basic procedure looks as follows: Starting with a fixed value of $x_{dist} = x$, the track uncertainty is taken into account by randomizing x via a Gaussian. From here, again using a Gaussian random number distributed around the value given by Eq. 7.8, η is obtained. Once again, approximating the distribution within one bin of x_{dist} is only valid for the central part as shown in Fig. 7.5(b). This is compensated, with an additional weighting factor when obtaining η . For Gaussian shifts towards $\eta=0.5$ the shift is amplified with a weight rising linearly with x_{dist} -pitch/2. In addition, the range of observable values for η should be the same for real data and in the simulation. As a consequence, the algorithm is redone, when the final result is not in valid range, namely $\eta \notin [0.02;0.98]$.

The outcome as two-dimensional distribution is shown in Fig. 7.6. The projection into the one-dimensional charge sharing distribution is shown in Fig. 7.7 together with the real data case. The overall agreement is quite reasonable, while via introducing the asymmetric weight also small artificial structures have been introduced. Since the deviation is sufficiently small, the presented approach was chosen for implementation.



(a) Real data



(b) Simulation

Figure 7.6: Charge sharing distribution versus the distance of the particle trajectory from the next strip, derived from real data (a) and obtained from simulation (b) for a plane with intermediate strips. The function is of the form given in Eq. 7.8 with the parameters presented in Eq. 7.9

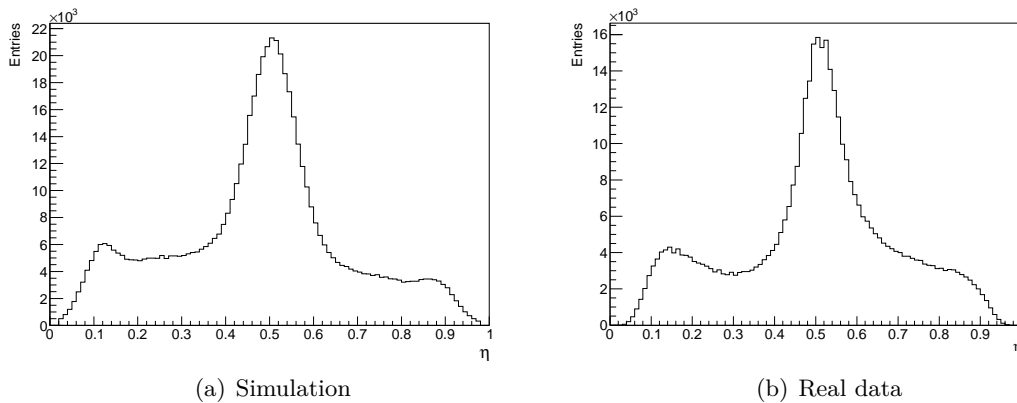


Figure 7.7: Comparison between the simulated charge sharing and the corresponding distribution extracted from real data for a plane with intermediate strips.

7.5 Conclusion and Outlook

The simulation of the detector response of the silicon microstrip detectors in CORAL has been revised within this thesis, now reproducing the main characteristics, as there are a reasonable number of double-strip clusters and a realistic charge sharing behavior. Now that it is reasonable for the first time to use the silicons clustering algorithm with Monte Carlo data, one has the tools at hand to revisit the analysis presented in the previous chapter and make new systematic studies. Although clusters of three or more strips are not yet explicitly created in the simulation, such clusters are nevertheless observed for Monte Carlo data as a result of tracks creating overlapping clusters. This is exactly the field of application of the real mate clustering presented in Section 6.3. Nevertheless there is still room for optimization left: An approach to create clusters composed of three or more strips including a realistic description of δ -electrons needs to be found and implemented. Usage of original calibrations for signal generation as well as reconstruction could be realized, but would require a MySQL database at all large computing centers used for COMPASS Monte Carlo computation. Another milestone is to include noisy and dead channels in the simulation, which would allow exact simulation of local inefficiencies in the detectors. These properties would have to be extracted from real data of the respective data taking period and again stored in a database. Created cluster positions could be compared to the strip numbers stored in the database and certain modifications of the cluster could be conducted. This could mean erasing the cluster for dead strips or blurring the position and time information for noisy strips.

Chapter 8

Conclusion and Outlook

The alignment of the spectrometer, and in particular the silicon detectors, during the 2009 Primakoff run was studied (see Chapter 4). For a precision Primakoff measurement the full potential of the COMPASS silicon detectors needs to be utilized to obtain the required resolution of the scattering angle of better than $100 \mu\text{rad}$. Therefore a precise alignment, which means the offsets of the silicon detectors need to be smaller than $1 \mu\text{m}$ for every physics run, is necessary. To fulfill these demanding requirements an alignment on a run-by-run basis is essential. This becomes even more important for a successful Primakoff beam time in 2012, when the pion polarizabilities shall be measured with unprecedented precision. Two silicon stations downstream of the target together with the other small area trackers upstream of SM1 need to be aligned properly for a reliable determination of the scattering angle. Therefore, also the relative alignment between the VSAT and SAT has to be done with great care. One way is to use tracks precisely reconstructed with the silicon detectors inside the conical cryostat, and align the rest of the spectrometer with respect to those.

During the 2009 beam time the silicon detectors were operated stably at 200 K. With the precise alignment available, the silicon detector performance was analyzed (see Chapter 5). A significant improvement compared to an earlier analysis is shown as the spatial resolution improved from $8 \mu\text{m}$ to $7 \mu\text{m}$ and from $11 \mu\text{m}$ to $9 \mu\text{m}$ for sensors with and without intermediate strips, respectively. The time resolution improved due to cryogenic operation from 3.0 ns to 1.8 ns and from 2.0 ns to 1.4 ns for sensors with and without intermediate strips, respectively. The average efficiency is above 99%. The overall improvements can be attributed to cryogenic operation and the new alignment. For the detectors inside the conical cryostat a capacitor configuration was used that increases the noise. Although this is visible in the data, the performance of these detectors is nevertheless pleasing. Since additional measures were taken to compensate for noise (see Section 6.2), it is not regarded as necessary at all costs to remove these capacitors, however the performance is likely to be improved in this case. As the cooling was shown to enhance the detector performance and stabilize the readout, continuation of the cryogenic operation should be intended. Instabilities in the cooling are likely to have degraded the time resolution of the detectors inside the conical cryostat, thus a repair of the cooling circuit for these detectors is planned before the run in 2012.

Chapter 8 Conclusion and Outlook

An extended clustering algorithm was developed and implemented. One part compensates for detector noise during the clustering step. Further, within the scope of this extension the amplitude correlation was utilized in the reconstruction process for the first time. All results achieved are promising, as the RMS of the residual distribution of modified clusters was significantly reduced for all detectors (see Chapter 6) and the reconstruction efficiency of exclusive three charged pions events was improved by up to 2.3%. More detailed studies restricted to the low mass region, where tracks are more prone to create overlapping clusters, are likely to show even more significant improvements. Now that the technical obstacles have been overcome, an efficient continuation can be expected as the potential is not yet fully utilized. In view of this fact, the simulation of the detector response was revised allowing now to use the full clustering algorithm also on Monte Carlo generated data (see Chapter 7). This permits a systematic refinement of the presented algorithms by reliably identifying overlapping clusters from several tracks within the simulation and studying their occurrence as well as their structure. With the gained insights and the exclusion principle it should be possible to extract a clean sample of clusters created from δ electrons from real data. By this means their properties can be studied in detail allowing additional refinement of the clustering algorithm. Furthermore their properties can then also be modeled and integrated into the detector simulation.

Appendix A

Performance Plots and Histograms

Used Runs

Table A.1: Used runs for clustering and determination of the time resolution. Only the listed chunks were used.

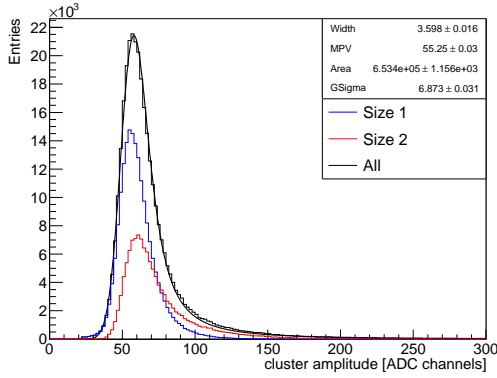
Run Nr.	Chunks	Comments	Purpose
81819	22001 - 22015 22018 - 22030 22032 - 22033	Primakoff Run Hadron beam	Clustering
81974	22002 - 22007	Primkaoff Run Muon beam	Time resolution

Table A.2: Used runs for determination of the efficiency and the spatial resolution. In each case the complete run was used.

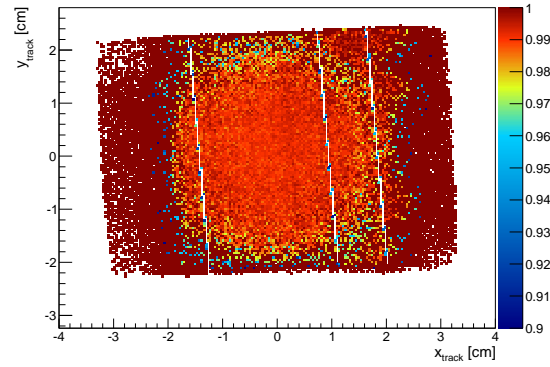
Run Nr.	Comments	Purpose
81970, 81971, 81973, 81974, 81975, 81976, 81977, 81978, 81980, 81981, 81982, 81983, 81985, 81986, 81991, 81992, 81993, 81994, 82000, 82001	Primakoff Runs Muon beam	Efficiency
81971, 81973, 81975, 81980, 81981, 81991	Primakoff Runs Muon beam	Spatial resolution

Appendix A Performance Plots and Histograms

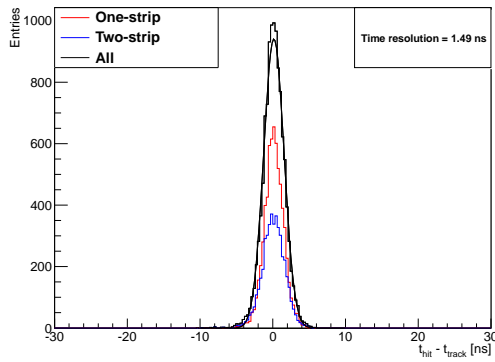
SI01U



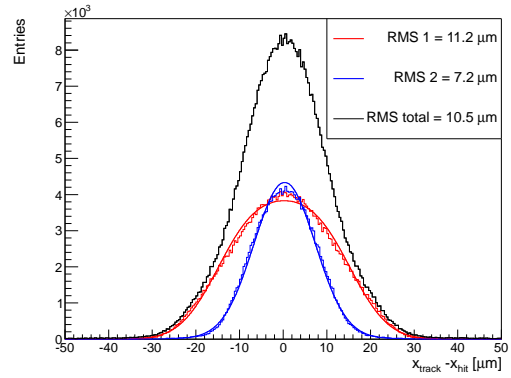
(a) Cluster amplitude



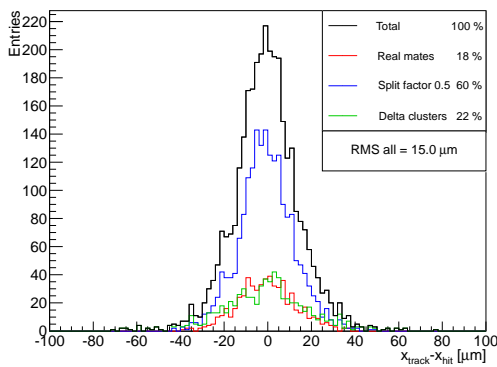
(b) Efficiency



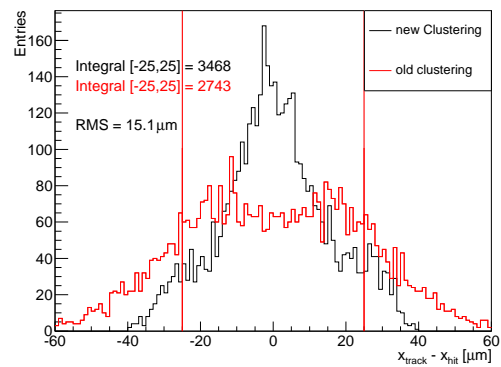
(c) Time Residual



(d) Spatial Residual



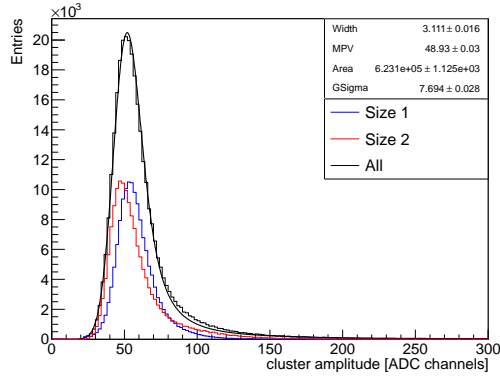
(e) Mate Clustering



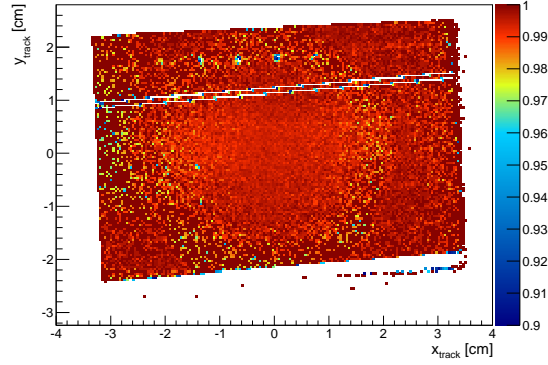
(f) Misidentified double-strip clusters

Figure A.1: Performance plots for SI01U.

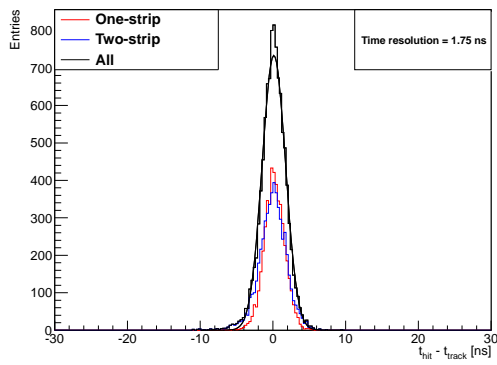
SI01V



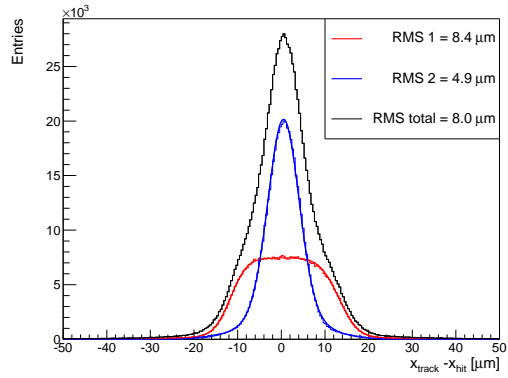
(a) Cluster amplitude



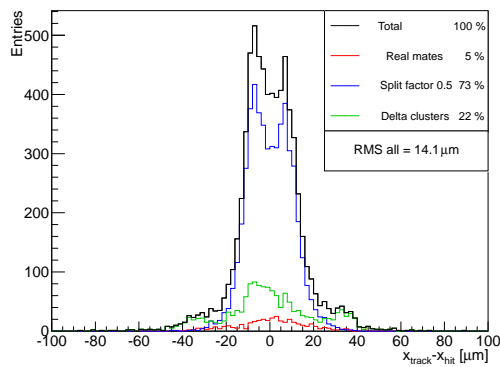
(b) Efficiency



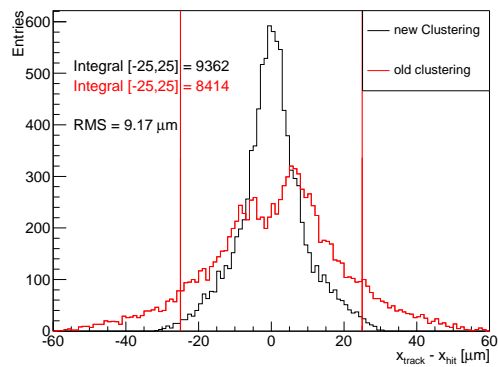
(c) Time Residual



(d) Spatial Residual



(e) Mate Clustering

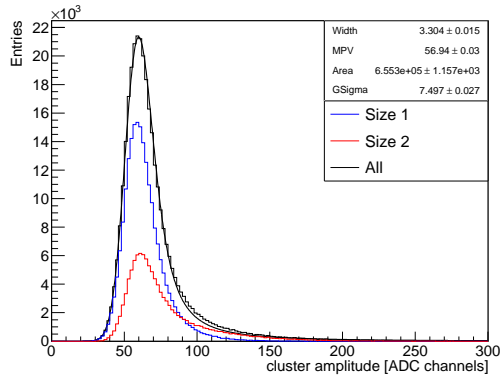


(f) Misidentified double-strip clusters

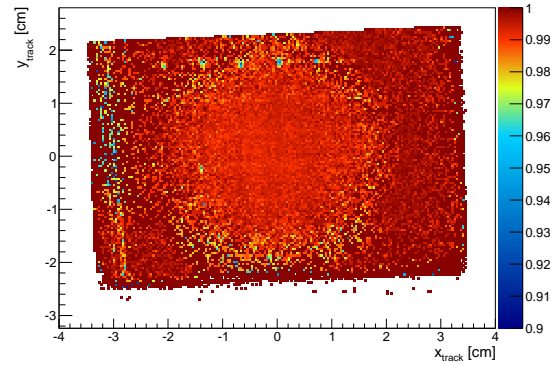
Figure A.2: Performance plots for SI01V.

Appendix A Performance Plots and Histograms

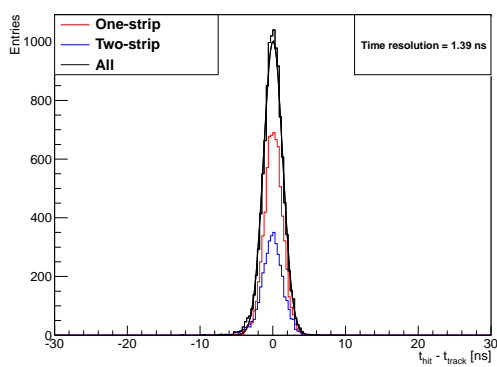
SI01X



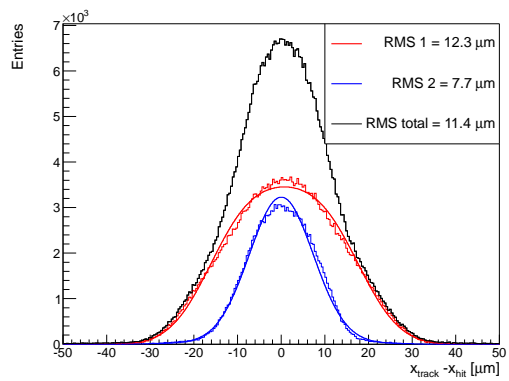
(a) Cluster amplitude



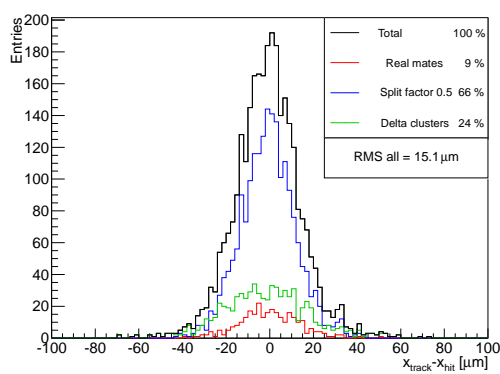
(b) Efficiency



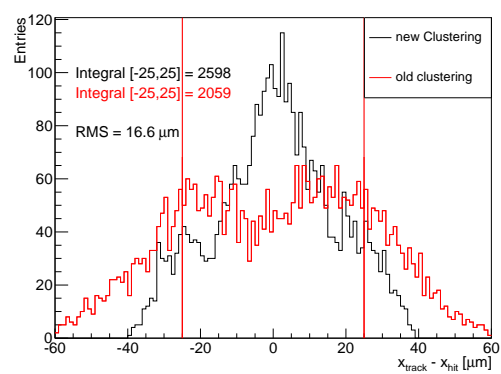
(c) Time Residual



(d) Spatial Residual



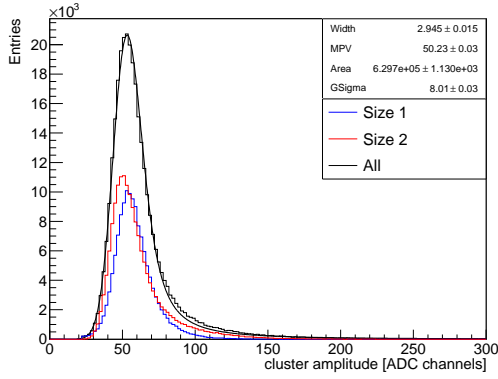
(e) Mate Clustering



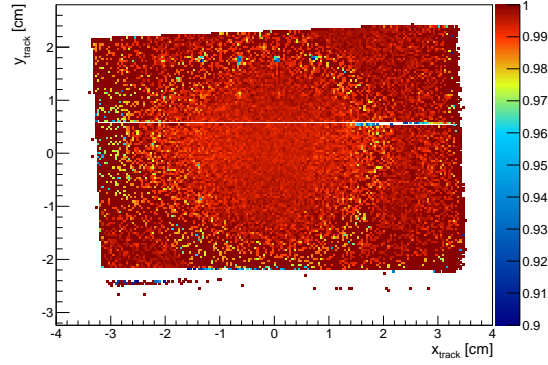
(f) Misidentified double-strip clusters

Figure A.3: Performance plots for SI01X.

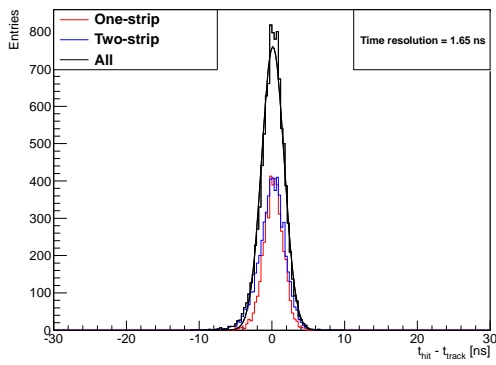
SI01Y



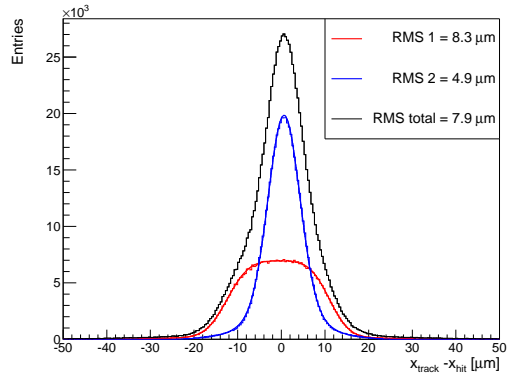
(a) Cluster amplitude



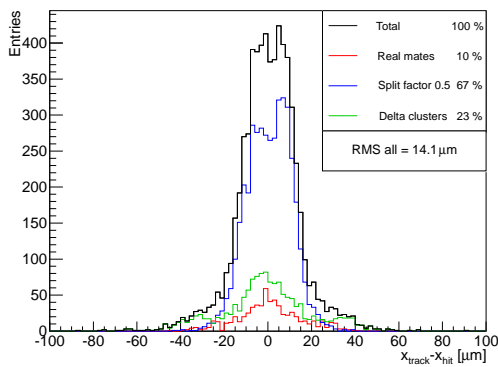
(b) Efficiency



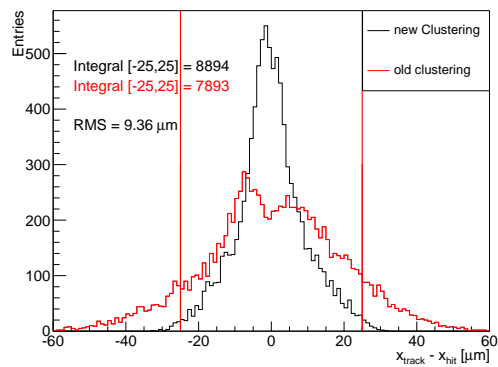
(c) Time Residual



(d) Spatial Residual



(e) Mate Clustering

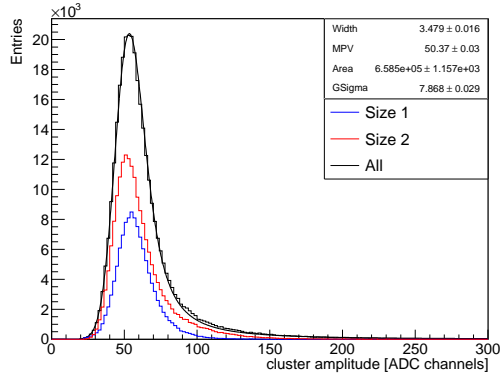


(f) Misidentified double-strip clusters

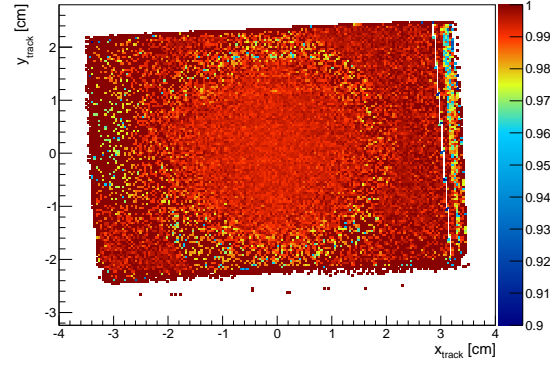
Figure A.4: Performance plots for SI01Y.

Appendix A Performance Plots and Histograms

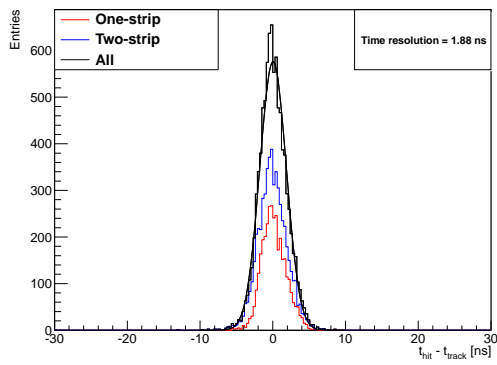
SI02U



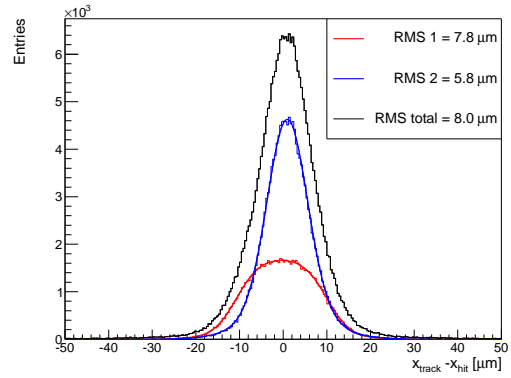
(a) Cluster amplitude



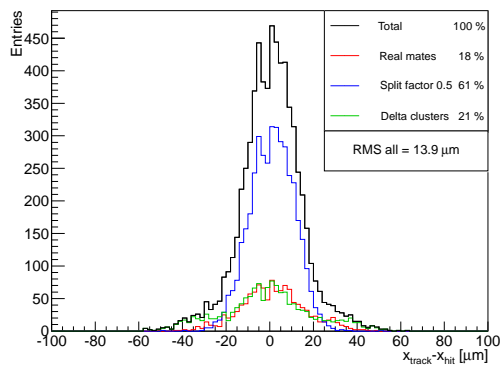
(b) Efficiency



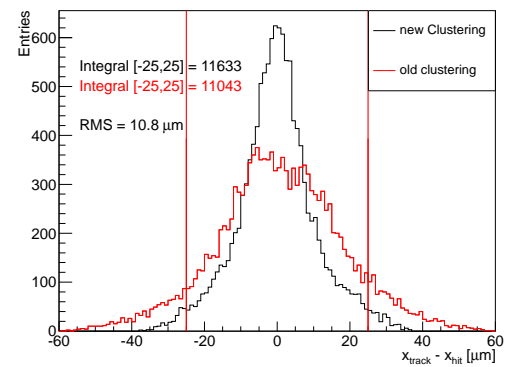
(c) Time Residual



(d) Spatial Residual



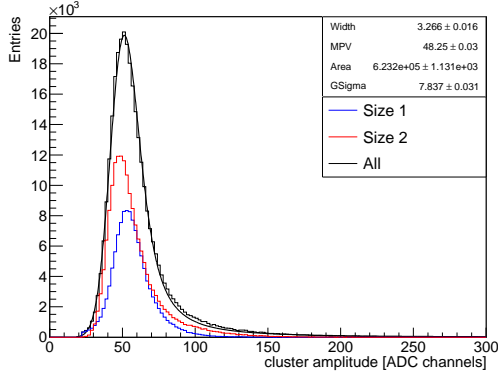
(e) Mate Clustering



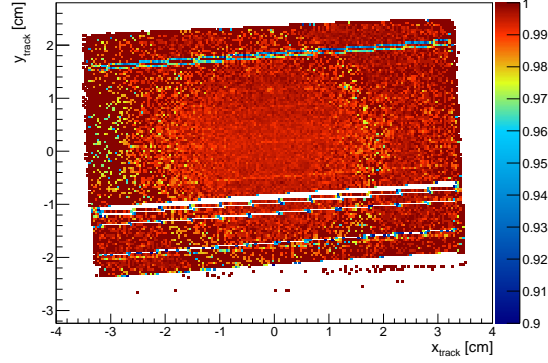
(f) Misidentified double-strip clusters

Figure A.5: Performance plots for SI02U.

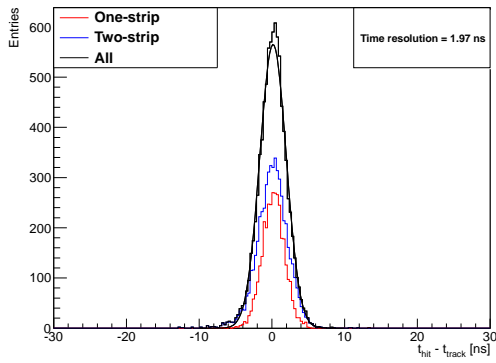
SI02V



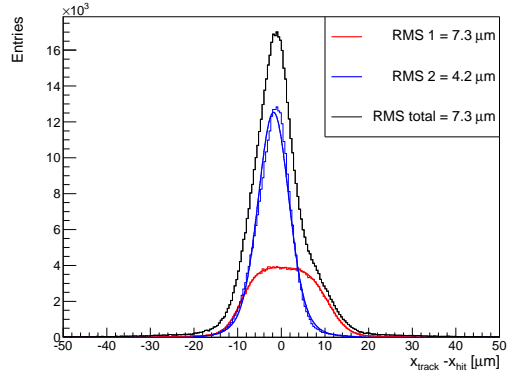
(a) Cluster amplitude



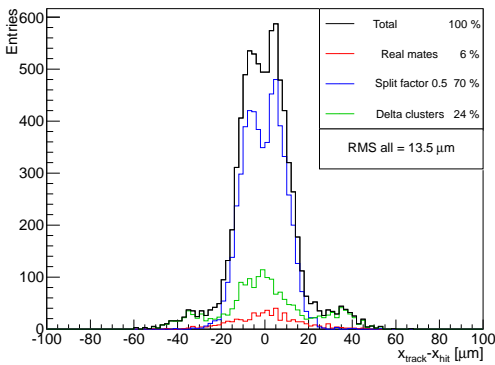
(b) Efficiency



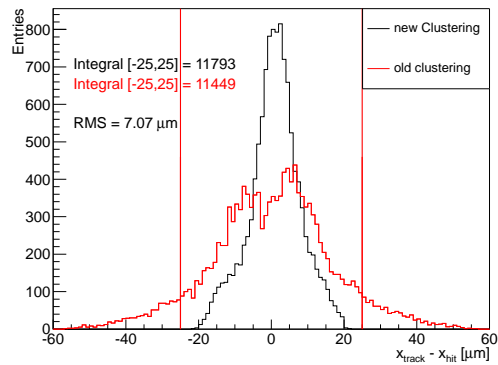
(c) Time Residual



(d) Spatial Residual



(e) Mate Clustering



(f) Misidentified double-strip clusters

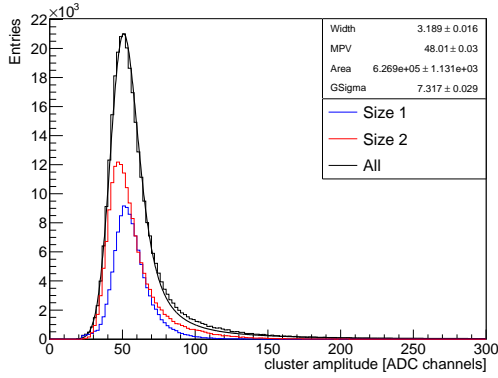
Figure A.6: Performance plots for SI02V.

Appendix A Performance Plots and Histograms

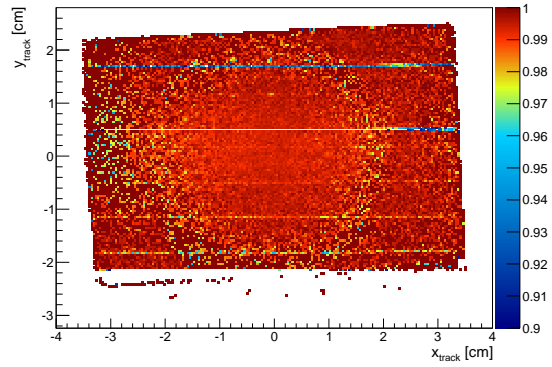
SI02X

SI02X was rendered inoperable in an incident at the beginning of the Primakoff period.

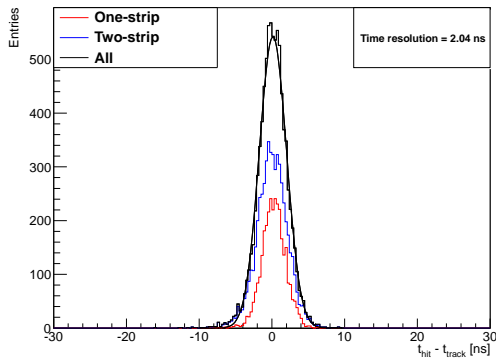
SI02Y



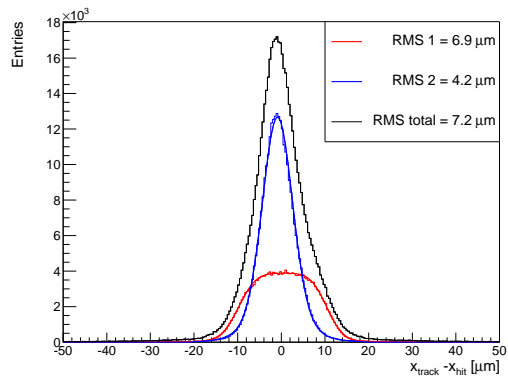
(a) Cluster amplitude



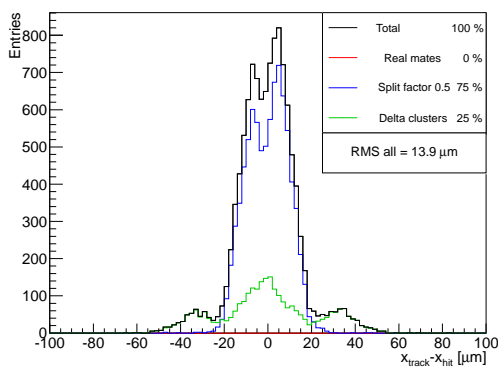
(b) Efficiency



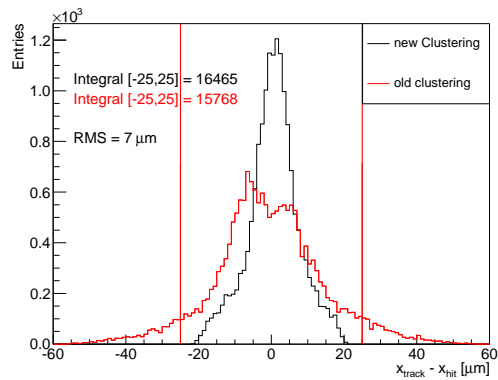
(c) Time Residual



(d) Spatial Residual



(e) Mate Clustering

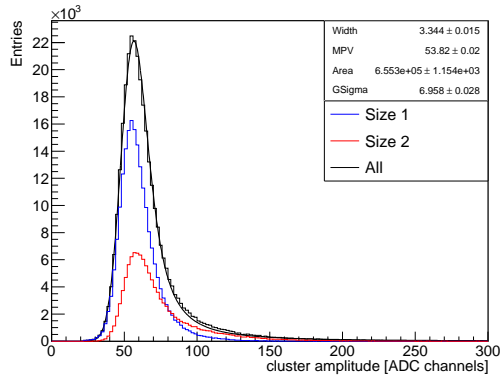


(f) Misidentified double-strip clusters

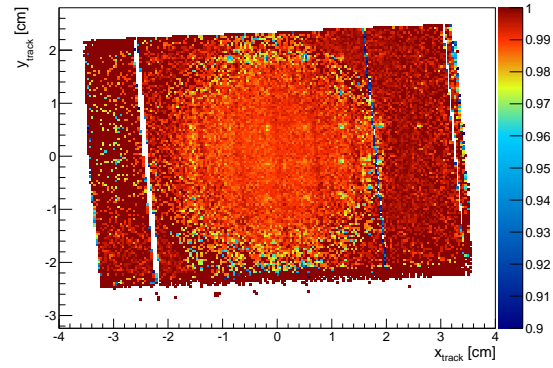
Figure A.7: Performance plots for SI02Y.

Appendix A Performance Plots and Histograms

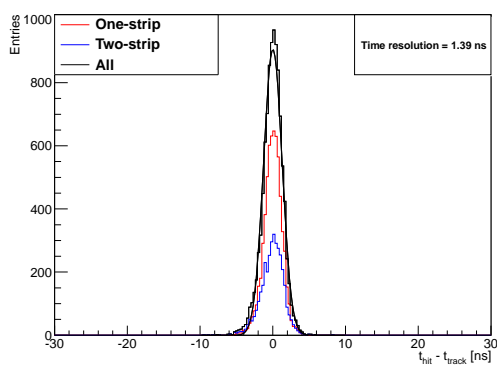
SI03U



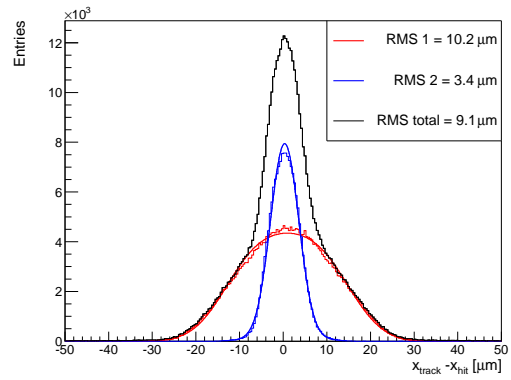
(a) Cluster amplitude



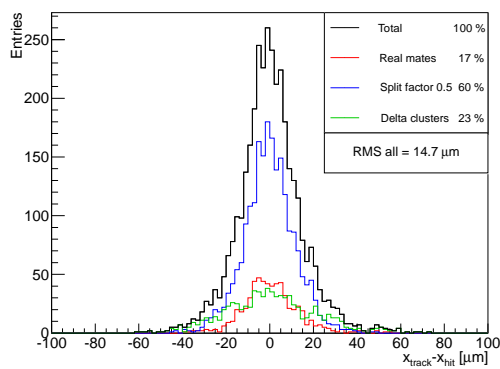
(b) Efficiency



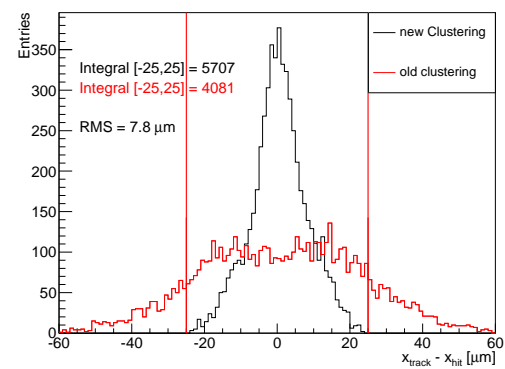
(c) Time Residual



(d) Spatial Residual



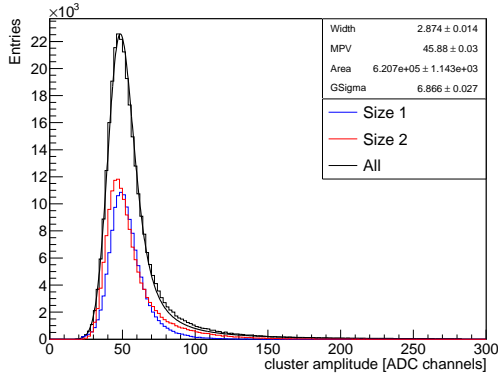
(e) Mate Clustering



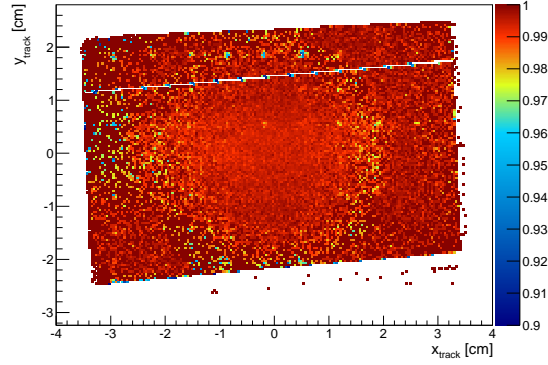
(f) Misidentified double-strip clusters

Figure A.8: Performance plots for SI03U.

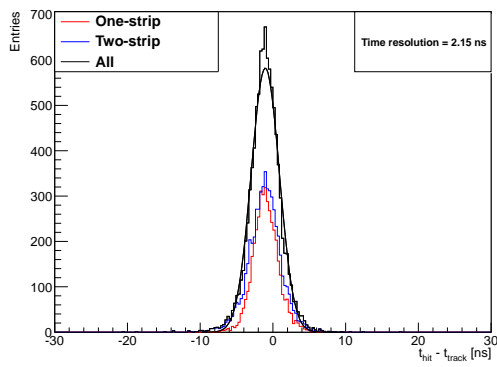
SI03V



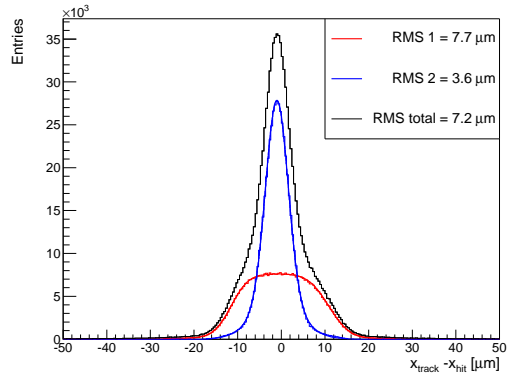
(a) Cluster amplitude



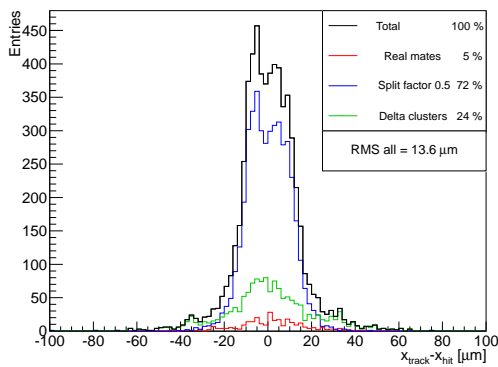
(b) Efficiency



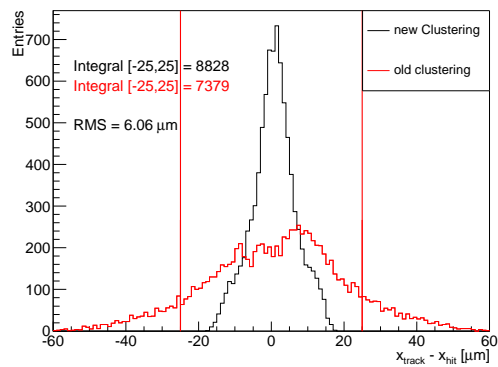
(c) Time Residual



(d) Spatial Residual



(e) Mate Clustering

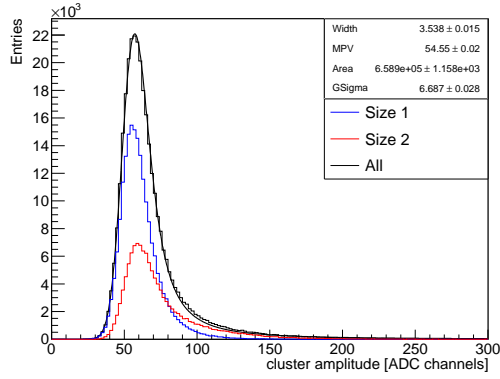


(f) Misidentified double-strip clusters

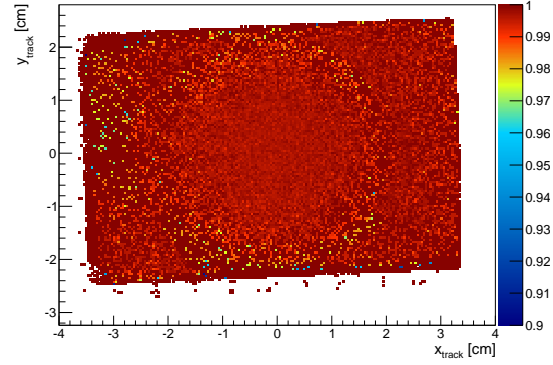
Figure A.9: Performance plots for SI03V.

Appendix A Performance Plots and Histograms

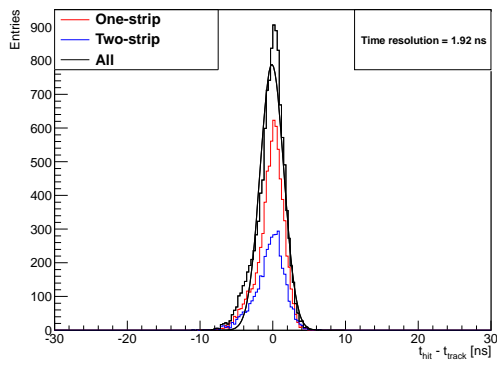
SI03X



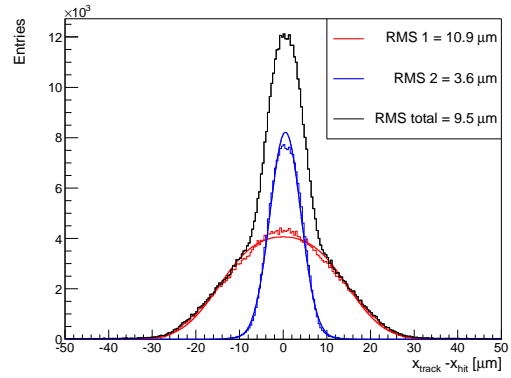
(a) Cluster amplitude



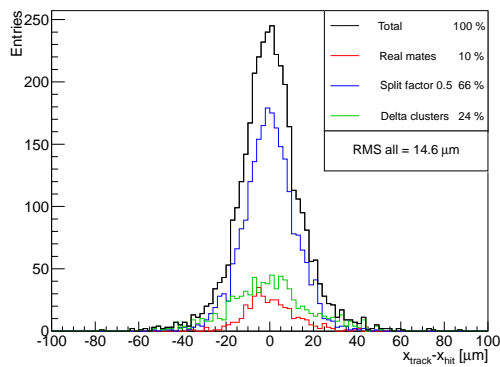
(b) Efficiency



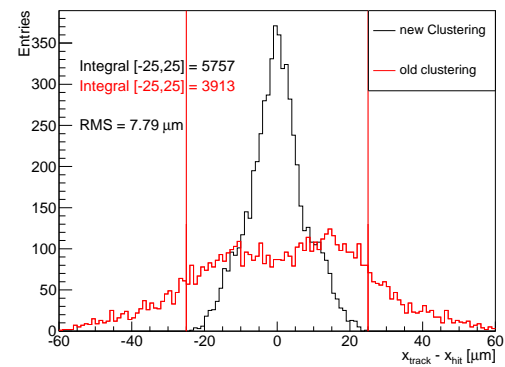
(c) Time Residual



(d) Spatial Residual



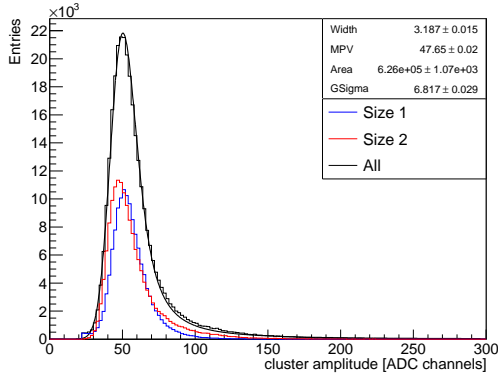
(e) Mate Clustering



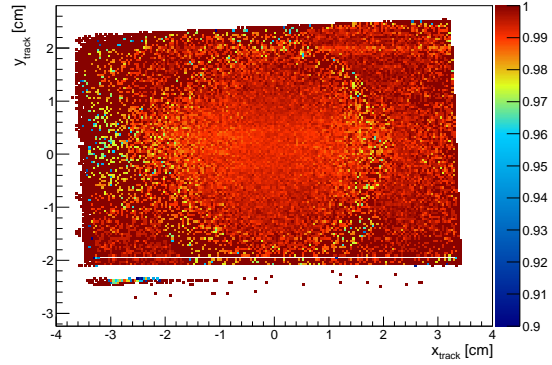
(f) Misidentified double-strip clusters

Figure A.10: Performance plots for SI03X.

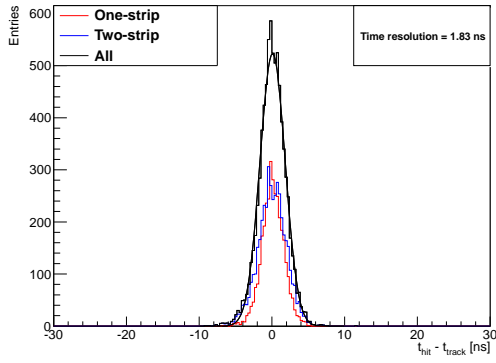
SI03Y



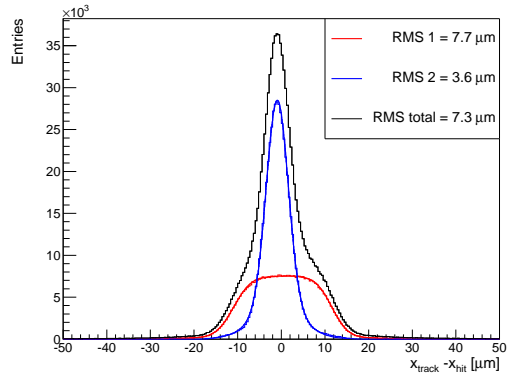
(a) Cluster amplitude



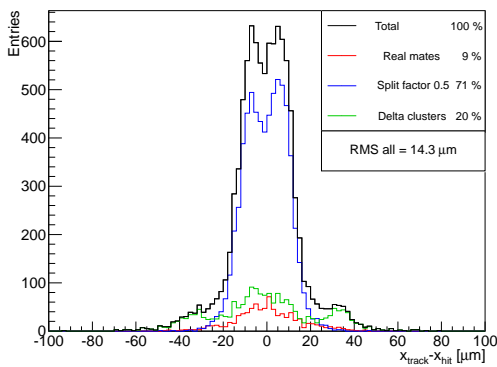
(b) Efficiency



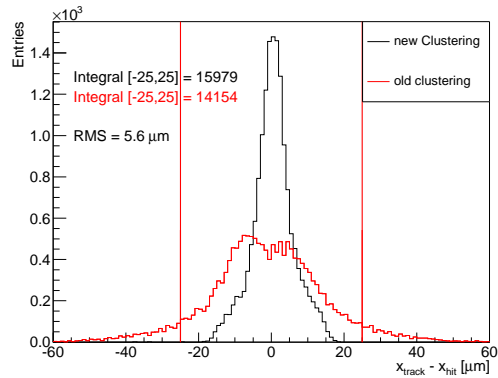
(c) Time Residual



(d) Spatial Residual



(e) Mate Clustering

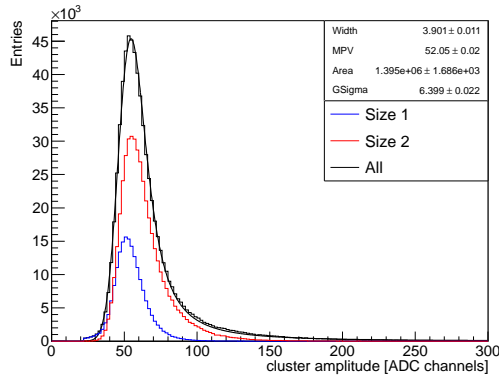


(f) Misidentified double-strip clusters

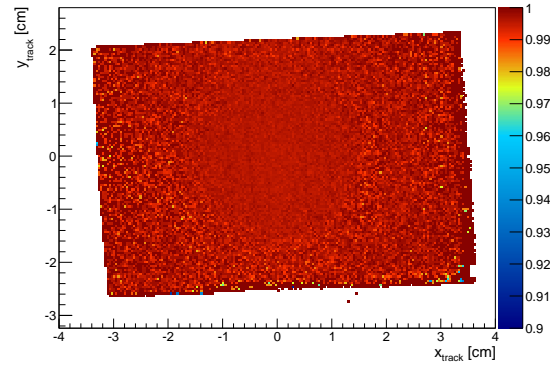
Figure A.11: Performance plots for SI03Y.

Appendix A Performance Plots and Histograms

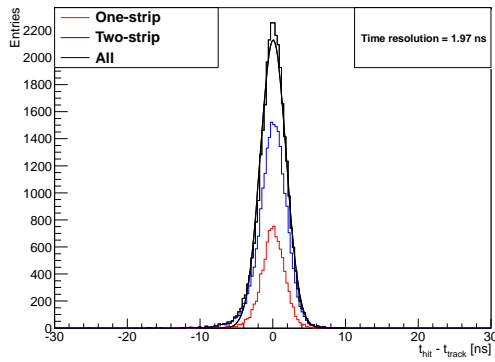
SI04U



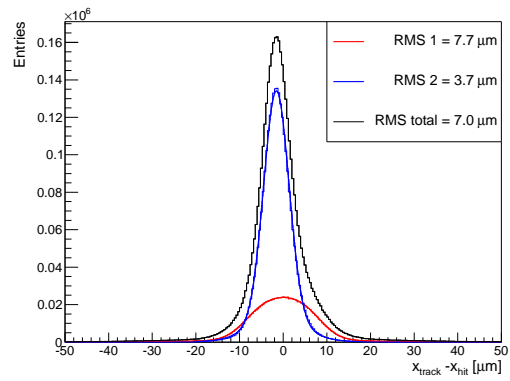
(a) Cluster amplitude



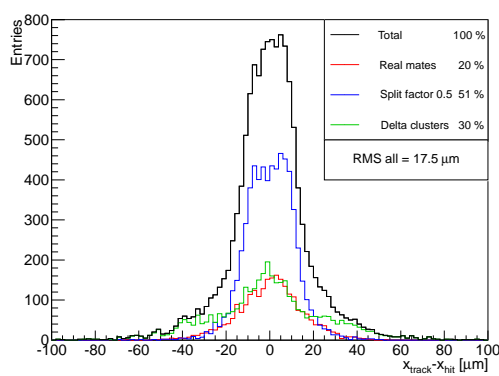
(b) Efficiency



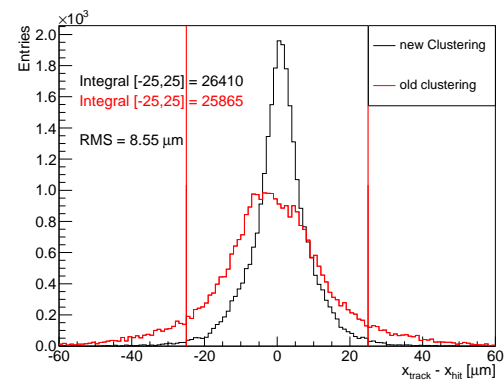
(c) Time Residual



(d) Spatial Residual



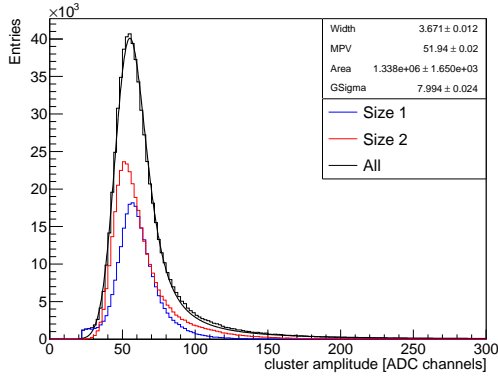
(e) Mate Clustering



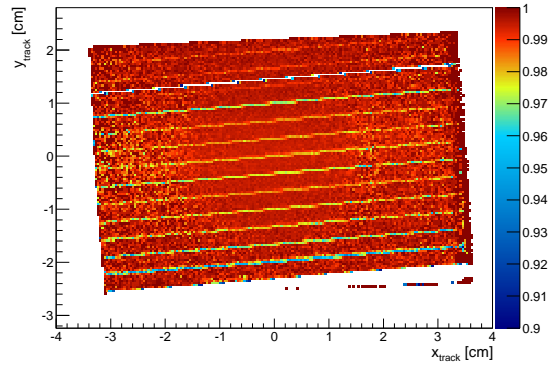
(f) Misidentified double-strip clusters

Figure A.12: Performance plots for SI04U.

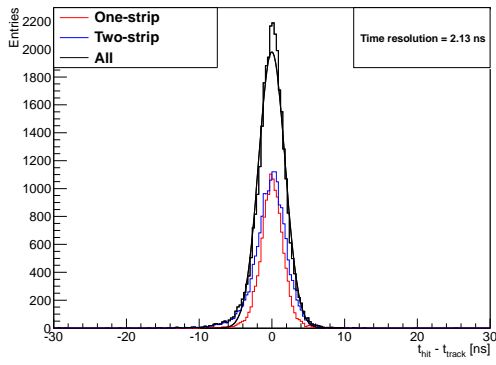
SI04V



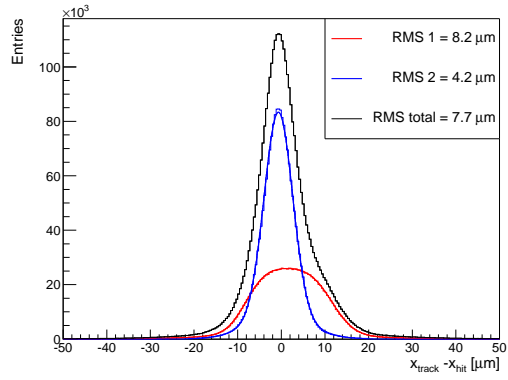
(a) Cluster amplitude



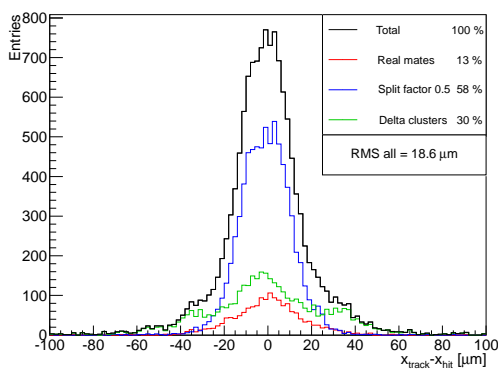
(b) Efficiency



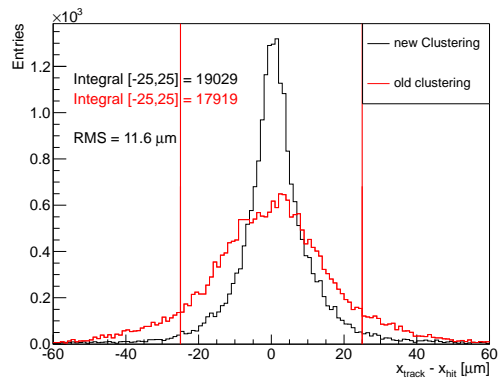
(c) Time Residual



(d) Spatial Residual



(e) Mate Clustering

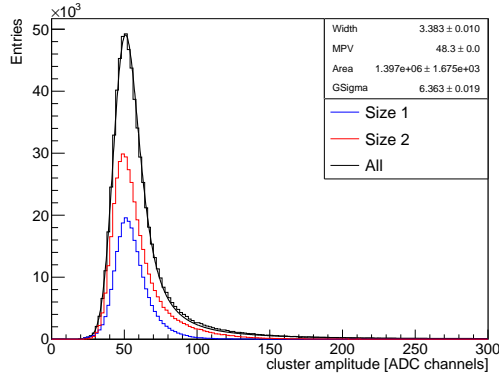


(f) Misidentified double-strip clusters

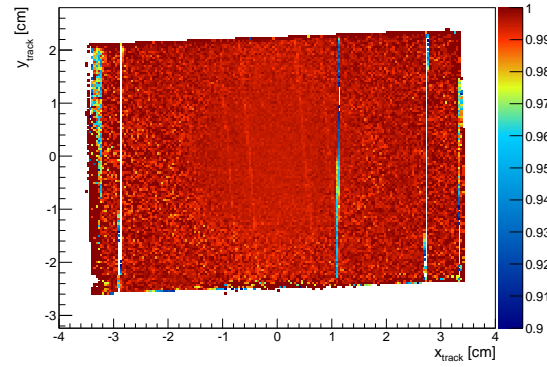
Figure A.13: Performance plots for SI04V.

Appendix A Performance Plots and Histograms

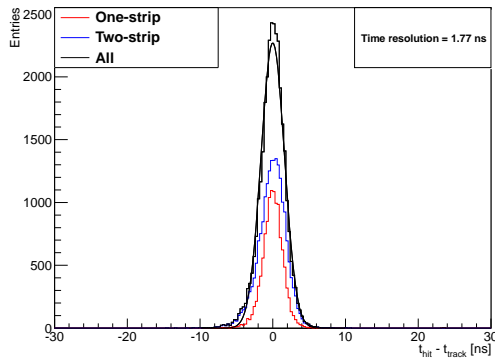
SI04X



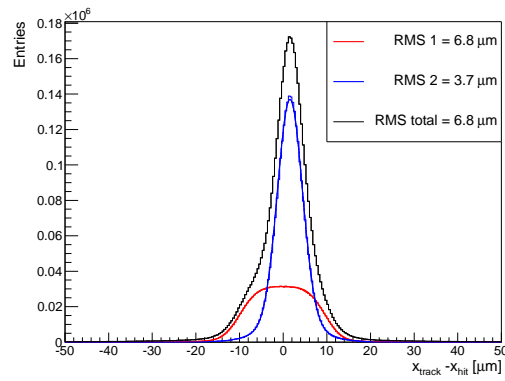
(a) Cluster amplitude



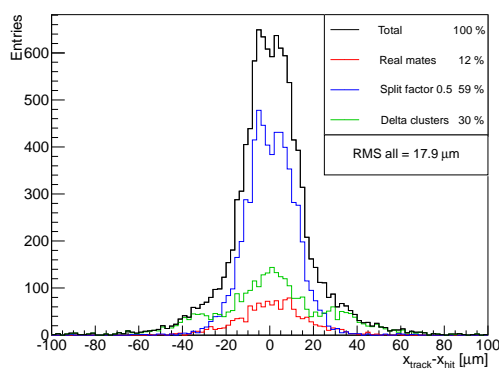
(b) Efficiency



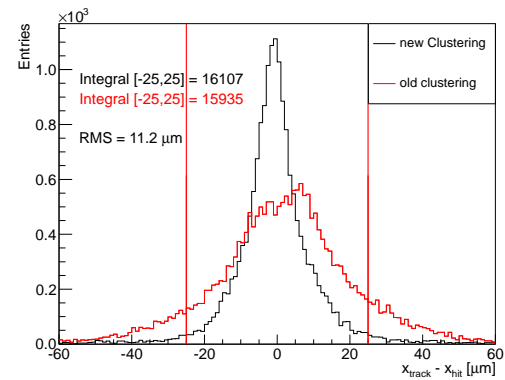
(c) Time Residual



(d) Spatial Residual



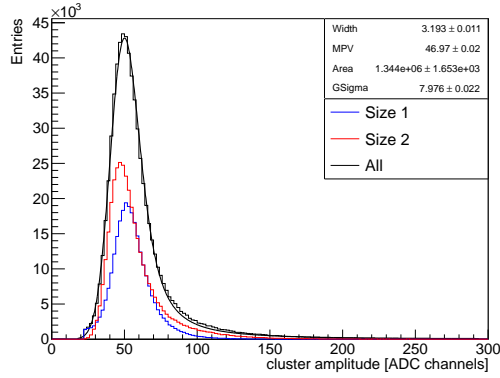
(e) Mate Clustering



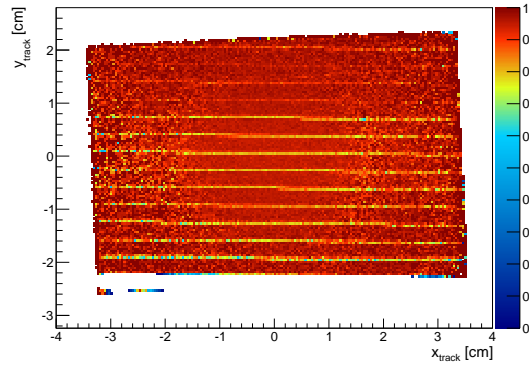
(f) Misidentified double-strip clusters

Figure A.14: Performance plots for SI04X.

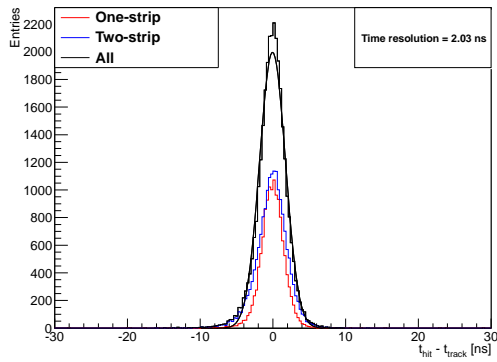
SI04Y



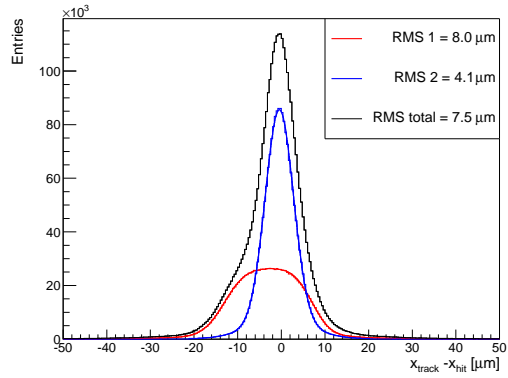
(a) Cluster amplitude



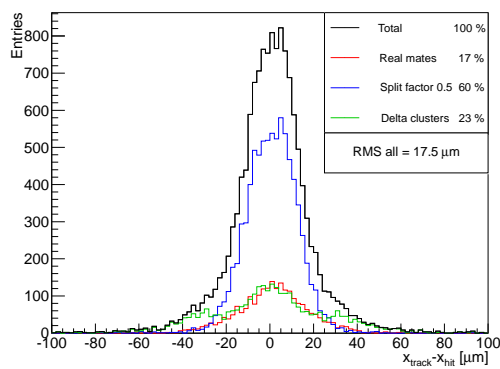
(b) Efficiency



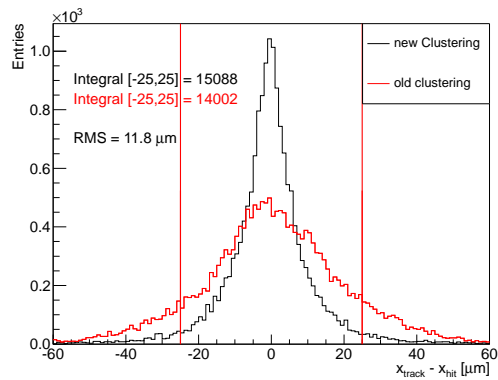
(c) Time Residual



(d) Spatial Residual



(e) Mate Clustering

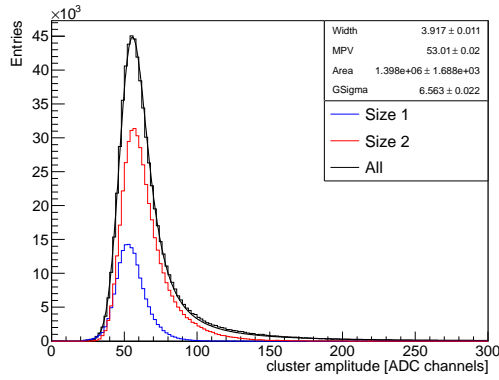


(f) Misidentified double-strip clusters

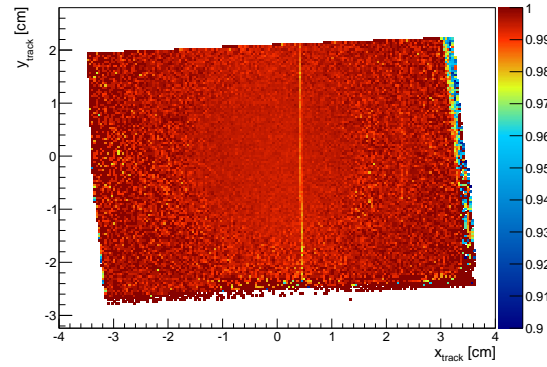
Figure A.15: Performance plots for SI04Y.

Appendix A Performance Plots and Histograms

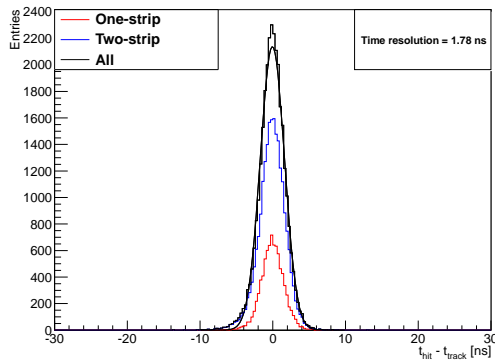
SI05U



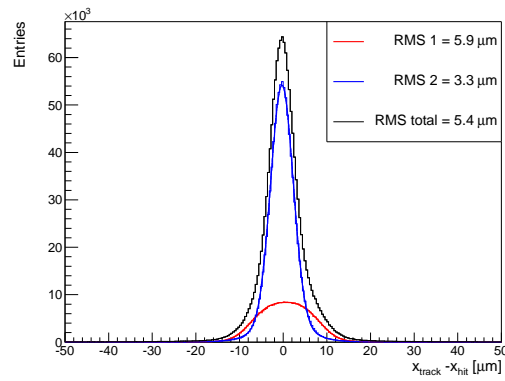
(a) Cluster amplitude



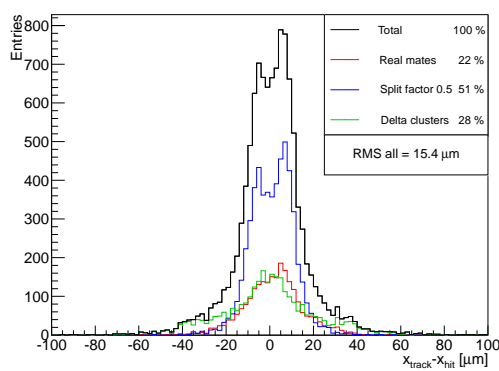
(b) Efficiency



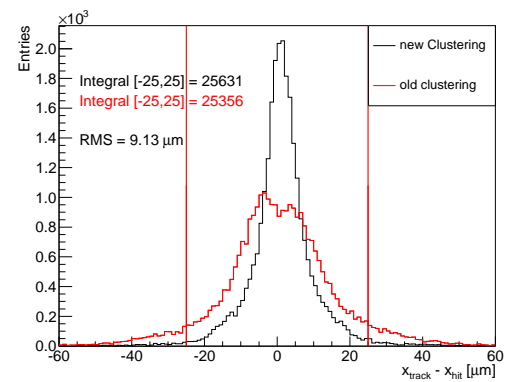
(c) Time Residual



(d) Spatial Residual



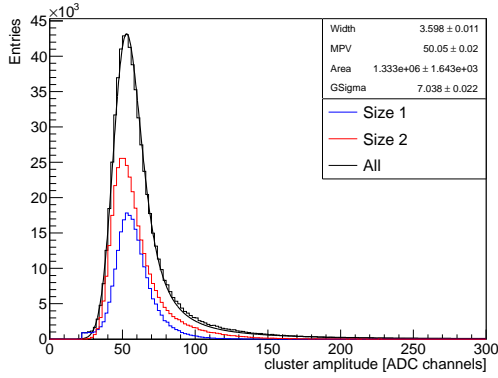
(e) Mate Clustering



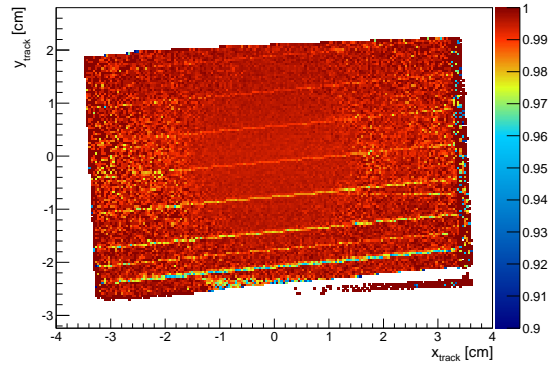
(f) Misidentified double-strip clusters

Figure A.16: Performance plots for SI05U.

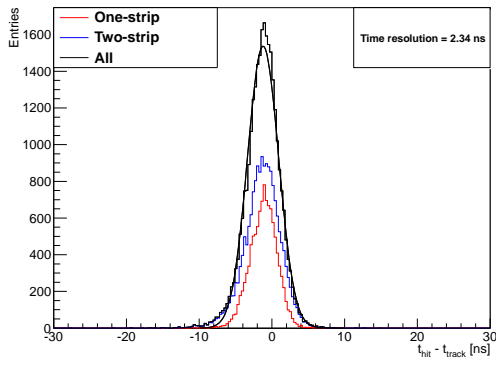
SI05V



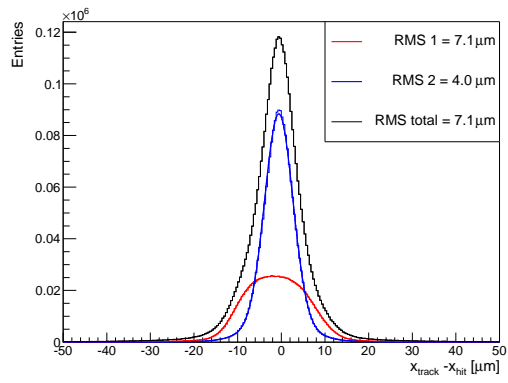
(a) Cluster amplitude



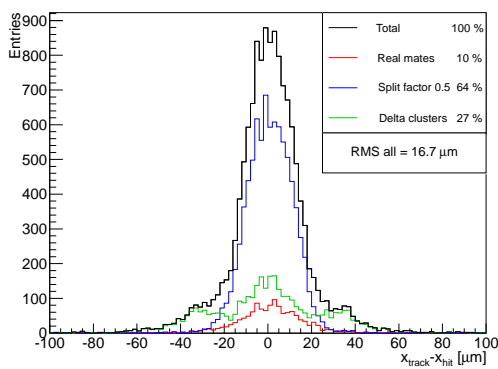
(b) Efficiency



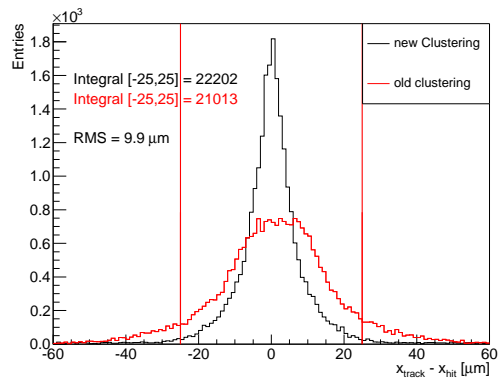
(c) Time Residual



(d) Spatial Residual



(e) Mate Clustering

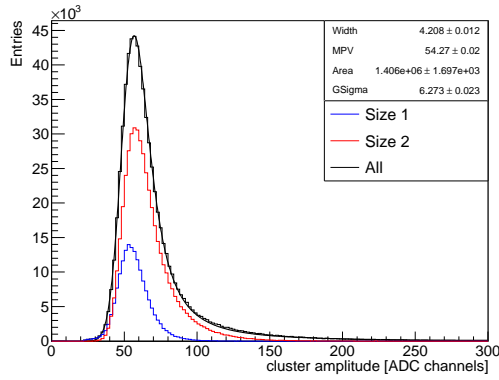


(f) Misidentified double-strip clusters

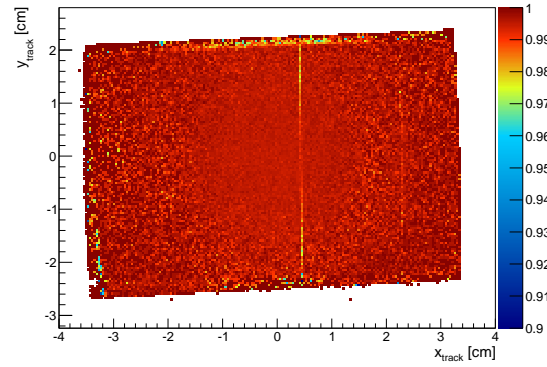
Figure A.17: Performance plots for SI05V.

Appendix A Performance Plots and Histograms

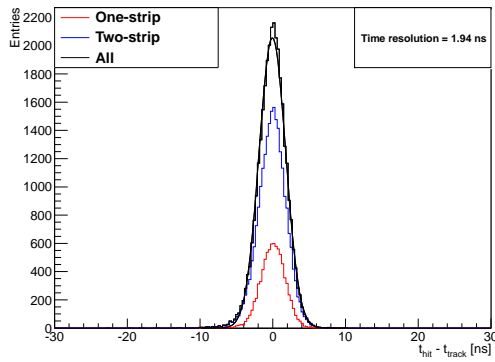
SI05X



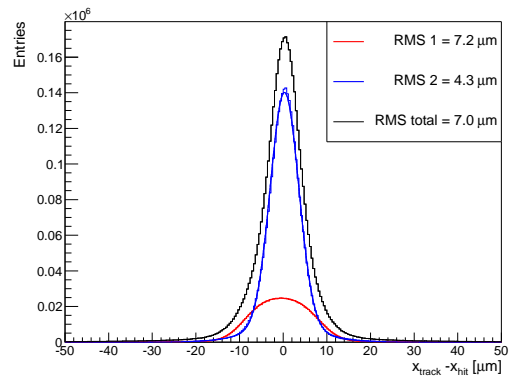
(a) Cluster amplitude



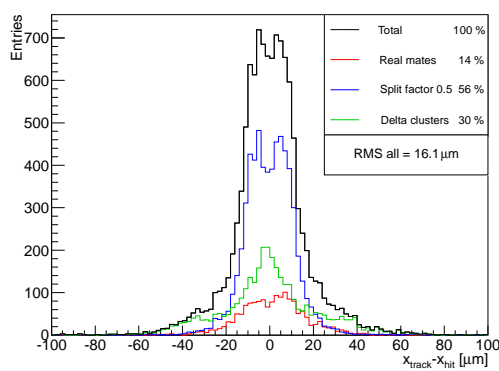
(b) Efficiency



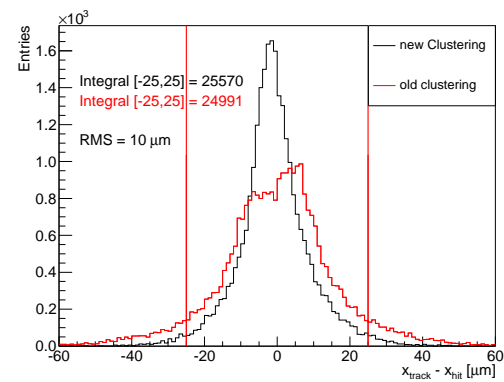
(c) Time Residual



(d) Spatial Residual



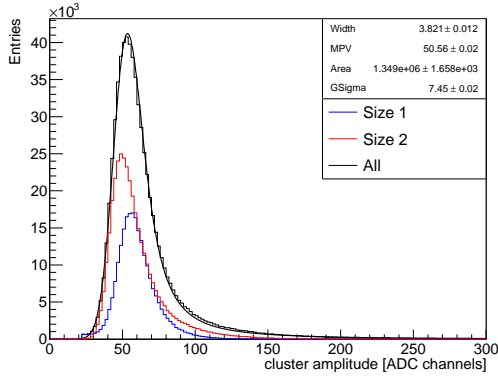
(e) Mate Clustering



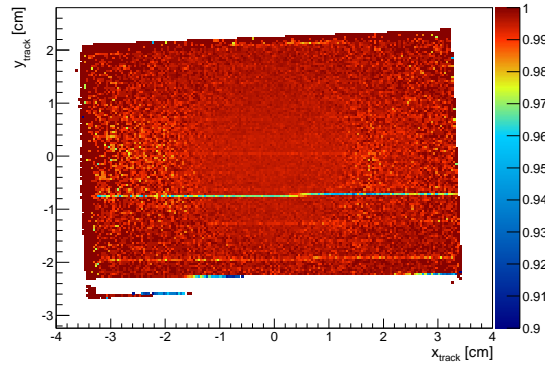
(f) Misidentified double-strip clusters

Figure A.18: Performance plots for SI05X.

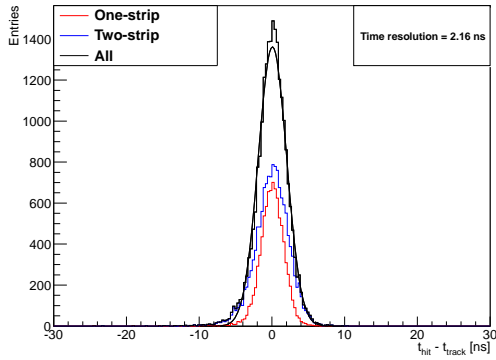
SI05Y



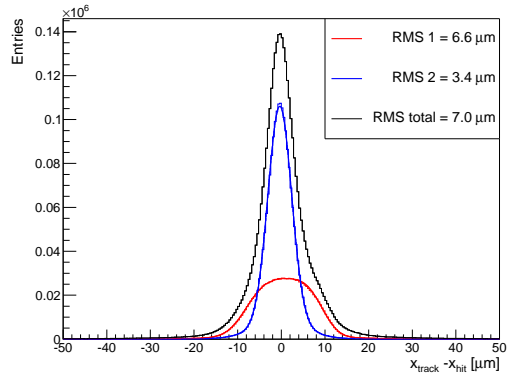
(a) Cluster amplitude



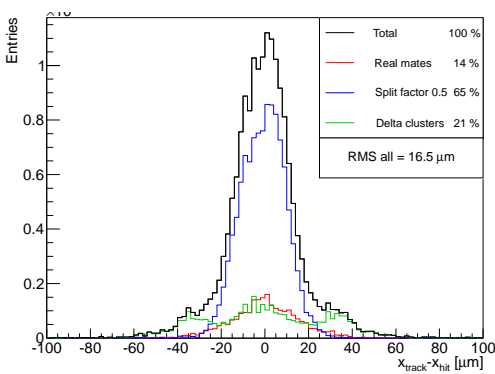
(b) Efficiency



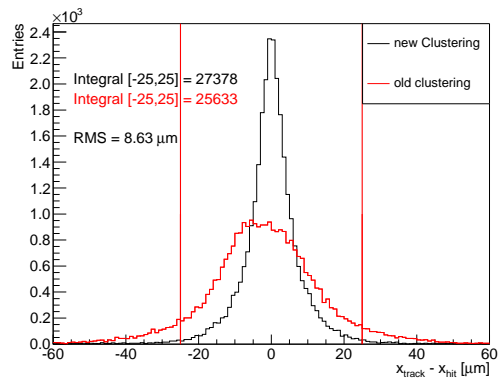
(c) Time Residual



(d) Spatial Residual



(e) Mate Clustering



(f) Misidentified double-strip clusters

Figure A.19: Performance plots for SI05Y.

Appendix B

Plots for Alignment Studies

B.1 Micromegas Pitch

The alignment studies presented in Section 4.3.2 were done using a modified CORAL options file. All changes are given with respect to the standard Primakoff 2009 options file `trafdic.2009.primakoff.opt`. Basically all tracking detectors behind the target are switched off during the tracking, leaving only SI04 and SI05 inside the conical cryostat. Therefore the parameters of the pattern recognition have to be adjusted.

Table B.1: CORAL options for tracking with SI04 and SI05 only.

Option	Explanation
TraF iPRpar [0 - 5] 2 3 8 2 2 8	Reduces the minimum number of clusters required to reconstruct a track in the zone between target and SM1.
TraF ReMode [26] 0	Bridging over the target is off.
TraF DetNameOff MM DC FI GEM GP MP	Deactivates the other tracking detectors.
mDST hits SI MM DC FI GEM GP MP	The clusters of the specified detectors are written to the MDST file.
TraF dCut [84] .00	Sets the silicon route enlargement to zero.
TraF dCut [85] .00	Sets the silicon cluster position uncertainty to zero.
TraF ReMode [17] 0	GEM amplitude correlation is disabled. This is obligatory if any GEM is among the switched off detectors.
TraF iPRpar [90] 0	Minimum number of hits for forward tracks.

Appendix B Plots for Alignment Studies

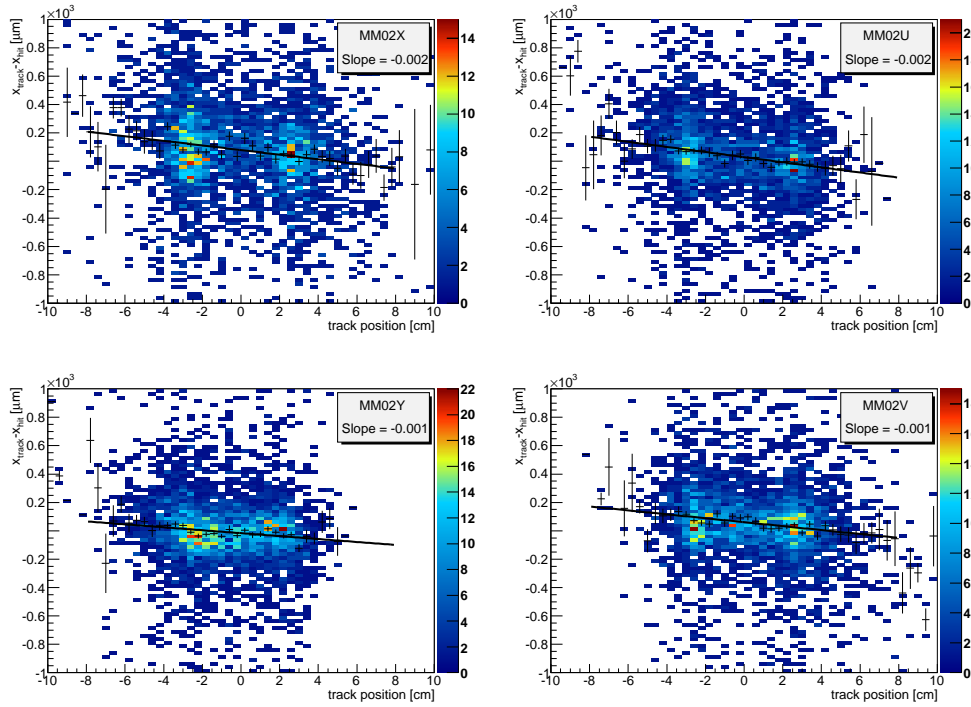


Figure B.1: Residual versus track position measured in WRS for the four planes of MM02.

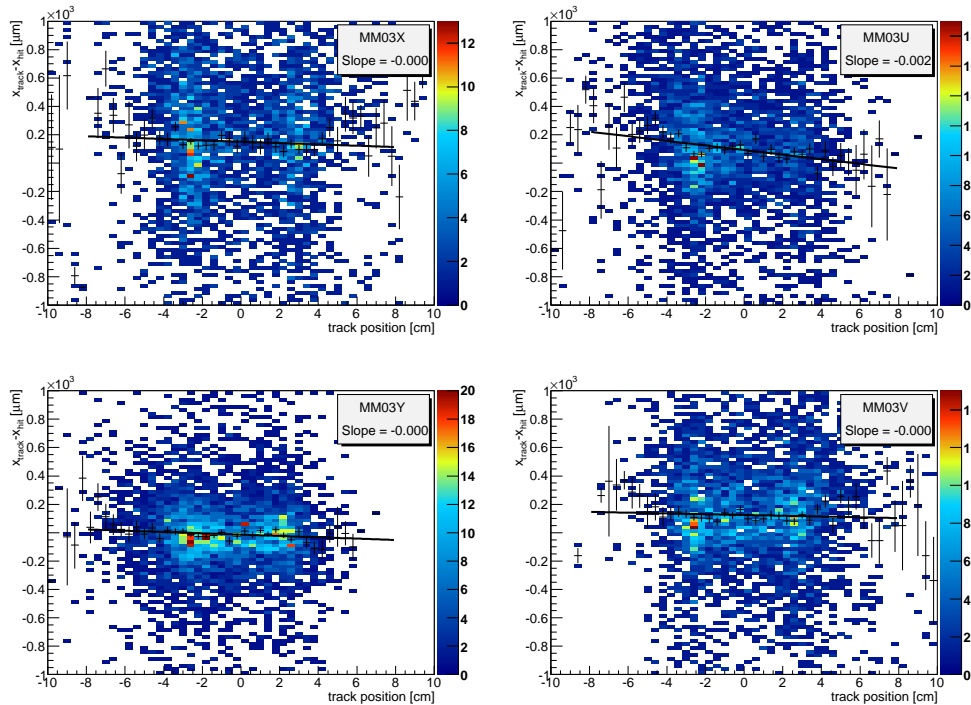


Figure B.2: Residual versus track position measured in WRS for the four planes of MM03.

B.2 Used Productions

The paths can be accessed from every CERN machine. In both cases the complete run 81819 was used.

Test production:

`/castor/cern.ch/user/n/na58dst2/ECAL/81819-bridge/mDST.chunks/`

T38:

`/castor/cern.ch/user/n/na58dst1/generalprod/testcoral/hadron2009t38/megaDST.chunks/`

B.3 Silicon Residuals

Residuals of all silicon stations for three runs during the Primakoff data taking period 2009 were extracted. The approach is described in Section 4.3.1. The plots are grouped according to the measured coordinate. The planes U together with X and V together with Y are shown on one double page each. Therein the left page shows the respective silicon planes upstream of the target, i.e. the beam telescope, whereas the right side shows the ones downstream of the target.

To obtain this residuals special CORAL options were used. All changes are given with respect to the standard Primakoff 2009 options file `trafdic.2009.primakoff.opt`.

Table B.2: CORAL options for straight line tracking through all silicon stations.

Option	Explanation
<code>define zone 350 3500 before M1</code>	Changes the zone definition to allow a tracking using silicons only.
<code>define zone -8000 350 before the target</code>	
<code>TraF ReMode [26] 0</code>	Bridging over the target is off, i.e. the silicon only tracks are not bridged into the next zone.
<code>TraF DetNameOff TBName</code>	Deactivates the detector <code>TBName</code> during the tracking. The technical board name has to be given, e.g <code>SI01U</code> or <code>SI</code> , where the latter option would deactivate all silicons.
<code>mDST hits SI</code>	Writes silicon clusters to the output. Needed to calculate the residuals in PHAST.
<code>TraF ReMode [44] 0</code>	Disable silicon ambiguities.
Optional, depending on alignment quality	
<code>TraF dCut [84] .00</code>	Sets the silicon route enlargement to zero.
<code>TraF dCut [85] .00</code>	Sets the silicon cluster position uncertainty to zero.

Run 81971, X-like

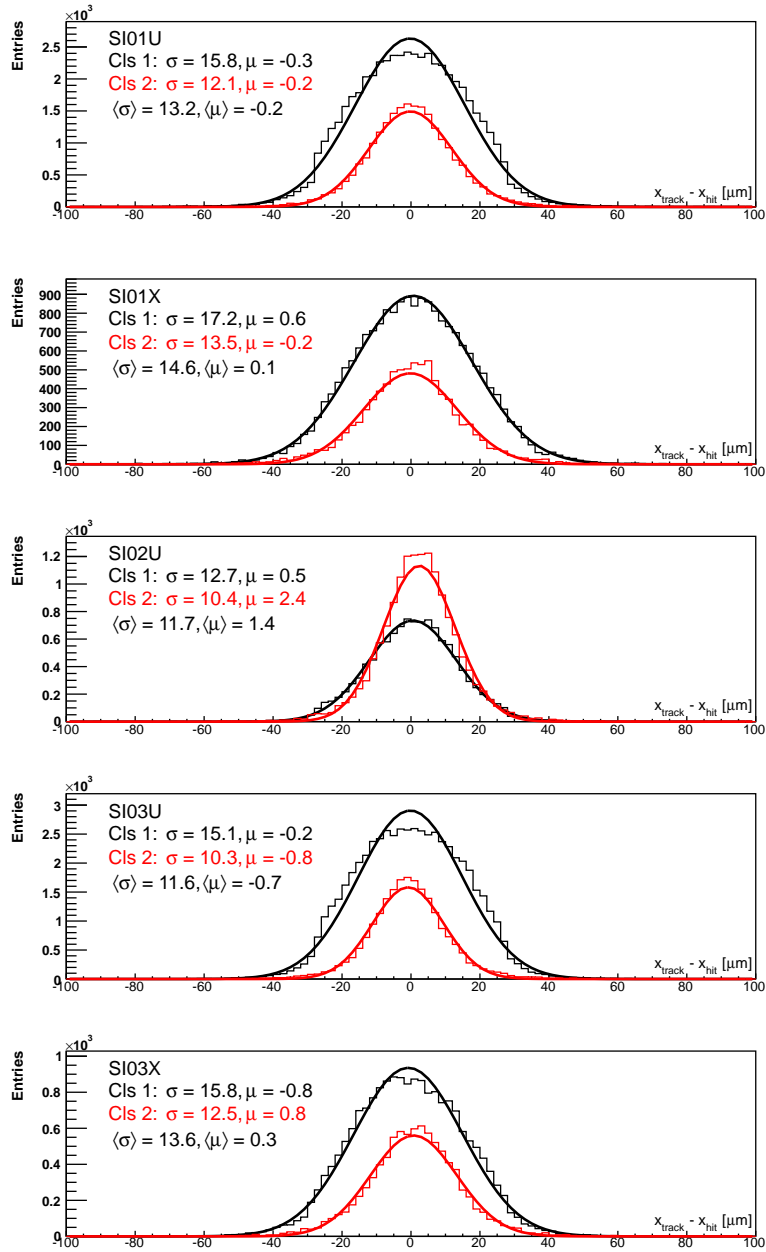


Figure B.3: Residuals for X-like detectors placed in the beam telescope, run 81971.

Appendix B Plots for Alignment Studies

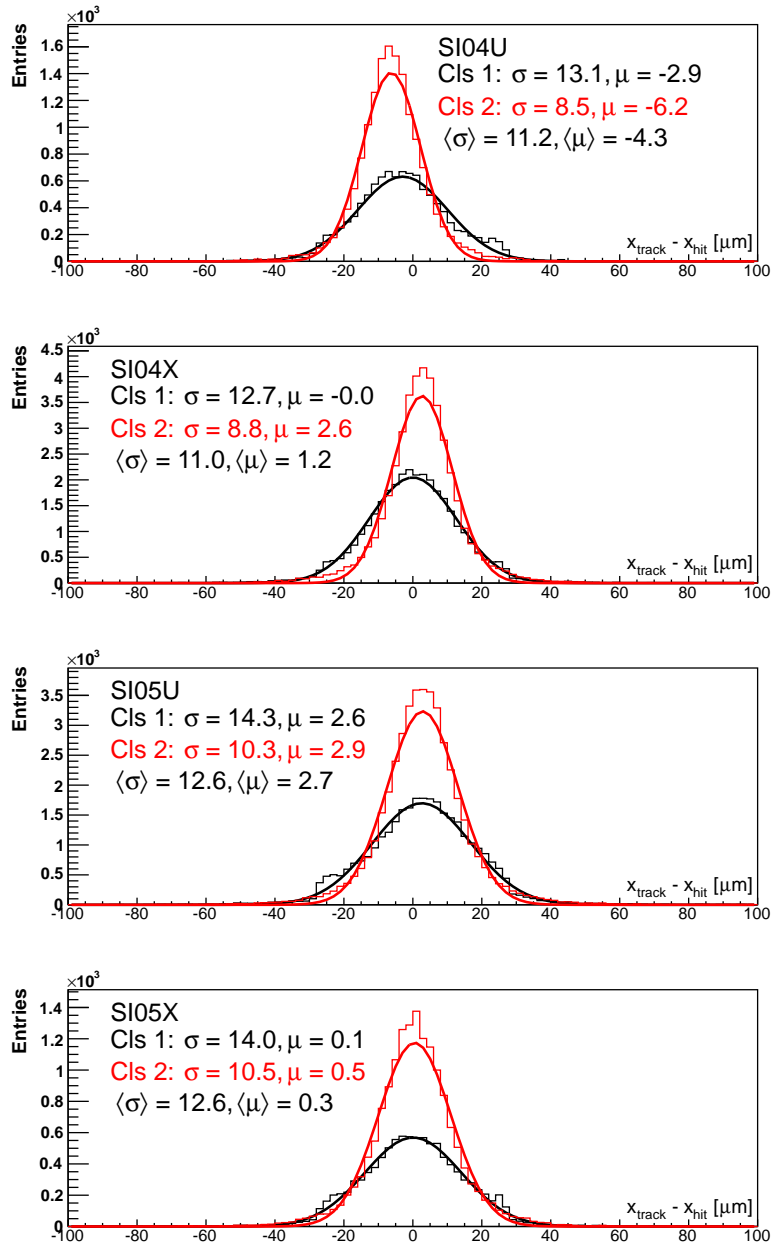


Figure B.4: Residuals for X-like detectors downstream of the target, run 81971.

Run 81971, Y-like

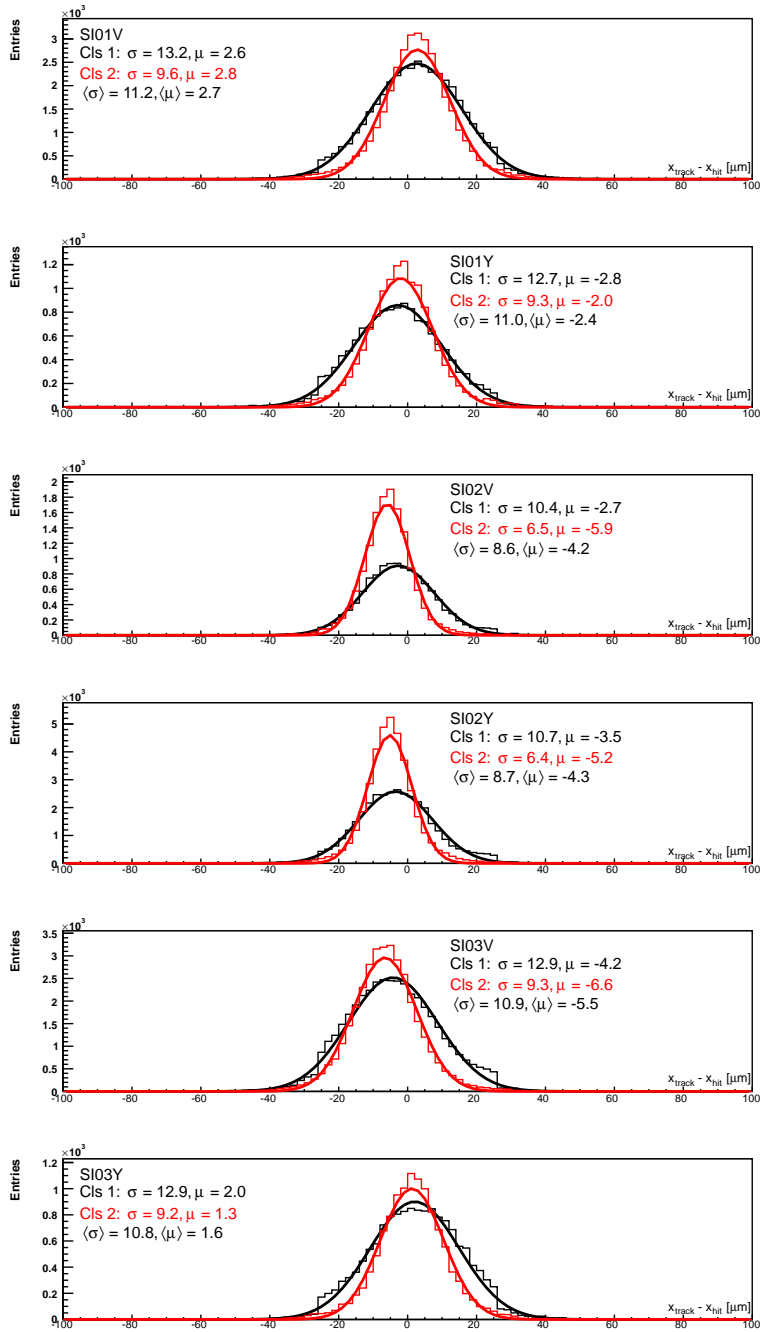


Figure B.5: Residuals for Y-like detectors placed in the beam telescope, run 81971.

Appendix B Plots for Alignment Studies

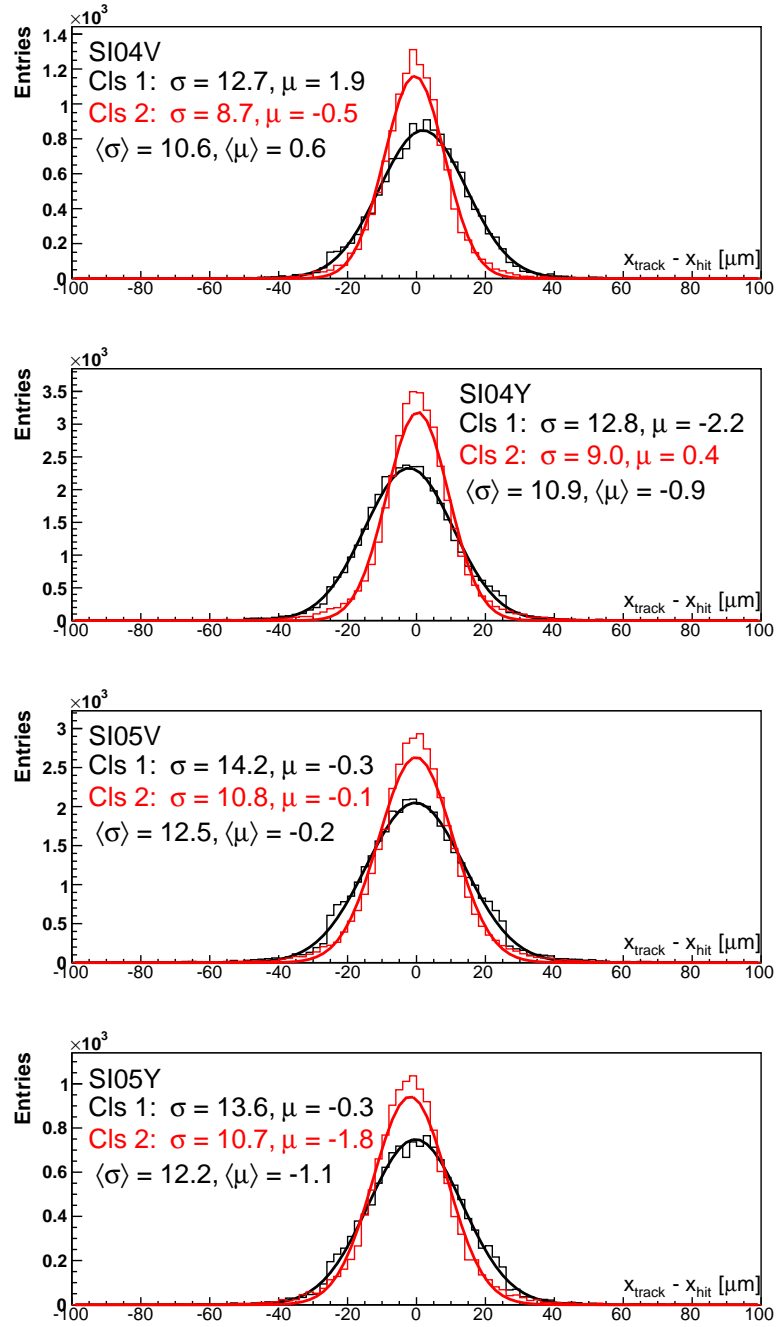


Figure B.6: Residuals for Y-like detectors downstream of the target, run 81971.

Run 82006, X-like

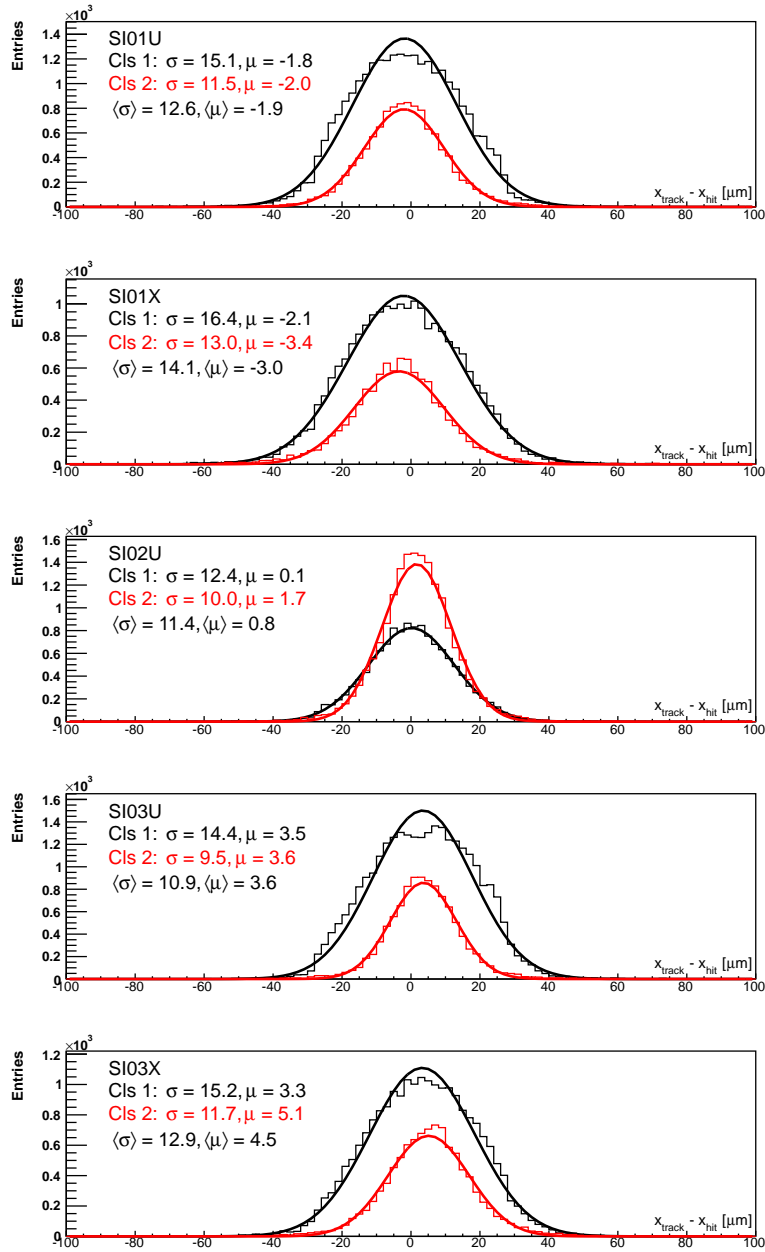


Figure B.7: Residuals for X-like detectors placed in the beam telescope, run 82006.

Appendix B Plots for Alignment Studies

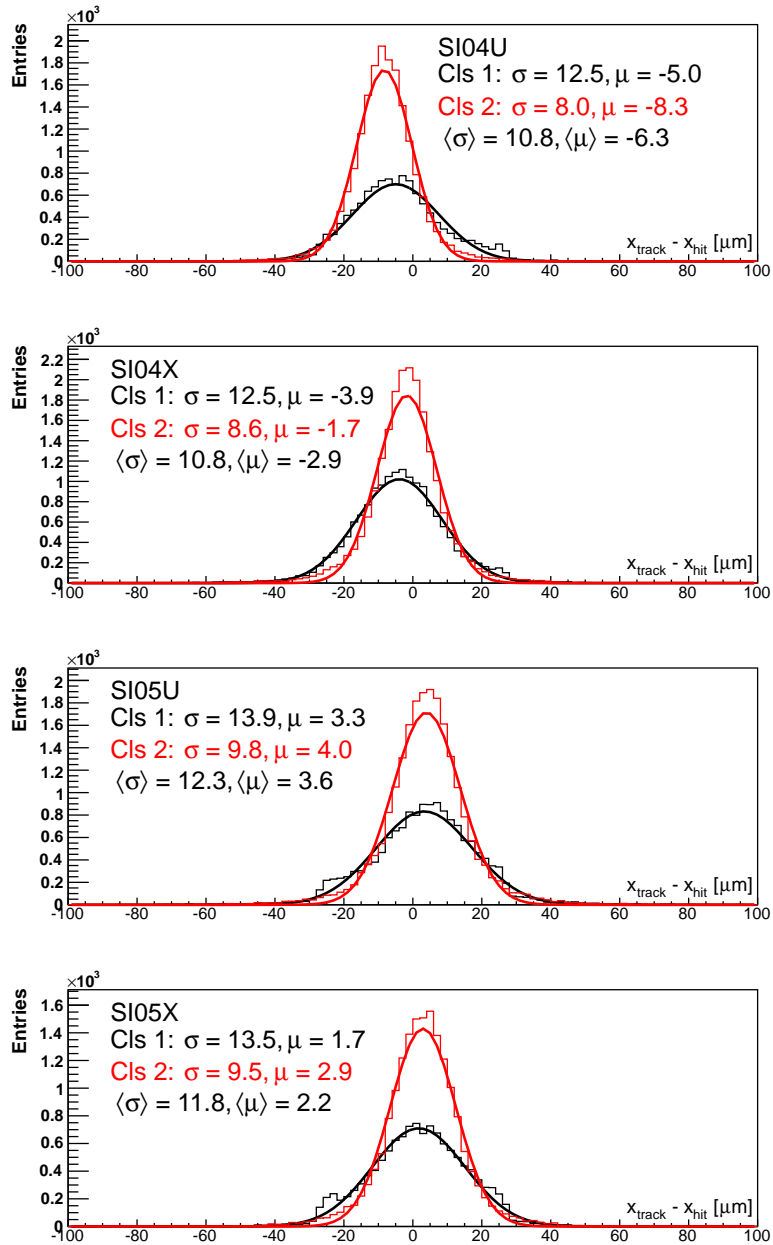


Figure B.8: Residuals for X-like detectors downstream of the target, run 82006.

Run 82006, Y-like

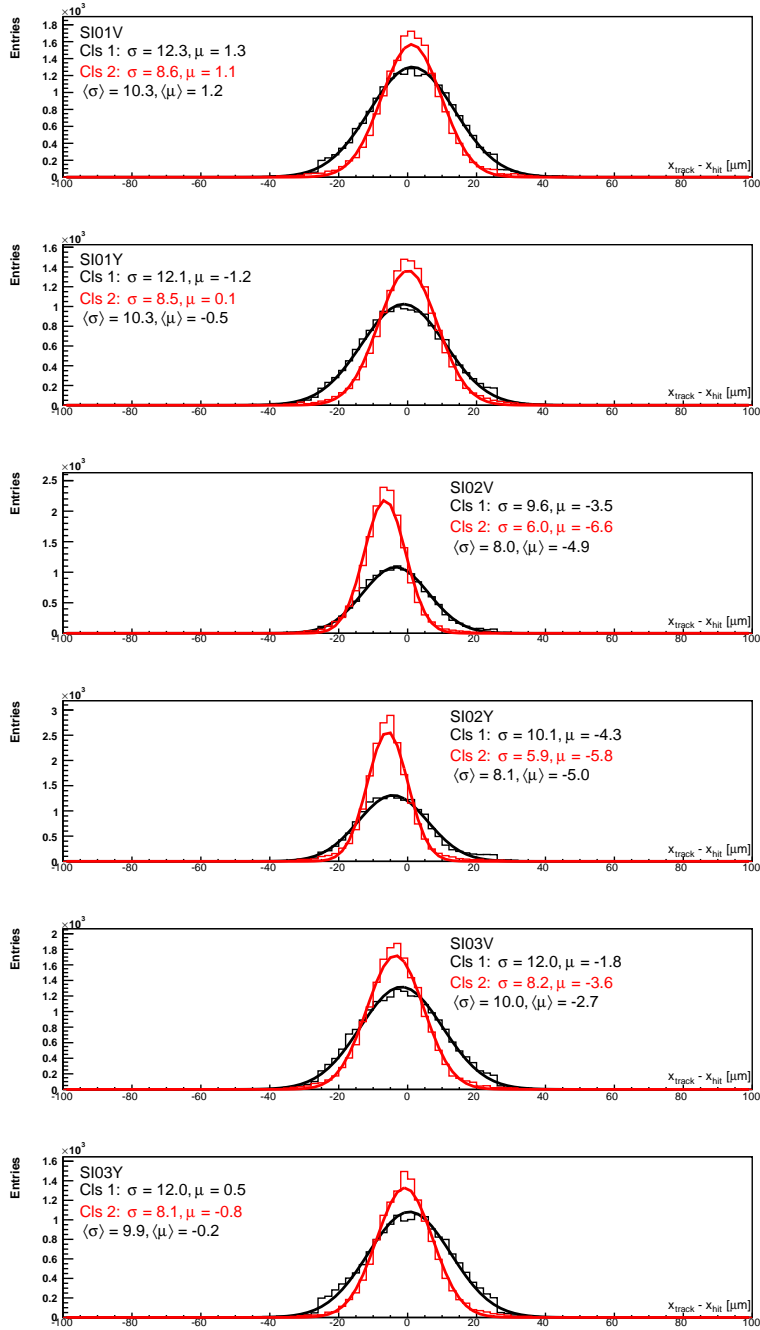


Figure B.9: Residuals for Y-like detectors placed in the beam telescope, run 82006.

Appendix B Plots for Alignment Studies

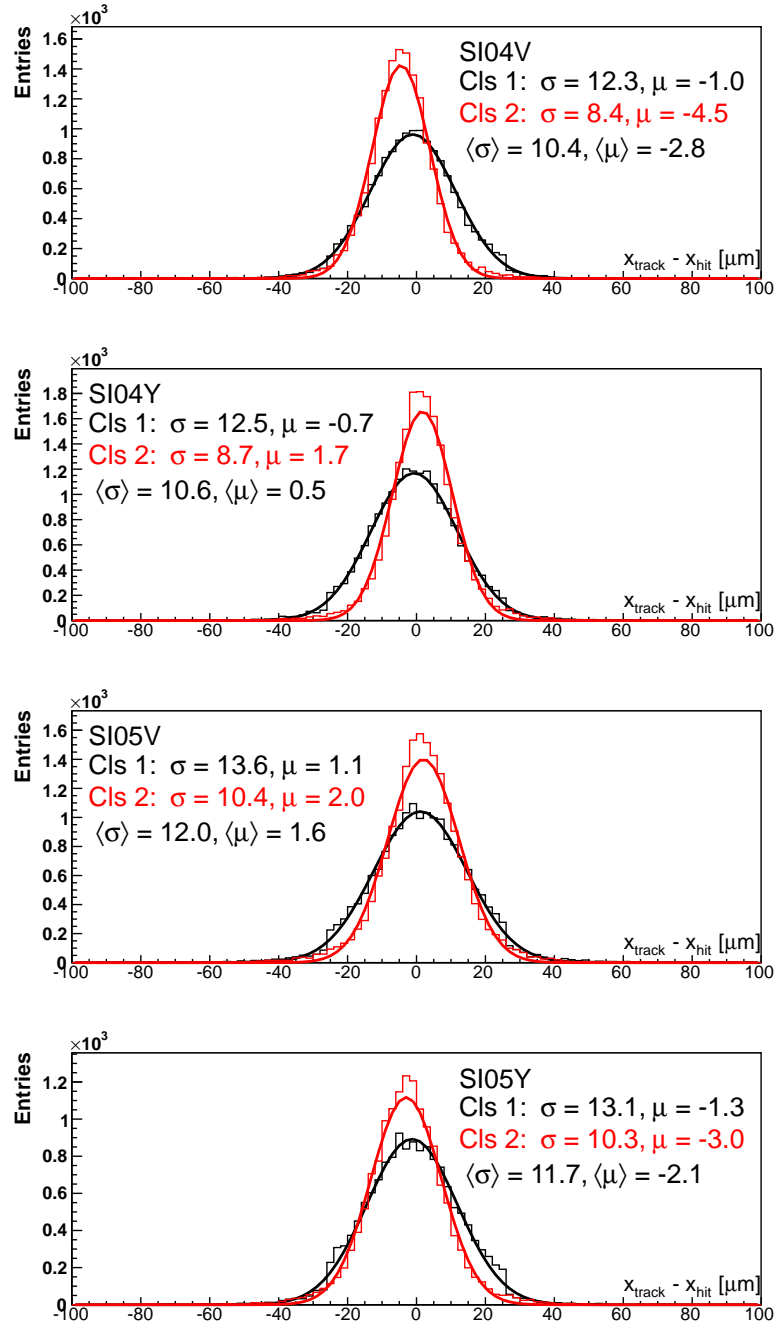


Figure B.10: Residuals for Y-like detectors downstream of the target, run 82006.

Run 82144, X-like

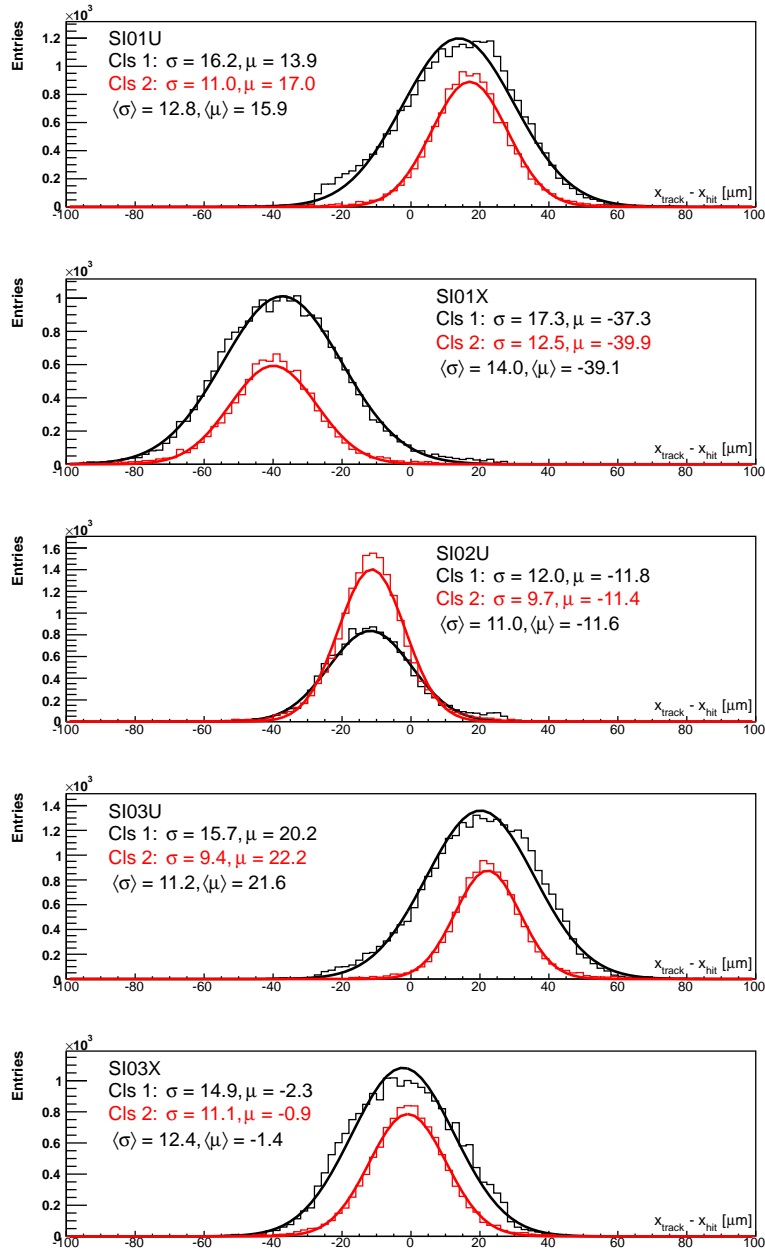


Figure B.11: Residuals for X-like detectors placed in the beam telescope, run 82144.

Appendix B Plots for Alignment Studies

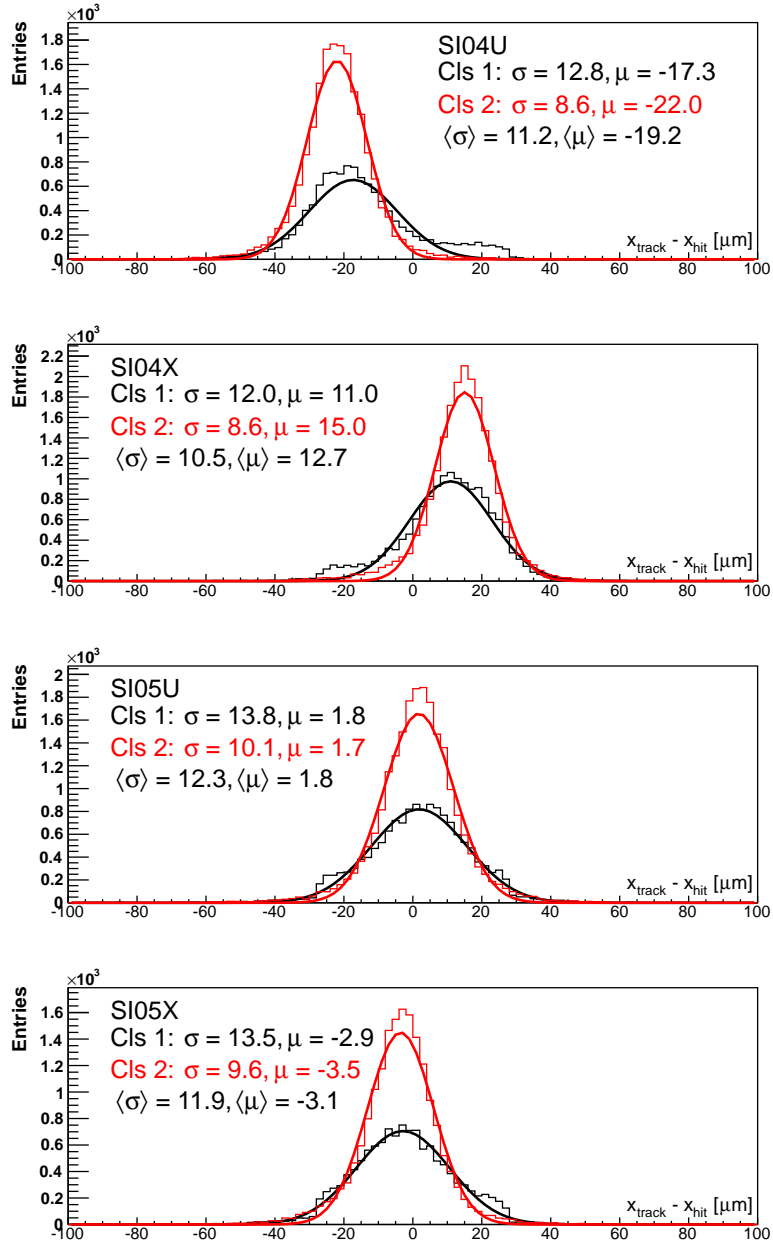


Figure B.12: Residuals for X-like detectors downstream of the target, run 82144.

Run 82144, Y-like

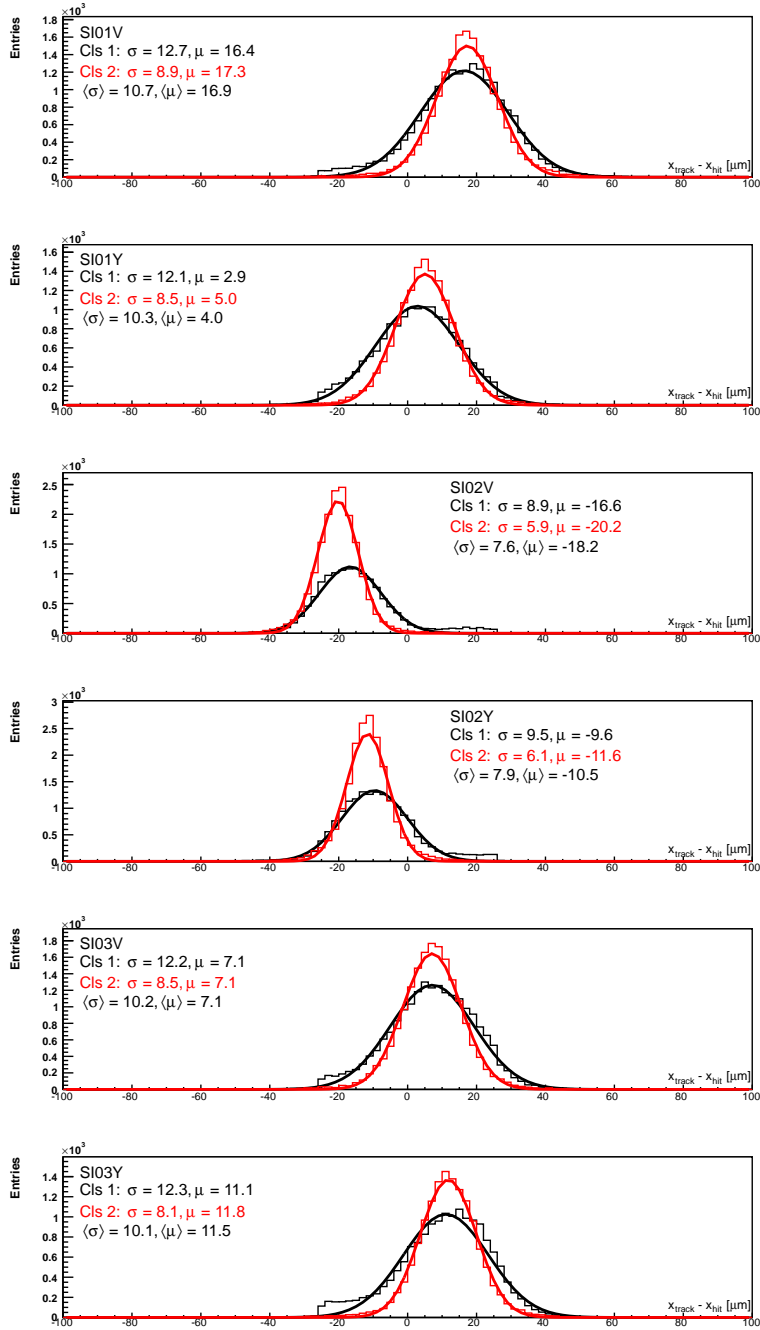


Figure B.13: Residuals for Y-like detectors placed in the beam telescope, run 82144.

Appendix B Plots for Alignment Studies

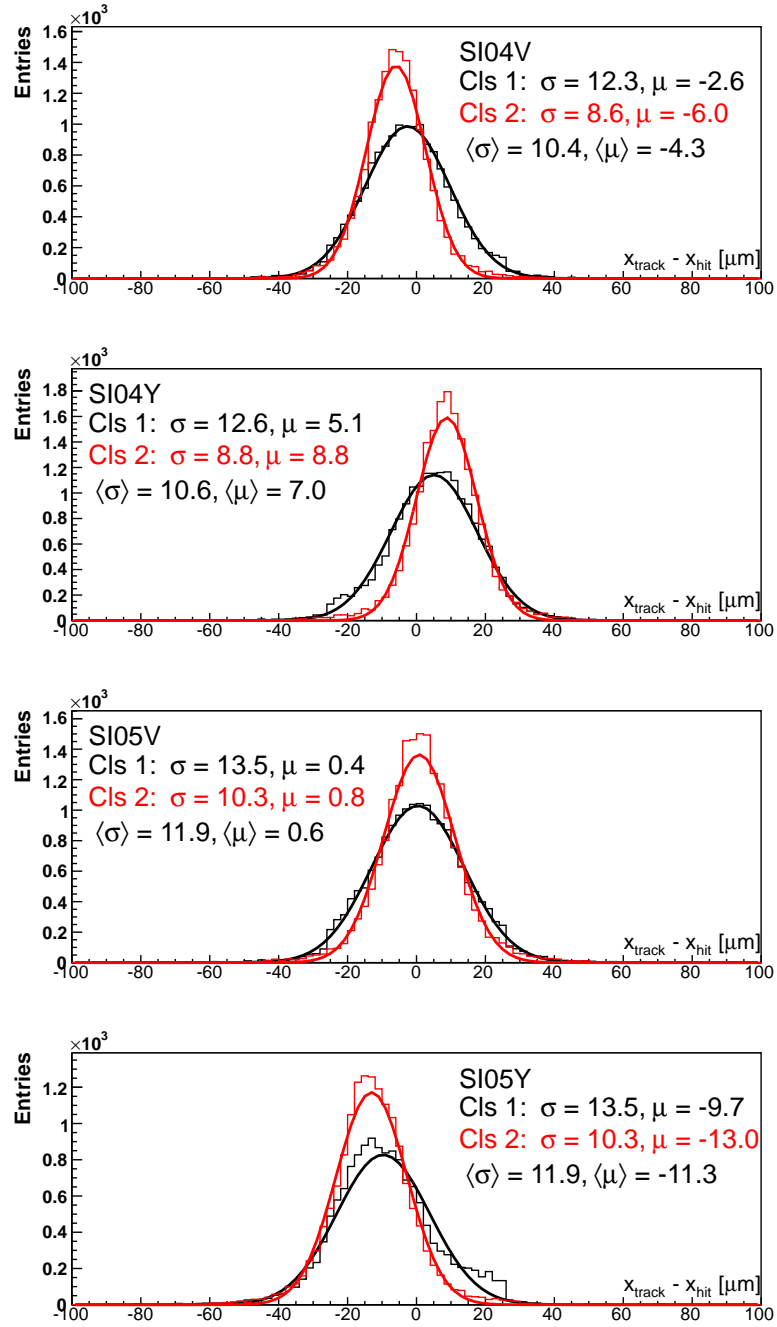


Figure B.14: Residuals for Y-like detectors downstream of the target, run 82144.

Bibliography

- [1] Coral website. <http://coral.web.cern.ch/coral/RefGuideCVS/html/>.
- [2] P. Abbon et al. The COMPASS experiment at CERN. *Nuclear Instruments and Methods in Physics Research A*, 577:455–518, 2007.
- [3] P. Abbon et al. The COMPASS setup for physics with hadron beam. To be published.
- [4] A. Abragam and M. Goldman. Principles of dynamic nuclear polarisation. *Rep. Prog. Phys.*, 41:395–467, 1978.
- [5] I. Abt et al. Double-sided microstrip detectors for the high radiation environment in the HERA-B experiment. *Nuclear Instruments and Methods in Physics Research A*, 439:442–450, 2000.
- [6] M. G. Alekseev et al. Observation of a $J^{PC} = 1^{-+}$ exotic resonance in diffractive dissociation of $190 \text{ GeV}/c \pi^{-}$ into $\pi^{-}\pi^{-}\pi^{+}$. *Phys. Rev. Lett.*, 104(24):241803, June 2010.
- [7] A. Austregesilo, 2011. Private communication.
- [8] Y. Bedfer, 2011. Private communication.
- [9] Y. Bedfer, S. Gerassimov, A. Korzenev, and R. Windmolders. COMPASS’s track reconstruction algorithm. COMPASS Note 2004-1, April 2005.
- [10] Bethe, H. Zur Theorie des Durchgangs schneller Korpuskularstrahlen durch Materie. *Annalen der Physik*, 397(3):325–400, 1930.
- [11] H. Bichsel. Straggling in thin silicon detectors. *Rev. Mod. Phys.*, 60:663–699, Jul 1988.
- [12] K. Bicker. *Construction and Commissioning of a Cooling and Support Structure for the Silicon Detectors for the COMPASS Experiment*. Diploma thesis, Technische Universität München, January 2011.
- [13] A. Bischoff, N. Findeis, D. Hauff, P. Holl, J. Kemmer, P. Klein, P. Lechner, G. Lutz, R. Richter, and L. Strüder. Breakdown protection and long-term stabilisation for si-detectors. *Nuclear Instruments and Methods in Physics Research Section A: Accelerators, Spectrometers, Detectors and Associated Equipment*, 326(1-2):27 – 37, 1993.

Bibliography

- [14] V. Blobel. *Linear Least Square Fits with a Large Number of Parameters*. DESY. <http://www.desy.de/~blobel/millepede1.ps>.
- [15] K. Borer et al. Charge collection efficiency of irradiated silicon detector operated at cryogenic temperatures. *Nuclear Instruments and Methods in Physics Research A*, 430:5–16, 2000.
- [16] R. Brun, F. Rademakers, et al. ROOT TH2D::ProfileX(). <http://root.cern.ch/root/html530/TH2.html#TH2:ProfileX>.
- [17] R. Brun, F. Rademakers, et al. ROOT Tutorials: Fitting functions. <http://root.cern.ch/root/html/tutorials/fit/langaus.C.html>.
- [18] R. Brun, F. Rademakers, et al. ROOT website. <http://root.cern.ch>.
- [19] CEA/Saclay. Anibus. http://irfu.cea.fr/Phocea/Vie_des_labos/Ast/ast_visu.php?id_ast=2117.
- [20] CERN. CERN accelerator complex. <http://cdsweb.cern.ch/record/1260465>.
- [21] CERN website. www.cern.ch.
- [22] Geant: Detector description and simulation tool. <http://wwwasd.web.cern.ch/wwwasd/geant/>.
- [23] COMGEANT: COMPASS Monte Carlo simulation program based on GEANT3. <http://wwwcompass.cern.ch/twiki/bin/view/DataReconstruction/COMGeantDoc>.
- [24] A.-M. Dinkelbach. *Precision Tracking and Electromagnetic Calorimetry Towards a Measurement of the Pion Polarizabilities at COMPASS*. PhD thesis, Technische Universität München, June 2010.
- [25] E. H. et al. HERA-B Technical Design Report. *DESY-PRC*, January 1995.
- [26] W.-M. Y. et al. Review of Particle Physics. *Journal of Physics G Nuclear Physics*, 33:1–1232, July 2006.
- [27] K. N. et al. (Particle Data Group). Review of particle physics. *Journal of Physics G*, 37, 2011.
- [28] M. French et al. Design and results from the APV25, a deep sub-micron CMOS front-end chip for the CMS tracker. *Nuclear Instruments and Methods in Physics Research A*, 466(2):359 – 365, 2001.
- [29] J. Friedrich, 2011. Private communication.
- [30] J. Friedrich, A.-M. Dinkelbach, et al. The Silicon Vertex Detector of COMPASS with sub-ns Time Resolution. 2005.

- [31] L. Gatignon. User guide for M2 beam. <http://sl.web.cern.ch/sl/eagroup/beams.html#m2>, 2001.
- [32] J.-C. GAYDE. Surveyor report from edm. https://edms.cern.ch/file/1027853/1/SF02_SI123_15Sept2009.doc.
- [33] S. Gerassimov. Physics analysis software tool. <http://ges.home.cern.ch/ges/phast>.
- [34] S. Grabmüller. PHD thesis in preparation.
- [35] S. Grabmüller, 2011. Private communication.
- [36] B. Grube. *The Trigger Control System and the Common GEM and Silicon Readout for the COMPASS Experiment*. Diploma thesis, Technische Universität München, December 2001.
- [37] B. Grube. *A Trigger Control System for COMPASS and A Measurement of the Transverse Polarization of Λ and Σ Hyperons from Quasi-Real Photo-Production*. PhD thesis, Technische Universität München, January 2006.
- [38] A. Guskov, 2011. Private communication.
- [39] S. Hancock, F. James, J. Movchet, P. G. Rancoita, and L. VanRossum. Energy loss and energy straggling of protons and pions in the momentum range 0.7 to 115 GeV/c. *Phys. Rev. A*, 28:615–620, Aug 1983.
- [40] M. Huhtinen. Delta ray effects in silicon strip detectors. 1993.
- [41] L. Jones. *APV25-S1 User Guide Version 2.2*. RAL. http://www.te.rl.ac.uk/INS/Electronic_Systems/Microelectronics_Design/Projects/High_Energy_Physics/CMS/APV25-S1/files/User_Guide_2.2.pdf.
- [42] G. F. Knoll. *Radiation Detection and Measurement*. John Wiley & Sons, Inc., 1994.
- [43] Kobetich, E. J. and Katz, Robert. Energy Deposition by Electron Beams and δ Rays. *Phys. Rev.*, 170:391–396, Jun 1968.
- [44] L. Landau. On the Energy Loss of Fast Particles by Ionization. *J. Phys. USSR*, 8, 1944.
- [45] W. R. Leo. *Techniques for nuclear and particle physics experiments*. Springer, 1994.
- [46] COMPASS run logbook. <http://wwwcompass.cern.ch/RunLogbook/dirphp/>.
- [47] C. Marchand, 2011. Private communication.

Bibliography

- [48] Mathematica. Wolfram mathematica online integrator. <http://integrals.wolfram.com/index.jsp>.
- [49] C. J. Morningstar and M. Peardon. Glueball spectrum from an anisotropic lattice study. *Phys. Rev. D*, 60:034509, Jul 1999.
- [50] T. Nagel. PHD thesis in preparation.
- [51] T. Nagel. *Cinderella: an Online Filter for the COMPASS Experiment*. Diploma thesis, Technische Universität München, January 2005.
- [52] T. Nagel, 2011. Private communication.
- [53] Particle Data Group. Review of particle physics. *Journal of Physics G*, 33:1, 2010.
- [54] A. Peisert. Silicon microstrip detectors. *Adv. Ser. Direct. High Energy Phys.*, 9:1–79, 1992.
- [55] H. Pereira and J.-M. Le Goff. COMPASS spectrometer alignment. COMPASS Note 2003-4, August 2003.
- [56] S. Pflüger. *Investigations of the light meson spectrum with Compass using final states containing neutral particles*. Diploma thesis, Technische Universität München, August 2011.
- [57] R. and Turchetta. Spatial resolution of silicon microstrip detectors. *Nuclear Instruments and Methods in Physics Research Section A: Accelerators, Spectrometers, Detectors and Associated Equipment*, 335(1-2):44 – 58, 1993.
- [58] SINTEF. SINTEF website. <http://www.sintef.no/Home>.
- [59] The COMPASS collaboration. COMPASS-II Proporsal. *CERN-SPSC-2010-014 ; SPSC-P-340*, 2010.
- [60] S. Uhl, 2011. Private communication.
- [61] P. Zimmerer. *Performance of cryogenic silicon microstrip detectors at the COMPASS Experiment*. Diploma thesis, Technische Universität München, January 2011.

Own Contributions

This thesis was created within the framework of the chair of Prof. Stephan Paul at the Technische Universität München and at the COMPASS collaboration at CERN, Geneva.

I started my thesis in December 2010, already familiar with the silicon hardware from my time as a technical student. At that time, various issues concerning the alignment of the spectrometer in 2009 had just been revealed. I took over the preliminary alignment investigations conducted by Philipp Zimmerer and extended the analysis under the guidance of Jan Friedrich, now also covering aspects of the tracking. Input was given to the alignment coordinator Alexander Austregesilo revealing several shortcomings of the then used alignments. This way the need for a run-by-run alignment was shown. I evaluated several alignments, hence contributing to the development of the run-by-run alignment procedure and a successful test production in March 2011.

With a precision alignment available, I created a framework to analyze the silicon detector performance. I compared my results to the performance of the non-cryogenic detectors, analyzed by my predecessors. The obtained results are part of the upcoming COMPASS hadron spectrometer paper.

In April, I spent several weeks together with Karl Bicker planning and coordinating the construction of a new phase-separator for immediate application in silicon station SI02 for the muon run in 2011. I performed several cooling tests with the test setup in Munich and searched a cold leak together with the technicians of the UCN hut. After successful tests, I spent two weeks at CERN and assisted in the installation of the phase separator and in the commissioning of the silicon beam telescope. I took my shifts and on-call responsibilities in June 2011.

I analyzed the clustering algorithm used for the silicon microstrip detectors and implemented two improvements. One of them compensates for detector noise during the clustering step, the other one includes the long standing request to exploit the amplitude correlation to disentangle tracks creating overlapping clusters. Both improvements were implemented as an extension to the existing clustering in the reconstruction software and the impact on the tracking was studied with the help of Sebastian Uhl.

The simulation of the silicon detector response in the reconstruction software was revised, based on the previous work of Philip Zimmerer. The amplitude generation was adjusted to produce realistic values. A phenomenological algorithm reflecting the charge sharing process was derived from experimental data and implemented in the simulation software. This allows for the first time to reasonably use the same algorithms on real- and Monte Carlo data and thus cleared the way to more systematic studies on the improvement of the clustering algorithm.

Acknowledgments

First of all I would like to thank Prof. Stephan Paul for giving me this interesting topic. I really enjoyed working at E18 and in a multi-national collaboration at CERN.

Many thanks to Dr. Jan Friedrich for sharing his vast experience with me. He was always there, offering great ideas and many insights into physics, analysis and COMPASS.

Sebastian Uhl deserves many thanks for his frequent and always very kind help. I learned a lot from him. He had no reasons for helping me and answering my questions again and again. He did it nevertheless, and therefore I am immensely thankful.

Special thanks to Charly Bicker for introducing me to the silicon project and teaching me basically everything I know about the silicon hardware. Working with him was both fun and instructive.

Many thanks go also to my other silicon colleagues Steffi Grabmüller and Phillip Zimmerer, I really enjoyed working with you. Phillip deserves additional thanks for introducing me to the silicon software.

My sincerest thanks to everybody who proofread parts of this thesis, as there are especially Dr. Jan Friedrich and Sebastian Uhl, but also Steffi Grabmüller, Alex Austregesilo, Charly Bicker, Boris Grube and Martin Schmid. Your input was invaluable to me!

Thanks a lot to my office mates, Alex Austregesilo, Michael Tasior and Stefan Huber. It was really a great time and I enjoyed every single day with you.

I want to thank all my friends for great five years. Special thanks go to Michael Tasior for pushing me when I really needed it.

Ein besonderer Dank geht an meine Familie, die mich während meines ganzen Studiums unterstützt und ermutigt hat. Ohne euch wäre das alles nicht möglich gewesen.

For love, understanding and endless support, I want to thank Nane with all my heart.

Erklärung

Hiermit erkläre ich, diese Arbeit (einschließlich aller Abbildungen) selbständig verfasst und keine anderen Hilfsmittel als die angegebenen verwendet zu haben.

Michael Leeb